



Swansea University  
Prifysgol Abertawe

# Bayesian Inference and Collapse Models in Levitated Optomechanics

Shaun J. Laing

Swansea University

Submitted to Swansea University in fulfilment of the requirements for the  
Degree of  
*Ph.D.*

March 2024

Copyright: The Author, Shaun J. Laing, 2024

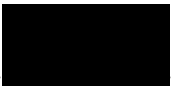
CC BY - Distributed under the terms of a Creative Commons Attribution 4.0  
License (CC BY 4.0).

## Abstract


An apparent contradiction exists between the wave nature of quantum mechanics allowing for superposition of states, and the observations of classical mechanics. Several possible solutions for this discrepancy have been suggested including the proposal that quantum and classical dynamics are simply approximations to a universal dynamics. Collapse models modify the usual Schrödinger equation that provides this universal dynamics and can be tested experimentally. In this thesis, we conceive of a Talbot matter-wave interferometer to probe the superposition of high-mass nanoparticles. We extend existing descriptions beyond the point-like regime allowing us to test collapse models with masses up to  $10^9$ u. During this development, we discover and correct an error in calculating the Talbot coefficients for a laser grating in the Mie regime. A Bayesian analysis is performed on simulated data making greater use of each recorded arrival position of the nanoparticle and provide a real-valued probability density to the parameter space as opposed to the binary exclusion plots of previous works. We find a limit to the size of spherical particles that can be used as a result of the grating transformation being averaged over the particle. As a result, during a collaboration with the Geraci group at Northwestern University, we develop a numerical method for finding where arbitrarily shaped particles scatter information about their position and use these techniques to derive the Talbot coefficients for arbitrary particle geometries.

# Declarations


This work has not previously been accepted in substance for any degree and is not being concurrently submitted in candidature for any degree.

Signed.  .....  
Date... 2.8.07 .....  
.....


This thesis is the result of my own investigations, except where otherwise stated. Other sources are acknowledged by footnotes giving explicit references. A bibliography is appended.

Signed.  .....  
Date.....  
.....

I hereby give consent for my thesis, if accepted, to be available for electronic sharing

Signed...  .....  
Date.....  
.....

The University's ethical procedures have been followed and, where appropriate, that ethical approval has been granted.

Signed.  .....  
Date.....  
.....

# Contents

<b>1</b>	<b>Introduction</b>	<b>1</b>
<b>2</b>	<b>Levitated Optomechanics</b>	<b>5</b>
2.1	Trapping Forces . . . . .	5
2.1.1	Rayleigh Sized Particles . . . . .	6
2.1.2	Mie Sized Particles . . . . .	7
2.1.3	Large Particles . . . . .	8
2.2	Trapping Configurations . . . . .	10
2.2.1	Optical Tweezers . . . . .	10
2.2.2	Cavity Optomechanics . . . . .	14
2.2.3	Optical Lattices . . . . .	14
2.3	Cooling of Particle Motion . . . . .	15
2.3.1	Scattering Force Based Cooling . . . . .	15
2.3.2	Parametric Feedback Cooling . . . . .	16
2.3.3	Electromechanical Cooling . . . . .	18
2.3.4	Cavity Cooling . . . . .	22
2.3.5	Cooling in an Optical Lattice . . . . .	23
2.3.6	Comparison of Cooling Schemes . . . . .	23
2.4	Trapping different shaped particles . . . . .	25
2.4.1	Rods . . . . .	26
2.4.2	Hexagonal Disks . . . . .	27
<b>3</b>	<b>Background Quantum Mechanics</b>	<b>30</b>
3.1	Density Operator . . . . .	30

3.1.1	Time Evolution of the Density Operator . . . . .	34
3.2	The Phase Space Description . . . . .	35
3.2.1	Time Dependence of the Wigner Function . . . . .	36
3.2.2	Husimi Q-Function . . . . .	38
3.3	Decoherence . . . . .	39
3.3.1	Deriving a General Form for Decoherence . . . . .	40
3.4	The Quantum-to-Classical Transition . . . . .	43
3.4.1	The Measurement Problem . . . . .	44
3.5	Proposed Solutions to the Measurement Problem . . . . .	46
3.5.1	The Copenhagen Interpretation . . . . .	47
3.5.2	Decoherence as a Solution . . . . .	47
3.5.3	The Many-Worlds Interpretation . . . . .	49
<b>4</b>	<b>Collapse Models</b>	<b>50</b>
4.1	Quantum Mechanics as an Approximation . . . . .	50
4.1.1	Deterministic Non-Linear Modifications . . . . .	52
4.1.2	Stochastic Non-Linear Modifications . . . . .	53
4.2	Spontaneous Collapse Models . . . . .	54
4.2.1	A Simple Example, The QMUPL Model . . . . .	55
4.2.2	GRW Model . . . . .	58
4.2.3	Diósi-Penrose Model . . . . .	59
4.2.4	Continuous Spontaneous Localisation . . . . .	60
<b>5</b>	<b>Interferometric Tests of Collapse Models</b>	<b>63</b>
5.1	Non-Interferometric Tests of Collapse Models . . . . .	63
5.2	Talbot-Lau Interferometry . . . . .	66
5.2.1	Laser Gratings . . . . .	68
5.3	A Single Source Talbot Interferometer . . . . .	70
5.3.1	MAQRO Experiment . . . . .	73
5.3.2	Initial State . . . . .	75
5.3.3	Propagation . . . . .	76
5.3.4	Grating Transformation and Interference Effect . . . . .	78
5.4	Derivation of the Talbot Coefficients . . . . .	82

5.4.1	Talbot Coefficients in the Rayleigh Regime . . . . .	82
5.4.2	Mie Theory . . . . .	84
5.4.3	Talbot Coefficients Beyond the Point-Like Approximation . . . . .	89
5.5	Decoherence within the Interferometer . . . . .	94
5.5.1	Absorption of Thermal Radiation . . . . .	95
5.5.2	Emission of Thermal Radiation . . . . .	97
5.5.3	Elastic Scattering of Thermal Radiation . . . . .	97
5.5.4	Collisions with Residual Gas Particles . . . . .	98
5.5.5	Position Resolution . . . . .	99
5.6	Including Collapse Models . . . . .	99
5.6.1	CSL in the Rayleigh Regime . . . . .	100
5.6.2	CSL Beyond the Rayleigh Regime . . . . .	100
<b>6</b>	<b>Bayesian Inference</b>	<b>102</b>
6.1	Introduction to Bayesian Inference . . . . .	102
6.1.1	The 2 Dimensional Case . . . . .	105
6.2	Choice of Prior . . . . .	107
6.2.1	Uninformative Priors . . . . .	107
6.3	Simulations of the Interferometer . . . . .	110
6.3.1	Bayesian Analysis of Simulated results . . . . .	110
6.3.2	Priors used to Estimate the CSL Parameters . . . . .	113
6.4	Parametrisation by Information Gain . . . . .	116
6.4.1	Expected Information Gain . . . . .	118
6.4.2	Expected Information with no Collapse . . . . .	119
6.4.3	Parametrisation by Decoherence rate $\lambda_c$ . . . . .	122
6.5	Choosing the Control Parameters . . . . .	125
6.5.1	Choosing Parameters to Maximise Information Gain . . . . .	125
6.5.2	Choosing Parameters to Maximise the Change in Visibility . . . . .	129
6.6	Scenario Comparisons . . . . .	130
<b>7</b>	<b>Information Radiation in a Beam</b>	<b>134</b>
7.1	Scuff-EM . . . . .	135
7.1.1	Numerical solutions . . . . .	137

7.1.2	Scuff-EM Implementation of a Gaussian Beam . . . . .	139
7.1.3	Alternative Method for Defining a Gaussian Beam . . . . .	140
7.2	Information Radiation . . . . .	142
7.2.1	Analytical Information Radiation Pattern in the Rayleigh Limit . . . . .	143
7.2.2	Numerical Solution for the IRP for Rayleigh Spheres . . . . .	145
7.2.3	Analytical Information Patterns for Large Spheres . . . . .	146
7.2.4	Numerical Information Patterns for Large Spheres . . . . .	151
7.2.5	Information Radiation Patterns from Hexagonal Plates . . . . .	153
7.3	Numerical Solutions for the Talbot Coefficients . . . . .	156
<b>8</b>	<b>Conclusion</b>	<b>158</b>

# Acknowledgements

I would like to thank my supervisor Dr. James Bateman for his invaluable advice, continuous support, and patience throughout my Ph.D. study. I would also like to thank my family who have been great support through all the ups and downs of my academic journey, and my friends who were always on hand to provide a much needed distraction from the seemingly endless work. I am grateful as well to Dr. Andrew Geraci and the team at Northwestern who welcomed me in early 2023. The time I spent in their company was greatly rewarding, both academically and personally. I will always look back on my time in The Windy City with fondness.

On the topic of cities, I would like to give note to the city of Swansea. My time here has given me the opportunity to explore the stunning Welsh landscape (weather permitting of course!), and has provided me with many memorable evenings. I suspect that I will never stop finding sand from Swansea beach in pockets of jackets.



# Publications Resulting from this Work

1. **Bayesian inference for near-field interferometric tests of collapse models**

*S. Laing, J. Bateman*

*arXiv 2023 arXiv:2310.05763, To be published*

See Chapters 5, and 6

2. **Optimal displacement detection of levitated dielectric objects using optical radiation**

*S. Laing, S. Klomp, G. Winstone, A. Grinin, A. Dana, Z. Wang, K.S. Widyatmodjo, P. Maurer, O. Romero-Isart, J. Bateman, A. Geraci*

*In preparation, Author list TBC*

See Chapter 7

# List of Figures

2.1	Force due to a field . . . . .	7
2.2	Particle in a Gaussian beam . . . . .	8
2.3	Particle in a focused beam . . . . .	9
2.4	Optical Potential . . . . .	11
2.5	Optical lattice . . . . .	15
2.6	Scattering force cooling . . . . .	16
2.7	Feedback cooling . . . . .	17
2.8	Electromechanical cooling . . . . .	18
2.9	Charged nanoparticle oscillations . . . . .	21
2.10	Trapped nano-rod . . . . .	25
2.11	Nano-rod PSD . . . . .	27
2.12	Trapped hexagonal plate . . . . .	27
2.13	Hexagonal plate PSD . . . . .	28
3.1	QHO wave functions . . . . .	32
3.2	QHO Wigner function . . . . .	37
5.1	CSL exclusion plot . . . . .	64
5.2	Talbot interference pattern . . . . .	67
5.3	Talbot-Lau interferometer . . . . .	69
5.4	Single source interferometer . . . . .	71
5.5	Initial characteristic function . . . . .	77
5.6	$t_1$ characteristic function . . . . .	78
5.7	Grating effect . . . . .	79
5.8	Final characteristic function . . . . .	80

5.9	Mie scattering plane . . . . .	89
5.10	Mie and Rayleigh optical forces . . . . .	91
5.11	Interferometer decoherence effects . . . . .	96
5.12	Internal temperature during feedback cooling . . . . .	98
6.1	Coin toss posteriors . . . . .	104
6.2	2D posterior example . . . . .	106
6.3	Proposed interferometer diagram . . . . .	111
6.4	Interferometer probability distribution . . . . .	112
6.5	Example CSL posteriors . . . . .	113
6.6	CSL example priors . . . . .	114
6.7	Information as a function of number of data points . . . . .	120
6.8	Information gain as a function of particle mass . . . . .	121
6.9	Predicted upper bounds on $\lambda_c$ . . . . .	123
6.10	Iterative bisection algorithm . . . . .	124
6.11	Gradient ascent algorithm . . . . .	126
6.12	Optimum control parameters . . . . .	130
6.13	Information gain for different pressures . . . . .	131
6.14	Information gain for various spacecraft drifts . . . . .	132
7.1	Scuff-EM calculation of the scattered field . . . . .	136
7.2	Scattered electric fields . . . . .	137
7.3	Scuff-EM Gaussian beam . . . . .	141
7.4	Analytical point-like IRPs . . . . .	145
7.5	Scuff-EM point-like IRPs . . . . .	146
7.6	Analytical IRPs for various radii . . . . .	150
7.7	Scuff-EM IRPs for various radii . . . . .	152
7.8	Hexagonal plate with degrees of freedom . . . . .	153
7.9	IRPs for various hexagonal plates . . . . .	155
7.10	Cartesian hexagonal plate scattering amplitudes . . . . .	156

# List of Tables

5.1	MAQRO experimental parameters . . . . .	74
5.2	Spherical Bessel and Hankel functions. . . . .	86
7.1	Dimensions for the hexagonal plate particles. . . . .	154

# Chapter 1

## Introduction

Quantum mechanics stands as a remarkably successful theory for describing the behaviour of microscopic systems. It can successfully predict various phenomena such as blackbody radiation [1], atom interferometry [2], semi-conductors [3], the properties of lasers [4], among many others. Quantum theory also appears to hold for ever larger systems being shown to hold for systems with masses of over 25,000u, or  $4.2 \times 10^{-23}$ kg in interferometry experiments [5]. This is in stark contrast, however, to macroscopic observations that apparently do not obey quantum mechanics. For example, the famous Schrödinger's cat thought experiment shows this disparity between a quantum world, which can exist in superposition, and the classical world that does not obey superposition. How the quantum dynamics of superpositions gives way to the probabilistic outcomes via the Born rule when measured remains unsolved. This is the heart of the measurement problem.

There exist a number of proposed solutions to this measurement problem, from the Copenhagen interpretation [6], which is sometimes described as “Shut up and calculate!”, to more exotic ideas such as the Many-Worlds interpretation by Hugh Everett [7]. A possible set of solutions are modifications to the Schrödinger equation known as collapse models which provide a clear mathematical framework that can be tested empirically, unlike the Copenhagen and Many-Worlds interpretations. These add a stochastic term to the Schrödinger equation that drives large scale systems into a single state with probabilities

matching the Born rule. Collapse models are distinct from more traditional decoherence mechanisms. Decoherence is an effect caused by the quantum system coupling to the environment and destroys the interference between states leaving a statistical mixture of states. Collapse models on the other hand, affect even perfectly isolated systems by providing a noise field throughout space that couples to all quantum systems, and drives the system into a statistical mixture matching the Born rule. All collapse models also share an amplification mechanism. This is needed so that microscopic systems are able to maintain their coherence for indefinitely long periods of time, while larger, macroscopic systems, decay sufficiently quickly to prevent macroscopic superpositions on large, human, scales [8]. The parameters defining these models must be determined empirically. This can be achieved in two ways, either by measuring a predicted anomalous heating (or absence thereof) from the collapse noise, or by directly probing the superposition of large masses via matter-wave interferometry. The latter requires considerable effort to overcome various hurdles. This includes mitigating the effects of traditional decoherence sources which become a greater challenge to deal with as the system size increases especially for interferometric experiments [9].

Previous macromolecule experiments work with beams of these molecules and record the number of counts in a given time frame, effectively producing a histogram over the measurement space [5, 10]. In order to ensure the coherence for larger particles, proposed large mass interferometry experiments use a single particle source with repeated measurements [11]. This procedure leads to a sparse data set to which we apply Bayes' rule to make better use of the data. By applying Bayes' theorem [12] to the results of simulated interferometry experiments, we can tune the parameters of an experiment to maximise the effect of a real-world experiment. We have the option of maximising the information gained in such an experiment [13], or by maximising the number of parameters of the collapse model we are able to rule out.

We can use optomechanical techniques to prepare large scale particles as a coherent source of matter-waves, and to induce the interference effect through a Talbot interferometer. These optomechanical systems are based in the use of radiation pressure of light. The use of radiation pressure of light has been

demonstrated to affect mechanical motion for many years, from Kepler noticing that the tails of comets always point away from the sun [14]. Radiation pressure was confirmed in the lab in 1901 by Nichols and Hull [15]. After the invention of the laser Arthur Ashkin was able to demonstrate the ability of light to control the mechanical motion of small dielectric spheres [16] in 1970. These early ‘optical-tweezers’ used the radiation pressure force from the momentum of light to push the sphere up, while using the force of gravity to pull the object back down to Earth. Later work by Ashkin realises that the dielectric sphere is attracted to the center of a Gaussian beam where the intensity is highest. By tightly focusing the beam, a 3D potential well can be created by the gradient force allowing the sphere to be trapped in a horizontally propagating beam. Beginning as optical tweezers used to manipulate biological samples [17], the field of levitated optomechanics has found a number of uses such as highly sensitive force probes [18]. More recent work, focused on cooling the motion of optically trapped nanoparticles to the ground state [19, 20] has opened the door for macroscopic tests of quantum mechanics. This has allowed researchers to explore various physical principles from attempting to witness quantum gravity [21] to testing the boundaries of quantum theory in the mesoscopic regime [10].

The rest of this thesis will be structured as follows. We start in Chapter 2 by introducing the idea of levitated optomechanics focusing on methods of trapping particles and cooling their motion. This chapter mainly focuses on spherical particles as the interferometry experiment we will discuss uses spherical particles. However, we are also interested in extending our theory to particles with arbitrary geometry. As a result of this, the final section of Chapter 2 will focus in trapping particles with different geometries. In Chapter 3 we introduce the important concepts of quantum mechanics that will form the backbone of our theoretical discussion. We start by introducing the density operator and applying this to the Wigner function, we then introduce a theoretical description of decoherence that will be necessary to accurately predict the outcome of an interferometry experiment. Chapter 4 introduces the idea of collapse models giving the theory of a handful and fully introducing the continuous spontaneous localisation (CSL) model that will be the main theory explored in the interferometry simulations.

With this background theory in place, Chapter 5 will put this all together and produce the theory for a matter-wave interferometer for particles with radii in the Mie regime that can test any collapse model that manifests as a source of decoherence. Bayes theorem is introduced in Chapter 6. This is then used to analyse the results of our simulations and make predictions regarding the probability that regions of the CSL parameter space that a given experiment, with given control parameters, could be ruled out. Finally, in Chapter 7 we consider the radiation of information for trapped particles. Our discussions start by reproducing the known results for spherical particles and then applies numerical methods to find the information radiation pattern for hexagonal plates. This then informs an approach to finding the scattering decoherence for a particle in a standing wave phase grating, such that our simulated interferometer can be applied to any particle geometry.



# Chapter 2

## Levitated Optomechanics

From set-ups such as LIGO that used a laser interferometer to measure the change in path length as a result of gravitational waves [22], to levitating and manipulating the motion of small particles in devices often referred to as ‘optical tweezers’ [16], optomechanics has proven to be a useful method of measuring and manipulating mechanical motion. The earliest optical tweezers took advantage of the scattering force of laser light via radiation pressure. In 1970 Arthur Ashkin demonstrated the use of radiation pressure to accelerate and trap micron-sized dielectric particles in liquids and gasses [16]. By illuminating a single particle with a laser, it can be observed that the particle is accelerated along the direction of the laser’s propagation, and, if the laser is focused, the particle will be drawn into the beam centre. In Ashkin’s experiments, the particle was kept in a glass cell, and when it reached the edge of the cell, it remained trapped in the laser until it was turned off, at which point the particle began to drift under the effects of Brownian motion.

### 2.1 Trapping Forces

In order to describe the trapping potential of a laser trap, we must understand the forces acting on the particle. The forces acting on the particle depend on its size relative to the wavelength of the incident laser light. It is often convenient to use the dimensionless size parameter  $kR$ , where  $k = 2\pi/\lambda$  is the wave-number

of the incident light and  $R$  is the radius of the spherical particle. This gives rise to three regimes with different methods of finding the forces acting on the particle. For particles with a size parameter of  $kR \lesssim 1$  we can treat the particle as a point-like dipole. This is the Rayleigh regime. For particles in the range  $1 \lesssim kR \lesssim 100$  we are in the Mie (sometimes known as the Mie-Lorentz) regime. And for particles with a size parameter  $kR > 100$  we are in the geometric optics regime [23].

### 2.1.1 Rayleigh Sized Particles

In 1986 Ashkin, along with Dziedzic, Bjorkholm, and Chu, developed the first single laser trap that could trap the particle in three dimensions [24]. Before this point, traps only worked to attract particles to the beam axis, other forces were needed to keep the particle in the same location such as gravity or the radiation pressure of a second laser [16]. The new trapping scheme proposed by Ashkin et al. is based on the use of the *gradient force*. The gradient force is a consequence of the radiation pressure and points in the direction of positive gradient of light intensity. This is in contrast to the *scattering force* that is induced by photons scattering from the particle and always points in the direction of propagation of the laser.

In the Rayleigh regime, where the radius of the particle is much smaller than the wavelength of the incident light  $R \ll \lambda$ , the scattering force is given by [25]

$$F_{\text{scat}}(\mathbf{r}) = \frac{128\pi^5 R^6}{3c\lambda^4} \left( \frac{m^2 - 1}{m^2 + 2} \right)^2 n_{\text{med}} I(\mathbf{r}) \quad (2.1.1)$$

where  $I(\mathbf{r})$  is the intensity of the laser at the point  $\mathbf{r}$ ,  $n_{\text{med}}$  is the refractive index of the medium,  $m = n_{\text{obj}}/n_{\text{med}}$  is the refractive index of the particle relative to that of the medium. The gradient force is also given by,

$$F_{\text{grad}}(\mathbf{r}, t) = 4\pi n_{\text{med}}^2 \epsilon_0 R^3 \left( \frac{m^2 - 1}{m^2 + 2} \right)^2 \frac{\nabla E^2(\mathbf{r}, t)}{2}. \quad (2.1.2)$$

The time average of Eq. (2.1.2) is given as,

$$\begin{aligned} F_{\text{grad}}(\mathbf{r}) &= \langle F_{\text{grad}}(\mathbf{r}, t) \rangle \\ &= \frac{2\pi n_{\text{med}}^2 \epsilon_0 R^3}{c} \left( \frac{m^2 - 1}{m^2 + 2} \right)^2 \nabla I(\mathbf{r}). \end{aligned} \quad (2.1.3)$$

### 2.1.2 Mie Sized Particles

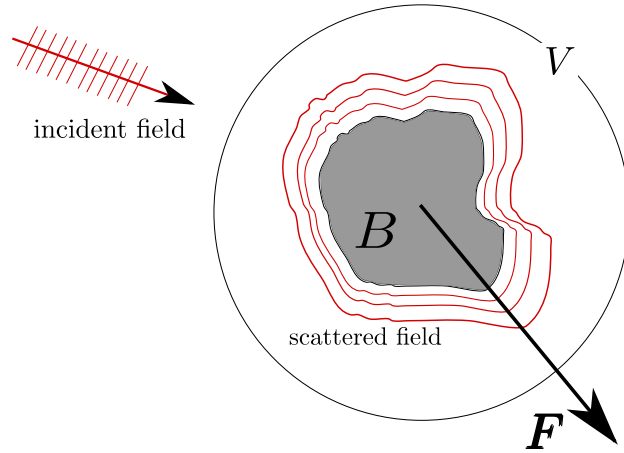


Figure 2.1: The force acting on the object  $B$  as a result of the incident field is related to the electric and magnetic fields on some surface  $V$  surrounding the object.

For spherical particles with radii comparable to the wavelength of the trapping laser we must consider the shape of the particle more closely. Different shapes will have different solutions for the forces acting on the particle. For various shapes, such as spheres, spheroids, and infinite cylinders, we can use the Mie equation, based on spherical harmonics, to describe the scattering of light from the particles [26–28].

We must turn to the Maxwell stress tensor  $\overleftrightarrow{T}$  to find the force acting on a particle. The elements of the Maxwell stress tensor are given by [23, 29],

$$T_{i,j} = \left[ \epsilon_0 \epsilon E_i E_j - \mu_0 \mu H_i H_j - \frac{1}{2} (\epsilon_0 \epsilon |E|^2 + \mu_0 \mu |H|^2) \delta_{i,j} \right] \quad (2.1.4)$$

where  $E_i$  and  $H_i$  are the  $i \in (x, y, z)$  component of the electric and magnetic fields respectively. Under the assumption that the particle is rigid, and by integrating the time averaged stress tensor over the area of our object, we find the time averaged force to be,

$$\langle \mathbf{F} \rangle = \int_V \langle \overleftrightarrow{T}(\mathbf{r}, t) \rangle \cdot \mathbf{n}(\mathbf{r}) da \quad (2.1.5)$$

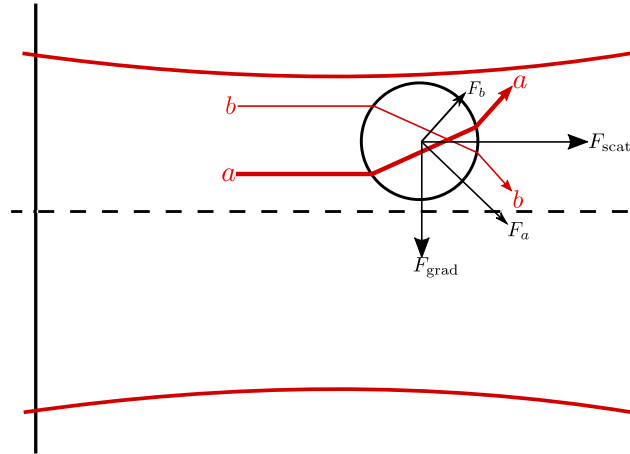


Figure 2.2: A dielectric sphere with large radius compared to the trapping wavelength levitated in a Gaussian beam located outside the central bright spot. The light rays  $a$  and  $b$  are shown along with the forces that oppose the change in momentum as each light ray is refracted.

where  $\mathbf{n}(\mathbf{r})$  is the unit vector of the closed surface  $V$  at the point  $\mathbf{r}$ , and  $da$  is the area element. The force on an object  $B$  due to scattering of an electromagnetic field is shown in Fig. 2.1.

### 2.1.3 Large Particles

For spheres of large radius compared to the wavelength, the forces acting on the particle are a result of the change in momentum of the light as it passes through the particle. The light rays are refracted as they enter and exit the particle. This causes a shift in the light ray's momentum. Considering light rays  $a$  and  $b$  that enter the particle at equal distance from its centre as seen in Fig. 2.2, we can explore how the particle's location in a Gaussian beam affects the forces acting on it. As the light ray  $a$  leaves the particle, it is propagating in a different direction to when it entered. This leads to a shift on the light's momentum. The conservation of momentum gives rise to a force opposing this momentum shift  $F_a$ . When on the beam axis, the particle refracted light rays  $a$  and  $b$  have the same intensity. This means that the forces opposing the change in momentum are equal and opposite in their components orthogonal to the direction of the

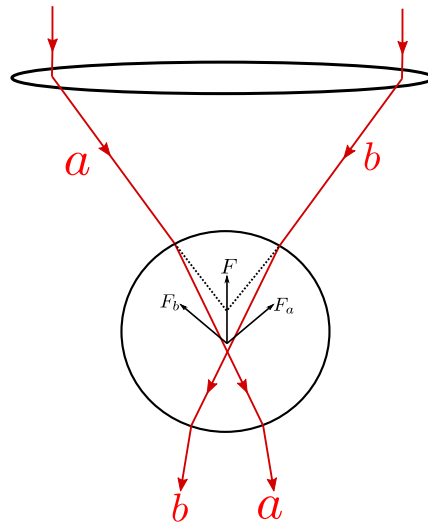


Figure 2.3: A particle trapped in a focused Gaussian beam. Here the particle is located beyond the focal point. This creates a force pulling it back to the focal point.

beam propagation. These beams also undergo Fresnel reflection as they enter and exit the particle transferring some momentum to the particle. This causes a scattering force  $F_{\text{scat}}$  acting in the direction of laser propagation. However, when the particle is off-axis, as shown in Fig. 2.2, one of the light rays  $a$  has a higher intensity leading to a greater momentum shift in one direction. As a result, a net force occurs pulling the particle back to the beam axis [16, 30].

By focusing the laser beam, we can also attract the particle to the beam waist as is seen in Fig. 2.3. When the particle is moved away from the focal point, the component of the momentum of the light rays in the direction of the beam propagation, reduces. This causes a force to act on the particle to restore that momentum.

## 2.2 Trapping Configurations

Since Ashkin first demonstrated it was possible to trap small micron sized spheres in a laser beam, a number of different configurations have been proposed to trap these particles. The first traps used only the scattering force to trap particles. This force attracted the particle towards the centre of the beam and pushed it in the direction of the laser propagation. Another force was needed to keep the particle from moving in this direction. Initial experiments took place in a glass cell where the wall of the cell would prevent the continued motion of the particle [16].

Later, the force of gravity could be used to restrict the motion of the particle. A particle can be illuminated by a vertically propagating Gaussian beam above the laser's focal point. The particle will feel the upwards directed scattering force  $F_{\text{scatt}}$  and the downwards pointing gravitational force  $F_{\text{grav}}$ . Close to the focal point, where the laser intensity is large, the particle will feel a net upwards force  $F_{\text{scatt}} > F_{\text{grav}}$ . However, above the point where the laser has diverged enough, the intensity leads to a scattering force less than the gravitational force  $F_{\text{scatt}} < F_{\text{grav}}$ . Thus, the net force on the particle is directed downwards. At the point where the forces are balanced  $F_{\text{scatt}} = F_{\text{grav}}$ , the particle will hover in place [30].

### 2.2.1 Optical Tweezers

By using a tightly focused Gaussian laser beam, it is possible to create a single-beam gradient optical trap, often referred to as an optical tweezer. As long as the particle stays within a distance smaller than the beam waist of the focal point, it will feel a harmonic potential centred on the focal point of the laser [31]. This potential is created by the forces discussed in section 2.1. In the Rayleigh regime, this potential is a result of the gradient force Eq. (2.1.2) towards the focal point being larger than the scattering force Eq. (2.1.1) in the direction of beam propagation.

For particles in the geometric optics regime, where  $kR > 100$ , a similar argument about momentum conservation can be used. As the particle moves away from the focal point, the exiting light rays are refracted away from each other

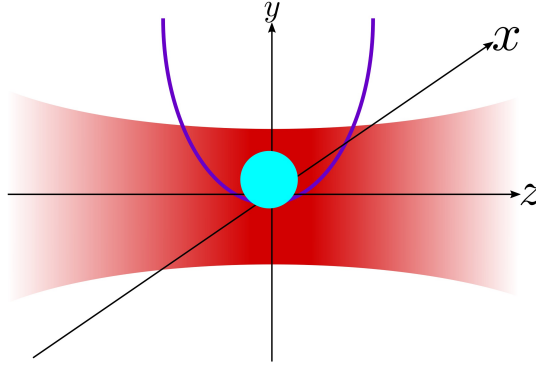


Figure 2.4: The optical potential created by a single focused Gaussian beam trap. A spherical particle with mass  $m$  oscillates about the trap centre with a frequency  $\Omega_\mu$  where  $\mu \in (x, y, z)$ .

changing the momentum. This induces a force on the particle moving it to conserve the total momentum of the system. When the particle has returned to the focal point of the trap, the forces balance out [32].

The potential energy felt by a point-like particle with a dipole moment  $\mathbf{P}$  in a slowly varying optical field is given by [33],

$$U(\mathbf{r}) = -\mathbf{P} \cdot \mathbf{E}(\mathbf{r}) \quad (2.2.1)$$

where the dipole moment is given by

$$\mathbf{P} = \alpha \mathbf{E}(\mathbf{r}). \quad (2.2.2)$$

From here, we find the optical force to be

$$\mathbf{F} = \nabla U. \quad (2.2.3)$$

In general, electro-magnetic waves oscillate rapidly, we take the time average of the force,

$$\langle \mathbf{F} \rangle = \nabla \langle U \rangle \quad (2.2.4)$$

By describing the trap as acting like a Hookeian spring with an optical force in one dimension of,

$$F_{\text{opt}} = -k_x \Delta x \quad (2.2.5)$$

where  $\Delta x$  is the displacement of the particle from the trap centre and  $k_x$  is the trap stiffness in analogy with the spring constant from Hooke's law. This leads to a Harmonic trapping potential of the form,

$$U(x) = \frac{1}{2}k_x\Delta x^2. \quad (2.2.6)$$

The depth of this potential, known as the trap depth, is often given in units of the thermal energy  $k_B T_{\text{CoM}}$  where  $k_B$  is the Boltzmann constant and  $T_{\text{CoM}}$  is the centre of mass temperature of the particle's motion [31]. The trap depth is the amount of energy needed for the particle to escape the trap and is found via  $U(\infty) - U(0)$  where we must consider the fact that for large displacement, the trap cannot be considered Hookien, and we must use the time average of Eq.(2.2.1).

In order to calibrate the optical tweezers we must determine the trap stiffness  $k_x$ . If we have enough information about the properties of the trapping laser and the trapped particle, we can determine the trap stiffness. However, the interaction between the laser and the particle is dependent on many parameters that are difficult to determine. There are a number of alternate methods to achieve this. Perhaps the most simple method is to make use of the equipartition theorem.

In a trap that acts as a harmonic potential, as described in Eq. (2.2.6), we find the thermal average of the potential is [31],

$$\langle U(x) \rangle = \frac{k_x}{2} \langle \Delta x^2 \rangle = \frac{k_x}{2} \int_{-\infty}^{\infty} p(x) \Delta x^2 dx = \frac{k_B T}{2}. \quad (2.2.7)$$

Some simple algebra then reveals that the trap stiffness is

$$k_x = \frac{k_B T}{\langle \Delta x^2 \rangle}. \quad (2.2.8)$$

We can estimate the average  $\langle \Delta x^2 \rangle$  by recording the trajectory of the particle over some sufficiently long time period  $\Delta t \gg \tau_{\text{ot},x}$  where  $\tau_{\text{ot},x}$  is the relaxation time of the trap and take the sample variance

$$\langle \Delta x^2 \rangle \approx \frac{1}{L} \sum_{l=1}^L (x_l - x_0)^2 \quad (2.2.9)$$



where  $x_0$  is the mean position of the particle (this should be the trap centre), and  $x_l$  is the particle location at the  $l$ -th time step.

By following the method given in [31, 34], we can calibrate the trap via the power spectral density. This is one of the most reliable methods of trap calibration. Considering a spherical particle with radius  $R$  immersed in a fluid with a viscosity  $\eta$  at some temperature  $T$ . Stokes' law gives the friction coefficient as,

$$\gamma = 6\pi\eta R \quad (2.2.10)$$

and the Einstein-Smoluchowski relation gives the diffusion constant as,

$$D = \frac{k_B T}{\gamma} \quad (2.2.11)$$

where  $k_B$  is Boltzmann's constant. The trapped particle follows the same motion as an over-damped Brownian particle, and according to the Einstein-Ornstein-Uhlenbeck theory, this motion is found by solving the following Langevin equation,

$$\frac{dx}{dt} = \frac{F(x)}{\gamma} + \sqrt{2D}W(t) \quad (2.2.12)$$

where  $F(x)$  is the optical trapping force and  $W(t)$  is a white noise term with the properties

$$\langle W(t) \rangle = 0; \quad \langle W(t)W(t') \rangle = \delta(t - t'). \quad (2.2.13)$$

In a harmonic potential, the force is given by  $F(x) = -k_x \delta x$ . Using this and Eq. (2.2.12) and by taking the Fourier transform, we find the power spectral density which has a Lorentzian form and is the expected value of the average energy in the frequency domain,

$$P(f) = \langle |\tilde{x}(f)|^2 \rangle = \frac{D}{2\pi^2(f_c^2 + f^2)} \quad (2.2.14)$$

where  $f_c = k_x/(2\pi\gamma)$  is the corner frequency, and  $\tilde{x}(f)$  is the Fourier transform of the time dependent position function. After empirically determining the power spectral density, the parameters  $f_c$  and  $D$  can be found via a least-square fitting method. From these, the values of  $k_x$  and  $\gamma$  can be estimated.

### 2.2.2 Cavity Optomechanics

It is possible to trap a nano-particle in the optical mode of a Fabry-Perot cavity. By using a second mode we can also cool the motion of sub-wavelength particles to the ground state from room temperature [19]. The cavity is made of two mirrors separated by a distance  $L$ . This leads to a number of allowed cavity modes with angular frequencies,

$$\omega_m = m\pi \frac{c}{L} \quad (2.2.15)$$

where  $m$  is the mode number. The distance between two of these resonant modes is the free spectral range given by,

$$\Delta\omega_{\text{FSR}} = \pi c/L \quad (2.2.16)$$

We can then introduce the quality factor of the cavity  $Q_{\text{opt}} = \omega_{\text{cav}}\tau$ , where the photon life time is  $\tau = \kappa^{-1}$ . The cavity decay rate  $\kappa = \kappa_{\text{ex}} + \kappa_0$  is made up of the loss rate at the input mirror  $\kappa_{\text{ex}}$  and the loss rate for the various phenomena in the cavity  $\kappa_0$ . The use of a cavity to trap a particle can induce cooling of the particle motion. This will be discussed further in Section 2.3.4.

### 2.2.3 Optical Lattices

Optical lattice traps, sometimes called interferometric traps, make use of the interference effect of light to trap multiple particles. The simplest optical lattice is created by two counter propagating beams generating a standing wave. This leads to repeating regions of high and low intensity where particles can be trapped as shown in Fig. 2.5. It is also possible to trap more than one particle by taking advantage of the multiple trapping sites present in this set-up. By introducing a third beam, it is also possible to create hexagonal “bee-hive” like structures [35]. In principal, it is also possible to form all fourteen Bravis lattice shapes by using no more than four beams [36] and all two-dimensional shapes have been experimentally demonstrated [37]. The Bravis lattice shapes beyond the counter propagating beams have not had much application in the optomechanics community, but have seen considerable use in cold atoms.

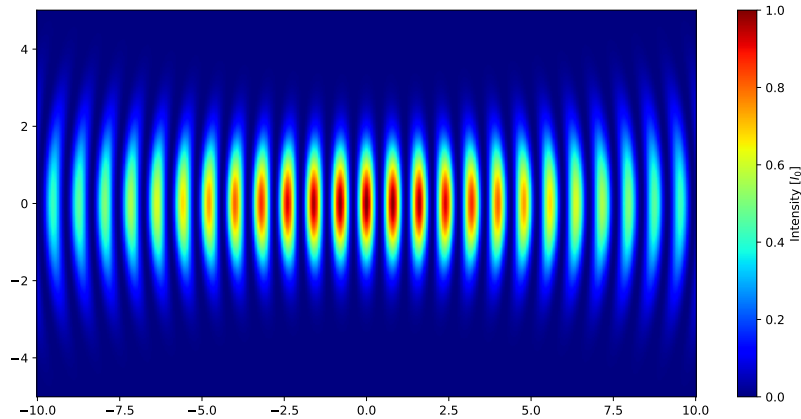


Figure 2.5: Intensity two counter propagating  $x$  polarised beams propagating in the  $z$  axis. Each beam has a waist of  $2\mu\text{m}$  and wavelength  $1550\text{nm}$ . The intensity profile is proportional to  $|\mathbf{E}(x, z)|^2$  and is given in units of the maximum intensity  $I_0$ .

## 2.3 Cooling of Particle Motion

A powerful property of optically levitated systems is their decoupling from the environment. This allows us to perform experiments to test quantum mechanics on small particles whilst minimising the effects of environmental decoherence. However, the motion of the particle in the trap still provides some issues preventing us from using the particle as a coherent source. Therefore, it is advantageous to cool the motion of the particle. In our interferometry experiments discussed in Chapter 5, cooling the particle's motion will be necessary in creating a sufficiently coherent single particle source for our matter-wave. We discuss here a number of methods used for cooling the motion of the particle.

### 2.3.1 Scattering Force Based Cooling

One method of cooling the motion of trapped nano-particles involves the scattering force. As the particle moves in the trap, the trapping beam is deflected. This deflection can be measured and used to track the motion of the particle. We can also plot the power spectrum of the particle's motion in each axis  $\mu \in (x, y, z)$

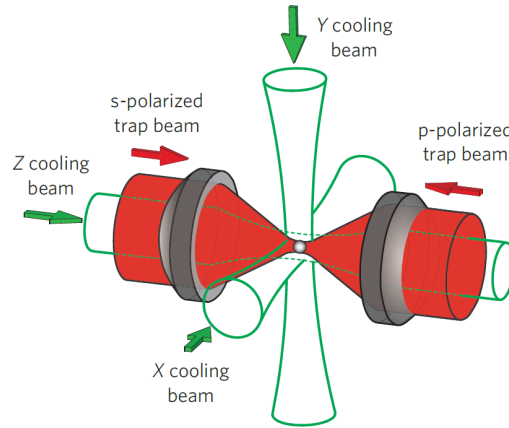


Figure 2.6: The set-up used in [38]. A nano sphere is trapped at the focus of a counter-propagating trap with its motion cooled by three cooling lasers, each propagating in one of the axial directions.

which follows the function,

$$S_{\mu}(\Omega) = \frac{2k_B T_{\text{env}}}{m} \frac{\Gamma_0}{(\omega_{\mu}^2 - \Omega^2)^2 + \Omega^2 \Gamma_0^2} \quad (2.3.1)$$

where  $\Omega/2\pi$  is the observation frequency,  $\Gamma_0$  is the damping due to residual gas, and  $\omega_{\mu}$  is the resonant frequency of the particle in each axis  $\mu \in (x, y, z)$ . The position of the particle is tracked and its velocity calculated for each direction. A time varying feedback signal for each axis is then generated proportional to the velocity in that axis plus some offset. This feedback signal is applied to an acousto-optic modulator that modulates the amplitude of the cooling laser directed in the  $\mu$  axis. The cooling laser then applies a scattering force that opposes the particle motion. This was implemented in a standing wave trap of counter-propagating, orthogonally polarised beams in [38] in the set-up shown in Fig. 2.6.

### 2.3.2 Parametric Feedback Cooling

First demonstrated in 2012 by Gieseler [39], parametric feedback cooling is able to cool the motion of all translational degrees of freedom using a single laser beam that is also used for trapping. In essence, feedback cooling works by increasing the

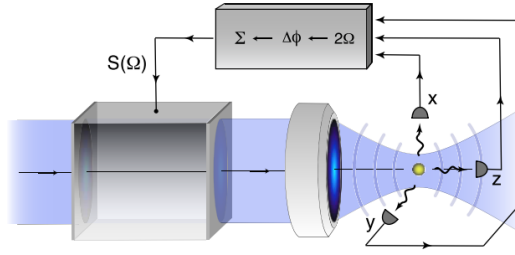


Figure 2.7: The centre of mass motion in each axis  $\mu$  is measured by an interferometric signal incident on a detector to measure a given axis of motion. This signal is then doubled in frequency and phase shifted. The final modulation signal  $S(\Omega)$  is the sum of these three signals [39].

trap stiffness  $k_\mu$  as the particle moves away from the centre of the trap hindering its motion. Then, as the particle moves towards the centre again, the trap stiffness is reduced to avoid increasing the particle's velocity too much. Unlike in other feedback methods based on the radiation pressure, which only works in the direction of laser propagation [40], this scheme is based on the gradient force which works in all directions. This removes the need for extra lasers to achieve cooling in each desired direction.

In order to achieve the feedback cooling, we measure the location of the particle to produce a signal of the particle's motion for each axis. The frequency of these signals is doubled and phase shifted to find the modulation signal for the trap stiffness. Because the frequencies of each axis of motion are not degenerate, there is no cross-coupling between the signals. Therefore, the signal that drives the trap stiffness modulation is simply the sum of the three calculated signals. Because the trap stiffness is directly proportional to the power of the trapping laser, the modulation signal is sent to any device that can adjust the laser power, often this is an electro-optic modulator.

The lowest possible centre of mass temperature  $T_{\text{CoM}}$  is limited by the shot noise uncertainty in measuring the particle's position in each axis. We can reduce the uncertainty by increasing the signal power at the detector either by increasing the laser power or the particle radius. Both options, however, lead to an increase in the scattering which introduces recoil heating. A trade-off is needed between

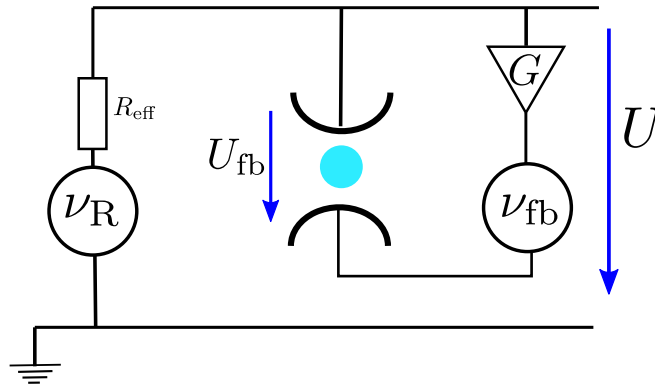


Figure 2.8: Circuit diagram for feedback cooling the motion of a trapped charged particle. A feedback voltage  $U_{fb}$  is applied to the particle by amplifying the voltage signal generated by the particle motion  $U$ . This introduces a voltage noise  $\nu_{fb}$ .

the uncertainty in measured position and the recoil heating to reach the lowest possible temperatures. By optimising the detection scheme, it is possible to use feedback cooling to reach the ground state [41]. Optimal detection is discussed in Chapter 7.

### 2.3.3 Electromechanical Cooling

If the trapped particle has some charge  $q$ , it is possible from [42] to use an RLC circuit to cool the motion of the particle. This has the benefit of avoiding the internal heating of the particle through absorption of laser photons. Fig. 2.8 shows the diagram of the electro cooling set-up. A spherical particle with mass  $m$  is trapped in a potential  $V(z)$  with trapping frequency  $\omega_z$ . The work by Goldwater et al. assumes that the particle is levitated in a Paul trap, but an optical trap could also be used as demonstrated in [43]. The particle is trapped between two plates separated by a distance  $d$  and with a capacitance  $C$ , connected in series with a resistor  $R$  and inductor  $L$ . We can derive the equations of motion of the

particle as,

$$\frac{dz}{dt} = \frac{p}{m} \quad (2.3.2a)$$

$$\frac{dp}{dt} = -\frac{\partial}{\partial z}V(z) - \frac{\Gamma Lq^2}{md^2}p \quad (2.3.2b)$$

where the damping rate is  $\Gamma = R/L$ . From Eq. (2.3.2b) which we find the adiabatic damping rate

$$\gamma_{\text{ad}} = \frac{\Gamma Lq^2}{md^2}. \quad (2.3.3)$$

If the circuit is on resonance with the particle motion  $\omega_{\text{LC}} = \omega_z$  where  $\omega_{\text{LC}} = 1/\sqrt{LC}$ , the particle motion cancels the inductance boosting the damping rate. This resonance damping rate is given by

$$\gamma_{\text{res}} = \left(\frac{q\eta}{d}\right)^2 \frac{R_{\text{eff}}}{m} \quad (2.3.4)$$

where the effective resistance is  $R_{\text{eff}} = \omega_z LQ_f$  when connected in parallel, with quality factor  $Q_f = \omega_z/\Gamma$ , and  $\eta$  is a geometric factor.

By detecting the particle motion via the voltage across the plates  $U$ , we can apply a feedback signal to further cool the motion of the particle. By passing the signal to an amplifier with a gain  $G$ , we can apply a voltage to the particle,

$$U_{\text{fb}} = (1 - G)U \quad (2.3.5)$$

where we ensue a suitable phase shift between  $GU$  and  $U$  to achieve cooling. Thermal fluctuations will lead to an added noise in the amplifier based on the bandwidth  $B = \Delta\omega/(2\pi)$  where  $\Delta\omega$  is the interval in the noise frequency modes [44]. The voltage noise added by the amplifier

$$\nu_{\text{fb}} = \sqrt{4k_B T_{\text{fb}}^n R_{\text{amp}} B} \quad (2.3.6)$$

where  $T_{\text{fb}}^n$  is the noise temperature,  $R_{\text{amp}}$  is the resistance of the amplifier, and  $B$  is its bandwidth. From this, and the uncorrelated voltage noise  $\nu_R$ , we can find the total noise,

$$\nu_{\text{total}} = \sqrt{(1 - G)^2 \nu_R^2 + G^2 \nu_{\text{fb}}^2} \quad (2.3.7)$$

and the equilibrium center of mass temperature is

$$T_{\text{CoM}} = (1 - G)T_R + \frac{G^2}{1 - G} T_{\text{fb}}^n \quad (2.3.8)$$

where  $T_R$  is the temperature of the circuit. By using state-of-the-art amplifiers with a noise temperature below  $20\mu\text{K}$  and circuit temperatures  $T_R = 5\text{mK}$ , it is possible to cool the center of mass temperature below  $100\mu\text{K}$  reaching the motional ground state.

### 2.3.3.1 Control of Particle Charge

In order to control the motion of the particle via its charge, we must be able to control the charge on the particle. To maximise the amount of control we have over the particles, we need to ensure a high charge on the particle. We can charge the particle in numerous ways.

We can apply a charge to the particle by using an ion beam. In this case, the maximum charge on the particle is achieved when the net current on the particle is 0 [45]. We can also make use of an electron beam to apply a negative charge to the particle. In this case, the charging rate is given by the sum of currents incident on the particle. This includes the current of the beam itself, the current produced by electrons and ions from residual gas molecules, the thermal electron emission current, and any other possible current sources [46].

By applying a high voltage to a conductor in a fluid, such as air, a current will flow ionising the fluid as it does in a process known as corona discharge. This produces ions that bombard the particle charging it. The saturation charge that can be applied to a spherical particle of radius  $R$  in a mono-ionized electric field was calculated for dielectric particles by Pauthenier and Moreau-Hanot as [47],

$$q_{\max} = 4\pi\epsilon_0 R^2 E_0 \frac{3\epsilon_r}{\epsilon_r + 2} \quad (2.3.9)$$

where  $E_0$  is the magnitude of the electric field. From Eq. (2.3.9), we can find an equation for the rate at which the particle will be charged,

$$q(t) = q_{\max} \frac{1}{1 + \tau_c/t} \quad (2.3.10)$$

where  $t$  is the time and  $\tau$  is the charging time constant given by,

$$\tau_c = \frac{4\epsilon_0}{\rho b} \quad (2.3.11)$$

where  $\rho$  is the space-charge density, and  $b$  is the mobility of ions [48].



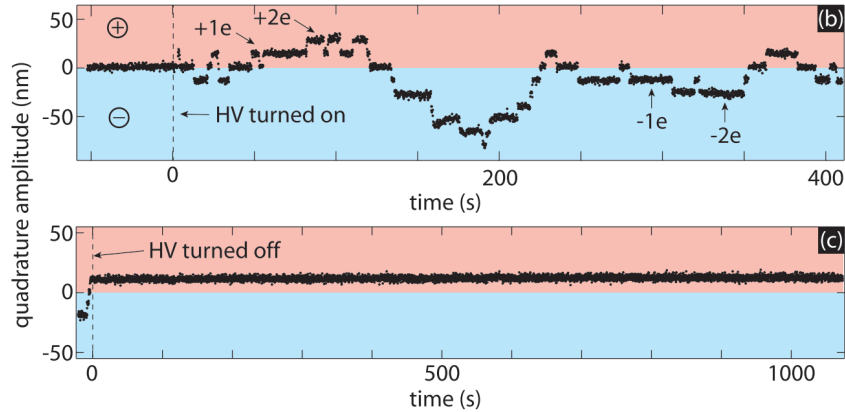


Figure 2.9: Oscillation amplitudes of a particle from a quadrature detector. The oscillations are driven by a 10V voltage. The high-voltage source is activated at  $t = 0$  in the top panel. The amplitude of the oscillations changes in integer multiples as the charge on the particle changes. In the bottom panel, the high-voltage source is switched off at  $t = 0$  and we see the amplitude of the particle’s motion has stabilised.

This can, in principal, be applied to an optically levitated system by feeding a 7kV potential into the chamber by use of a bare wire. This ionises gas molecules close to the particle charging it. The charge on the particle will make random jumps in integer units of the elementary charge while the voltage is applied, and then will maintain the charge indefinitely while the potential is switched off as shown in Fig. 2.9 [49].

By illuminating a nearby metal with UV light we are able to increase the negative charge on a particle. This works because the UV photons will have sufficient energy to knock electrons from the surface of the metal such that they fall onto a nearby levitated nano-particle. This was used in [50] to fully neutralise the positive charge on a trapped particle. In that work a diamagnetic particle was trapped in a hybrid magneto-gravitational trap constructed of four pole pieces made of a ferromagnetic material. Much of the charge on the particle was adjusted by exposing it to an ionizing radiation source until no motion of the particle in an oscillating electric potential is detected. Finally, the nearby pole pieces were

illuminated with UV light that knocked electrons on to the particle.

### 2.3.4 Cavity Cooling

The main principle of cooling particle motion is to increase the trap stiffness as the particle moves away from the centre, and to decrease it as the particle moves towards the centre. This is achieved in feedback cooling by modulating the laser power with twice the frequency of the particle oscillation. By setting up a high-finesse optical cavity with an off-resonant laser field, it is possible that the optical potential will be steeper as the particle ascends the potential than when it descends.

A sub-wavelength object in a cavity will experience an optical potential given by,

$$U_{\text{opt}} = -\hbar U_0 |E_0|^2 f^2(\mathbf{r}) \quad (2.3.12)$$

where  $E_0$  is the field amplitude, and  $f(\mathbf{r})$  describes the cavity mode function at the point  $\mathbf{r}$ , and is given by  $f(z) = \cos kz$  for a cavity composed of wide plane parallel mirrors. The particle will create an effective increase to the cavity length due to the index of its refraction, thus shifting the cavity resonance by  $U_0 f^2(\mathbf{r})$ , where the coupling constant is

$$U_0 = \frac{\alpha \omega_L}{2\epsilon_0 V} \quad (2.3.13)$$

and  $V$  is the cavity's mode volume,  $\omega_L$  is the frequency of the laser light, and  $\alpha$  is the particle's polarisability. If the frequency of the incident laser  $\omega_L$  is less than the cavity's resonance frequency  $\omega_C$ , any particle with a refractive index greater than 1 will shift the cavity resonance frequency closer to the laser frequency, and thus increase the power of the cavity field.

As the particle moves along the cavity it changes the shift of the resonance frequency leading to a time-dependant intensity modulation. The intensity is maximal when the particle moves away from the anti-node of the cavity standing wave, leading to an increase in the trap stiffness, and is lowest as the particle moves towards the anti-node, leading to a decrease in trap stiffness. As a result, the particle gains less energy moving towards the centre of the trap than it loses when moving out of the trap [51].

A more recent method of cooling the particle motion is presented in [19]. In this work, a sub-wavelength particle is trapped at an intensity minimum of the cavity field. Here, dipole scattering into the cavity mode is prevented by destructive interference in the cavity. Therefore, only inelastic scattered photons are allowed. Scattering that increases the particle's kinetic energy are suppressed while scattering that decreases the energy are enhanced. Thus the particle will lose kinetic energy until it reaches the ground state

### 2.3.5 Cooling in an Optical Lattice

It is possible to reach low occupation numbers, and thus achieve high degrees of cooling for a particle trapped in an optical lattice. A particle is trapped at the anti-node of a standing wave produced by a retro-reflected laser with angular frequency  $\omega_0$ . By using phase modulation, weak side-bands are introduced at frequencies  $\omega_0 \pm \omega_1$ . These side-bands produce intensity gradients at the position of the nano-particle thus inducing forces on the particle with opposite direction to each other. In order to achieve cooling, the magnitudes of these forces must be modulated via the modulation of the side-band magnitudes [52].

### 2.3.6 Comparison of Cooling Schemes

All the cooling schemes discussed above are useful for specific circumstances. However, in this section we discuss their applicability to the interferometry experiments to be described in Chapter 5.

Using the scattering force based cooling perhaps the simplest method. This however, requires cooling beams for each direction of the particle's motion. Because we are only interested in cooling the particle's motion in the  $z$  axis for our interferometry experiment. This means that we can achieve all necessary cooling with only one cooling beam.

As we shall see in Chapter 5, the proposed interferometry experiment goes to great lengths to minimise decoherence during the particle's free evolution. Due to the effect of Coulomb coupling to nearby metallic surfaces will introduce another source of decoherence during the particle's free-fall [53] any cooling system reliant

on the particle having an electric charge is likely to be useful. Although it is possible to control the charge on the particle, thus charging it to cool then de-charging for the free-fall, the most efficient methods of controlling the charge prevent us from working in a vacuum which is needed to reduce the decoherence from collisions with gas molecules.

The presence of the dielectric in an optical cavity shifts the frequency of the cavity mode. This means that using a cavity to produce the standing wave for the phase grating that will be used to induce the interference pattern will likely introduce a further decoherence within the standing wave. In an Earth-based experiment, where the particle will fall under the influence of gravity, we could use a cavity to trap and cool the particle. Then, after some distance  $gt_1^2/2$  below the trapping laser, we have our standing wave grating that is not produced by a cavity. This standing-wave grating can be produced by a retro-reflected laser pulse which would induce some motional perturbation to the particle similar to the cooling or heating effect of the cavity. However, due to the fact that the laser is not reflected many times, as it would be in a cavity, these effects are much smaller. Alternately, the standing-wave could be generated by counter propagating lasers which would remove this effect altogether. For a space-based experiment that would be needed to allow for long free-fall times required by larger particles, this is not practical as the particle will not fall during its free evolution meaning that the trapping laser will need the same set-up as the grating laser. Cavity cooling has managed to reach the ground state [19] ensuring that it can achieve the necessary localisation for an interferometry experiment.

Parametric feedback cooling does not require any cooling beams, working by modulating the intensity of the trapping beam. This would decrease the complexity of the set-up making it beneficial for a space based mission where size and weight greatly increases the cost of launching the experiment. We also avoid the need for an optical cavity or charging the particle. Feedback cooling has also been shown to achieve cooling close to the ground state [54] which allows us to reach the necessary localisation for our proposed interferometry experiments.

In principle, the simplest method to use would be the lattice cooling presented in [52] which uses a retro-reflected laser to produce a standing wave. This is the

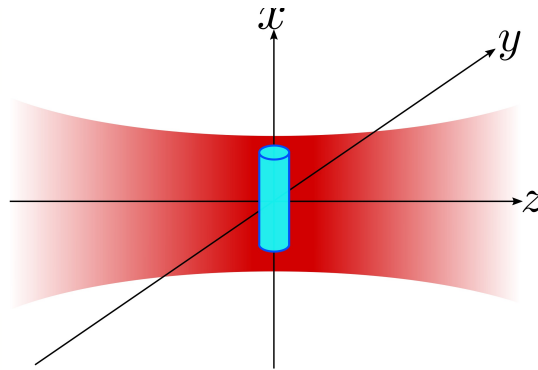


Figure 2.10: A nano-rod levitated in a standing wave trap. The rod orients itself such that its length lines up with the polarisation direction.

same set-up as we will use to produce the phase grating in the interferometry experiment allowing us to use the same set-up. It also reaches occupation numbers as low as 0.85 ensuring the necessary localisation for interferometry experiments.

## 2.4 Trapping different shaped particles

Optical levitation is most often performed with spherical particles as their symmetry means that there are only three degrees of freedom to consider. However, we show at the end of Chapter 6 that there is a limit to the size of the particle we can use for interferometry. The issue with spherical particles seems to be the size in the direction that the laser propagates. Using a particle that can be arbitrarily large in either, or both, of the radial axes of the laser, but still small in the longitudinal axis, could solve this problem allowing us to access greater masses. In recent years, it has become more common to trap and cool particles of different shapes. This leads to adding rotational degrees of freedom on top of the translational ones. This section discusses trapping and cooling some of the different shapes of particles that could be used.

### 2.4.1 Rods

A cylindrical rod contains the desired properties. We can describe the rod by its length  $L$  and its radius  $R$ . To increase the mass, we can either increase  $L$  or increase  $R$ . In principle it we could increase the radius of the rod until its diameter is close to the wavelength of the grating laser, and then increase the length of the rod so that we continue to increase the mass. It has also been shown that the rotational states of a nano-rod could be used to test large mass superpositions [55], detect Casimir torque [56], among other proposals. A nano-rod cooled to a tight orientation then released will enter a superposition of all possible orientations until integer units of the revival time where constructive interference recovers the initial, tightly oriented state.

This rod will have five degrees of freedom. Its center of mass positional  $(x, y, z)$  and rotational  $(\theta_y, \theta_z)$  motions. by trapping the rod in counter propagating beams that are linearly polarised in the same direction, the particle orients itself along the axis of polarisation, thus trapping all degrees of freedom. An example of this is shown in Fig. 2.10 This occurs as a result of a torque induced by the difference in angle between the direction of field polarisation and the induced dipole moment. When the rod is angled away from the direction of polarisation, the dipole moment of the rod, given by  $\mathbf{P} = \langle \alpha \rangle \mathbf{E}$  sits at an angle  $\theta$  from the polarisation direction. This induces a torque proportional to  $\theta$  on the rod given by  $\boldsymbol{\tau} = \mathbf{P} \times \mathbf{E}$  [57]. If, however, the trapping light is circularly polarised, the particle will begin to precess around the  $z$  axis whilst maintaining the trap in the  $y$  and  $z$  directions [58].

We are also able to track the motion and rotation of the rod. In the Fourier transform of a signal from the scattered light, such as that shown in Fig. 2.11, we see two distinct peaks. This first corresponds to the center of mass motion of the particle along the laser propagation axis  $\nu_{\text{trans}} = 2v_z/\lambda$ , where  $v_z$  is the velocity in the  $z$  direction. The second frequency peak is a twice the rotational frequency  $\nu_{\text{rot}} = 2f_{\text{rot}}$  [59]. This can then be used to inform our cooling method allowing us to cool both the motional, and rotational degrees of freedom of a trapped nano rod.

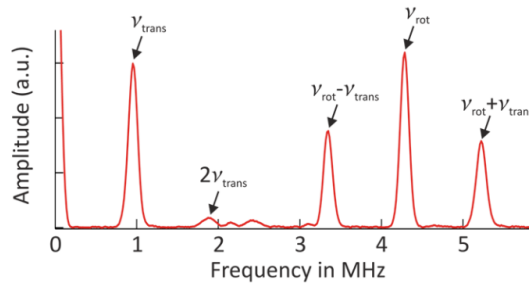


Figure 2.11: An example power spectral density of the recorded signal showing the peaks relating to its transverse motion  $\nu_{\text{trans}}$  and its rotational motion  $\nu_{\text{rot}}$  [59].

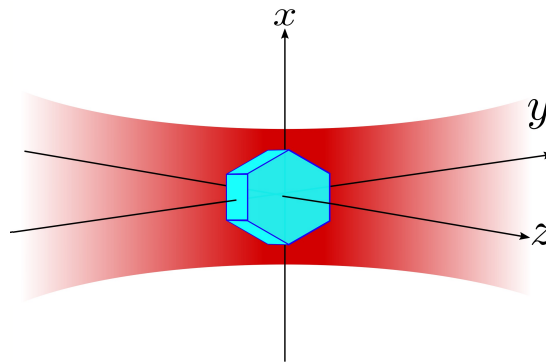


Figure 2.12: An image of a hexagon showing the five degrees of freedom that are observed in [60].

## 2.4.2 Hexagonal Disks

An alternative geometry we can use are hexagonal disks. These are thin plates in the  $z$  axis, but are wide hexagons in the  $x-y$  plane. This allows us to manufacture disks with a thickness on the scale of the grating laser wavelength, but still be able to extend the size of the particle in both the  $x$  and  $y$  directions. This is different to the rod that could only extend in the direction that its length was pointed in. These plates have six degrees of freedom, the usual center of mass motion  $(x, y, z)$ , and three rotational degrees of freedom  $(\theta_x, \theta_y, \theta_z)$ . It should be noted that due to the hexagonal shape of the disks, a rotation of  $\pi/3$  radians gives the same shape due to its six lines of symmetry in this rotational axis.

Particle of this geometry can be used to detect gravitational waves as is being

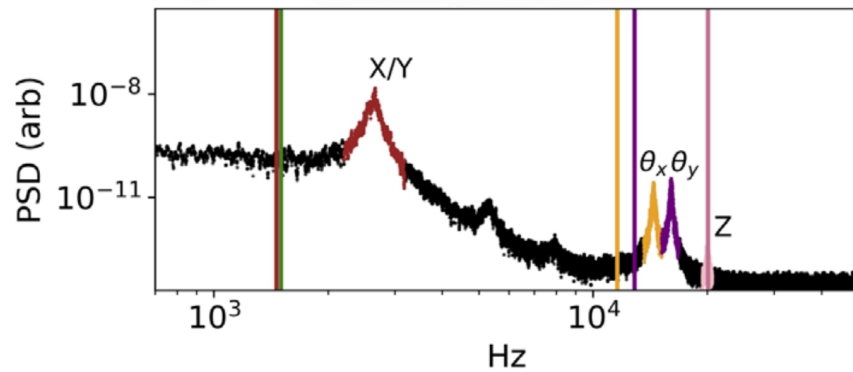


Figure 2.13: Power spectral density recorded from a QPD of a hexagonal plate with a thickness of 300nm and vertex-to-vertex diameter of  $2.5\mu\text{m}$  reproduced from [60]. Although we consider all three rotational degrees of freedom, only the  $\theta_x$  and  $\theta_y$  degrees of freedom are observed. This is likely a result of the fact that the  $\theta_z$  motion is not driven as a mechanical mode. We see in Sec. 7.2.5 that if there is motion in this axis, we will be able to detect it. The coloured lines indicate the calculated frequencies related to the motion in each degree of freedom from a finite-element simulation and show qualitative agreement.



done by a team at Northwestern University [60]. Disks of various thicknesses and diameters have been studied to develop trapping and cooling techniques. We can see in Fig. 2.13 the power spectral densities recorded by a quadrant photodetector (QPD) of a hexagonal disk levitated in a standing wave trap consisting of linearly polarised counter propagating beams with a waist of  $12\mu\text{m}$ . The disk has a thickness of  $300\text{nm}$  and vertex-to-vertex diameter of  $2.5\mu\text{m}$ . Peaks form in the PSD corresponding to the five degrees of freedom  $(x, y, z, \theta_x, \theta_y)$ . This allows us to track and cool all five degrees of freedom. In Chapter 7 we discuss methods for optimal position and rotational detection for hexagons, such that they can be maximally cooled. We also discuss how we can apply hexagonal plates to our theory of an interferometry experiment.

# Chapter 3

## Background Quantum Mechanics

In this chapter we introduce the necessary quantum mechanical ideas that will be used throughout the rest of this work. We begin by introducing the density operator  $\hat{\rho}$  that we use to describe quantum systems. Then we introduce the Wigner function as a phase-space description of the system that will be useful in describing the propagation of the quantum system through the interferometer. The effects of decoherence is given next as this is a phenomena that affects all quantum systems that are not completely decoupled from the environment and therefore must be considered.

### 3.1 Density Operator

Much of quantum mechanics can be described by the use of state vectors in Hilbert space, such as  $|\psi\rangle$ . This state vector contains the full knowledge of a pure quantum system and evolves according to the Schrödinger equation

$$i\hbar \frac{\partial}{\partial t} |\psi\rangle = \hat{H} |\psi\rangle \quad (3.1.1)$$

where  $\hat{H}$  is the Hamiltonian of the system. This Dirac notation formulation allows us to simply write a superposition of states as the sum of states,

$$|\psi\rangle = \sum_{i=1} c_i |\psi_i\rangle \quad (3.1.2)$$

where  $c_i$  are complex amplitudes that fulfil the normalisation condition

$$\sum_{i=1} |c_i|^2 = 1. \quad (3.1.3)$$

If our state  $|n\rangle$  refers to a particle in the  $n$ th energy level of a harmonic oscillator, as shown in Fig. 3.1, we can write the Hamiltonian as

$$\hat{H} = \frac{\hat{P}^2}{2m} + \frac{m\omega^2 \hat{x}^2}{2} \quad (3.1.4)$$

where  $\omega$  is the angular frequency and is related to the spring constant via  $\omega = \sqrt{k/m}$ . By solving the time-independent Schrödinger equation, we can show that the energy of a particle in the  $n$ th energy level is

$$E_n = \left(n + \frac{1}{2}\right) \hbar\omega \quad (n = 0, 1, 2, 3, \dots). \quad (3.1.5)$$

In position representation, we find the wave-function for each energy level to be

$$\psi_n(x) = \langle x|n\rangle = \left(\frac{\sqrt{m\omega}}{n! 2^n \sqrt{\pi\hbar}}\right)^{1/2} H_n\left(x\sqrt{\frac{m\omega}{\hbar}}\right) \exp\left(-\frac{m\omega x^2}{2\hbar}\right) \quad (3.1.6)$$

where  $H_n(x)$  is the Hermite polynomial of order  $n$  [61].

However, this state vector formalism is insufficient to capture a statistical mixture of states. A statistical mixture, sometimes simply called a mixed state, is a mixture of pure states that can be described by the state vector formalism. For example, an ensemble of silver atoms all prepared with the same spin direction is a pure state with state vector  $|\alpha\rangle$ , but if there is a mixture of spin directions present in the ensemble, such that some have their spin described by the state  $|\alpha\rangle$  and the rest by the state  $|\beta\rangle$  with relative weights  $w_\alpha$  and  $w_\beta$ , we have a mixed state. A mixed state cannot be described by the usual linear superposition equation  $|\alpha\rangle = c_- |-\rangle + c_+ |+\rangle$ . To describe these mixed states, we must include a probability weighting  $w_i$  distinct from the expansion coefficients  $c_\pm$ . The probability weightings are real numbers that fulfil the normalisation condition

$$\sum_i w_i = 1. \quad (3.1.7)$$

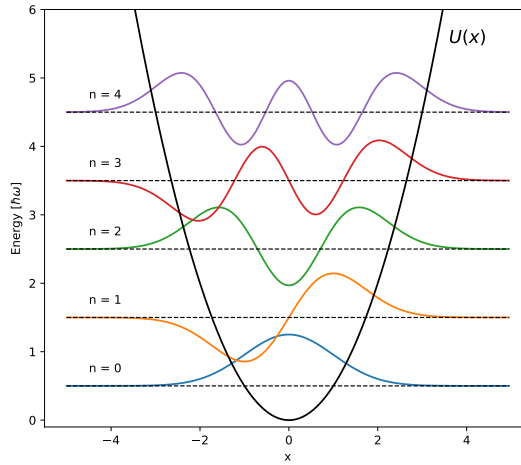


Figure 3.1: Wave functions for the position of a particle in a quantum harmonic oscillator  $\psi_n(x)$  in the first five energy levels. The probability distribution of the measured particle location is  $p(x) = |\psi_n(x)|^2$ . The energy is given on the left axis in units of  $\hbar\omega$  and the right axis gives the number of the energy level. The black line gives the potential  $U(x)$ .

We are still able to define the expected value of some observable  $\hat{A}$  on a mixed state quantum system. This is given by the ensemble average defined as,

$$[\hat{A}] = \sum_i w_i \langle \alpha^{(i)} | \hat{A} | \alpha^{(i)} \rangle \quad (3.1.8)$$

where  $\langle \alpha^{(i)} | \hat{A} | \alpha^{(i)} \rangle$  is the expectation value of  $\hat{A}$  on the state  $|\alpha^{(i)}\rangle$ . From Eq. (3.1.8) we can see that we weight the expectation value by the probability that the measured state in the ensemble is described by  $|\alpha^{(i)}\rangle$ .

By inserting two completeness relations  $\sum_n |n\rangle \langle n| = 1$  into the definition of the expected value,

$$\langle \hat{A} \rangle = \sum_a \sum_b \langle \alpha | a \rangle \langle a | \hat{A} | b \rangle \langle b | \alpha \rangle \quad (3.1.9)$$

we can rewrite Eq. (3.1.8) as,

$$[\hat{A}] = \sum_a \sum_b \sum_i w_i \langle b | \alpha^{(i)} \rangle \langle \alpha^{(i)} | a \rangle \langle a | \hat{A} | b \rangle. \quad (3.1.10)$$

Because we are able to factor out the property of the mixed state that does not depend on the observable  $\hat{A}$ , we define the density operator as,

$$\hat{\rho} = \sum_i w_i |\alpha^{(i)}\rangle \langle \alpha^{(i)}| \quad (3.1.11)$$

with corresponding density matrix

$$\rho = \langle b | \hat{\rho} | a \rangle = \sum_i w_i \langle b | \alpha^{(i)} \rangle \langle \alpha^{(i)} | a \rangle. \quad (3.1.12)$$

We can use the density operator to find the expectation value of an observable,

$$\begin{aligned} [\hat{A}] &= \sum_a \sum_b \langle b | \hat{\rho} | a \rangle \langle a | \hat{A} | b \rangle \\ &= \text{tr}(\hat{\rho} \hat{A}) \end{aligned} \quad (3.1.13)$$

where  $\text{tr}(x)$  is the trace of  $x$  [62].

For a pure state,  $|\psi\rangle$  with weight  $w = 1$ , the density operator takes the form,

$$\hat{\rho} = |\psi\rangle \langle \psi|. \quad (3.1.14)$$

We can use the definitions of the density operator from a mixture and pure state to show the fundamental differences between an ensemble of states and a superposition. First, we define the pure states  $|\psi_1\rangle = \begin{pmatrix} 1 & 0 \end{pmatrix}^T$  and  $|\psi_2\rangle = \begin{pmatrix} 0 & 1 \end{pmatrix}^T$ , each with relative weighting 1/2. Recall the definition of the density operator Eq. (3.1.11) and the definition of the outer product,

$$|u\rangle \langle v| = \begin{pmatrix} u_1 \\ u_2 \end{pmatrix} \begin{pmatrix} v_1 & v_2 \end{pmatrix} = \begin{pmatrix} u_1 v_1 & u_1 v_2 \\ u_2 v_1 & u_2 v_2 \end{pmatrix} \quad (3.1.15)$$

we find the ensemble density operator to be

$$\hat{\rho}_{\text{ensemble}} = w_1 |\psi_1\rangle \langle \psi_1| + w_2 |\psi_2\rangle \langle \psi_2| = \frac{1}{2} \begin{pmatrix} 1 & 0 \\ 0 & 1 \end{pmatrix}. \quad (3.1.16)$$

Alternately, if we have the pure state in a superposition  $|\psi\rangle = (|\psi_1\rangle + |\psi_2\rangle)/\sqrt{2}$  and use the definition from Eq. (3.1.14) we find,

$$\hat{\rho}_{\text{superposition}} = \frac{1}{2} \begin{pmatrix} 1 & 1 \\ 1 & 1 \end{pmatrix}. \quad (3.1.17)$$

The difference between these two density operators is in the off diagonals. The off diagonals measure the coherence between two of the basis vectors. When the off diagonals are not 0, we are able to observe quantum interference [63]. If we look at the pure state  $\hat{\rho}_{\text{superposition}} = \frac{1}{\sqrt{2}}(|\psi_1\rangle + |\psi_2\rangle) \times \frac{1}{\sqrt{2}}(\langle\psi_1| + \langle\psi_2|)$  and find the expectation value of the density operator in the basis of some observable  $\hat{A}$  with eigenvectors  $|a\rangle$ , we find,

$$\begin{aligned} \langle a | \hat{\rho}_{\text{superposition}} | a \rangle &= \frac{1}{2} (\langle a | \psi_1 \rangle \langle \psi_1 | a \rangle + \langle a | \psi_1 \rangle \langle \psi_2 | a \rangle + \langle a | \psi_2 \rangle \langle \psi_2 | a \rangle + \langle a | \psi_2 \rangle \langle \psi_1 | a \rangle) \\ &= \frac{1}{2} (|\langle a | \psi_1 \rangle|^2 + |\langle a | \psi_2 \rangle|^2 + \langle a | \psi_1 \rangle \langle a | \psi_2 \rangle^* + \langle a | \psi_2 \rangle \langle a | \psi_1 \rangle^*). \end{aligned} \quad (3.1.18)$$

The values  $|\langle a | \psi_i \rangle|^2$  are simple probability amplitudes squared and give a constant real number. The terms  $\langle a | \psi_1 \rangle \langle a | \psi_2 \rangle^*$  and  $\langle a | \psi_2 \rangle \langle a | \psi_1 \rangle^*$  lead to interference between the states. Considering the statistical mixture  $\hat{\rho}_{\text{ensemble}} = w_1 |\psi_1\rangle \langle \psi_1| + w_2 |\psi_2\rangle \langle \psi_2|$ , we find,

$$\begin{aligned} \langle a | \hat{\rho}_{\text{ensemble}} | a \rangle &= w_1 \langle a | \psi_1 \rangle \langle \psi_1 | a \rangle + w_2 \langle a | \psi_2 \rangle \langle \psi_2 | a \rangle \\ &= w_1 |\langle a | \psi_1 \rangle|^2 + w_2 |\langle a | \psi_2 \rangle|^2 \end{aligned} \quad (3.1.19)$$

where we only have the probability amplitude terms leading to no interference between terms.

### 3.1.1 Time Evolution of the Density Operator

The time dependant Schrödinger equation is,

$$\begin{aligned} i\hbar \frac{\partial}{\partial t} |\psi\rangle &= \hat{H} |\psi\rangle \\ -i\hbar \frac{\partial}{\partial t} \langle\psi| &= \langle\psi| \hat{H} \end{aligned} \quad (3.1.20)$$

in ket and bra space respectively. Using Eq. (3.1.20) we can apply the differential operator to the density operator leading to the Von Neumann equation of motion,

$$\begin{aligned} i\hbar \frac{\partial}{\partial t} \hat{\rho} &= i\hbar \sum_i w_i \left( \frac{\partial}{\partial t} |\psi_i\rangle \langle\psi_i| + |\psi_i\rangle \frac{\partial}{\partial t} \langle\psi_i| \right) \\ &= \sum_i w_i \left( \hat{H} |\psi_i\rangle \langle\psi_i| - |\psi_i\rangle \langle\psi_i| \hat{H} \right) \\ &= -\frac{i}{\hbar} [\hat{H}, \hat{\rho}]. \end{aligned} \quad (3.1.21)$$

which is the quantum equivalent of the Liouville equation which is given as  $\partial_t \rho = -\{\rho, H\}$  in Poisson bracket notation. The classical Liouville equation describes the time dependence of the distribution  $\rho(q, p, t)$  describing an ensemble of systems in phase space [64].

## 3.2 The Phase Space Description

Introduced by Wigner in 1932 the Wigner function is a powerful tool allowing us to view a quantum system in terms of its phase-space [65]. A classical phase-space describes the likelihood that a system will have a certain momentum and position at any given time. For example, the phase-space for some simple harmonic motion, like a pendulum, would be a circle around the origin. The Wigner function acts almost as an analogy to this. Discussions on the Wigner function can be found in standard quantum optics textbooks [4, 66] and a review paper by Case [67]. This section summarises these discussions relevant to our interferometry experiment.

We make the move to considering observables of continuous spectra. Instead of an observable  $\hat{A}$  having specific discrete eigenvectors  $|a_i\rangle$  with corresponding eigenvalues  $a_i$ , continuous variable, such as position  $\hat{x}$  will have continuous eigenvectors and values. Many of the operations we perform on discrete systems have corresponding operations in continuous systems. For summations, we use integration in the continuous regime, the probability of a system existing in a narrow interval  $dx$  is given by  $|\langle x|\psi\rangle|^2 dx$ , and we can re-write state vectors as wave-functions in a given basis by  $\psi(x) = \langle x|\psi\rangle$ . The inverse Weyl transform, sometimes referred to as the Wigner-Weyl transform, is given by [68],

$$\tilde{A}(x, p) = \int \exp\left[\frac{-ipy}{\hbar}\right] \left\langle x + \frac{s}{2} \left| \hat{A} \right| x - \frac{s}{2} \right\rangle ds \quad (3.2.1)$$

and converts an operator  $\hat{A}$  into a function of phase-space  $\tilde{A}(x, p)$ . The Wigner function is a special case of the Wigner-Weyl transform defined as the Wigner-Weyl transform of the density operator divided by Planck's constant [67],

$$W(x, p) = \frac{\tilde{\rho}(x, p)}{\hbar} = \int \frac{1}{\hbar} \exp\left[\frac{-ips}{\hbar}\right] \left\langle x + \frac{s}{2} \left| \hat{\rho} \right| x - \frac{s}{2} \right\rangle ds. \quad (3.2.2)$$

Unlike a regular wave function, which can only assign a value to either position or momentum at any given time, the Wigner function assigns a value to the full  $(x, p)$  parameter space. However, unlike a traditional probability function, the value of the Wigner function can take negative values, meaning it should only be viewed as a pseudo-probability function. We can recover a probability function from the Wigner function, but only for one axis of the phase-space. We achieve this by integrating over the other variable. After this, we will have a purely positive function of the form  $p(x) = |\psi(x)|^2 = \int w(x, p) dp$  if we integrate out the momentum term. If we integrate out the position term, we will recover the equivalent expression for the momentum term.

This is more clearly seen if we assume a pure state such that  $\hat{\rho} = |\psi\rangle\langle\psi|$  and  $\langle x | \hat{\rho} | x \rangle = \psi(x)\psi^*(x)$ ,

$$W(x, p) = \frac{1}{h} \int \exp\left[\frac{-ips}{\hbar}\right] \psi\left(x + \frac{s}{2}\right) \psi^*\left(x - \frac{s}{2}\right) ds. \quad (3.2.3)$$

Then, if we integrate over the momentum  $p$ , we find,

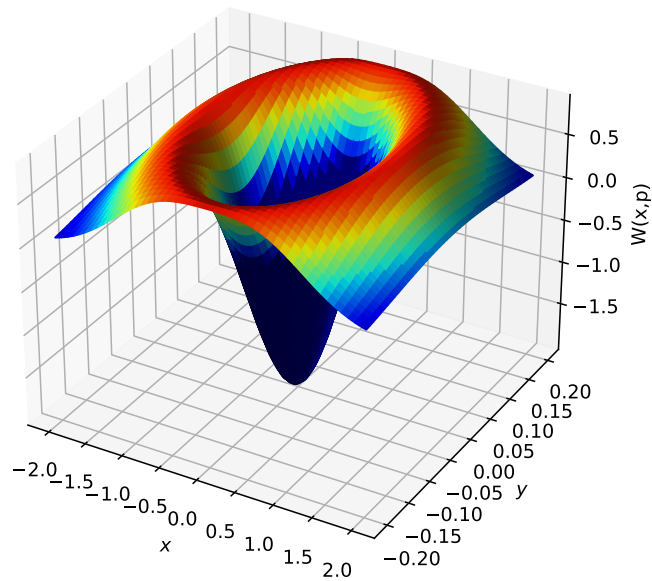
$$\begin{aligned} \int W(x, p) dp &= \frac{1}{h} \iint \exp\left[\frac{-ips}{\hbar}\right] \psi\left(x + \frac{s}{2}\right) \psi^*\left(x - \frac{s}{2}\right) ds dp \\ &= \frac{1}{h} \int \psi\left(x + \frac{s}{2}\right) \psi^*\left(x - \frac{s}{2}\right) h\delta(s) ds \\ &= \psi(x)\psi^*(x) = |\psi(x)|^2 \end{aligned} \quad (3.2.4)$$

where we have made use of the relation  $\int \exp[-ips/\hbar] dp = h\delta(s)$ . This formulation recovers the Born rule  $P(x) = |\psi(x)|^2$  and thus gives the probability of finding the system in the state  $x + \delta x$ . We can perform the equivalent operation integrating over the position variable to find the probability function with respect to the system's momentum. An example of the Wigner function in the  $n = 1$  energy level of a harmonic oscillator is given in Fig. 3.2.

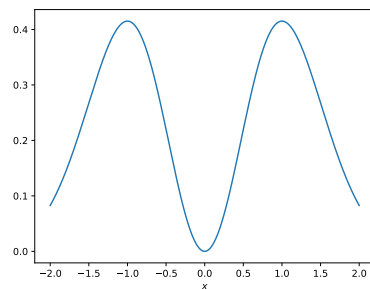
### 3.2.1 Time Dependence of the Wigner Function

In order to find the equation of motion of the Wigner function, we must differentiate it with respect to time. Doing this to the Wigner function of a pure state

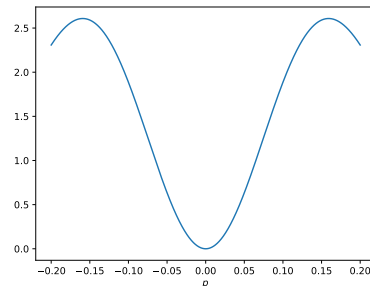




(a) Wigner Function



(b) Position probability function



(c) Momentum probability function

Figure 3.2: (a) The Wigner function for a particle in the  $n = 1$  energy level of a harmonic oscillator. We can see clearly that the Wigner function here is negative for most values of  $x$  and  $p$ . (b) The probability density function of measuring the particle at some location found by integrating the Wigner function over the momentum  $p(x) = \int_{-\infty}^{\infty} W(x,p)dp$ . (c) The probability density function of measuring the particle with some momentum found by integrating the Wigner function over the position  $p(p) = \int_{-\infty}^{\infty} W(x,p)dx$ . These plots are found by setting  $m = \omega = \hbar = 1$ .

from Eq. (3.2.3), we find

$$\frac{\partial}{\partial t}W(x, p) = \frac{1}{\hbar} \int \exp\left[\frac{-ips}{\hbar}\right] \left[ \psi\left(x + \frac{s}{2}\right) \frac{\partial}{\partial t}\psi^*\left(x - \frac{s}{2}\right) + \frac{\partial}{\partial t}\psi\left(x + \frac{s}{2}\right) \psi^*\left(x - \frac{s}{2}\right) \right]. \quad (3.2.5)$$

Recalling the time dependant Schrödinger equation,

$$\frac{\partial\psi(x, t)}{\partial t} = -\frac{\hbar}{2im} \frac{\partial^2\psi(x, t)}{\partial x^2} + \frac{U(x)}{i\hbar}\psi(x, t), \quad (3.2.6)$$

we can rewrite Eq. (3.2.5) as,

$$\frac{\partial W}{\partial t} = \frac{\partial W_T}{\partial t} + \frac{\partial W_U}{\partial t} \quad (3.2.7)$$

where

$$\begin{aligned} \frac{\partial W_T}{\partial t} = \frac{1}{4\pi im} \int \exp\left[\frac{-ips}{\hbar}\right] & \left[ \psi\left(x + \frac{s}{2}\right) \frac{\partial^2}{\partial x^2}\psi^*\left(x - \frac{s}{2}\right) \right. \\ & \left. + \frac{\partial^2}{\partial x^2}\psi\left(x + \frac{s}{2}\right) \psi^*\left(x - \frac{s}{2}\right) \right] ds \end{aligned} \quad (3.2.8)$$

and

$$\begin{aligned} \frac{\partial W_U}{\partial t} = \frac{1}{4\pi im} \int \exp\left[\frac{-ips}{\hbar}\right] & \left[ U\left(x + \frac{s}{2}\right) - U\left(x - \frac{s}{2}\right) \right] \\ & \psi\left(x + \frac{s}{2}\right) \psi^*\left(x - \frac{s}{2}\right) ds. \end{aligned} \quad (3.2.9)$$

Eqs. (3.2.7), (3.2.8), and (3.2.9) is equivalent to solving the Schrödinger equation due to the fact that the wave function and corresponding Wigner function have a one-to-one relationship apart from an overall phase.

### 3.2.2 Husimi Q-Function

The Wigner function discussed above is not the only phase-space description of quantum mechanics. Here we focus on a brief introduction to the Husimi Q-function as an alternative phase-space description based on the complex eigenvalue for the annihilation operator  $\alpha = \alpha_r + \alpha_i i$ . The derivation presented here

is short and is only intended to show that other phase-space models exists. For this section we follow the derivation given in Section 12.2 of [66].

For a harmonic oscillator, we can derive the position and momentum variables from the real and imaginary parts of  $\alpha$  as,

$$x = \sqrt{\frac{\hbar}{2m\omega}}(\alpha + \alpha^*) = \sqrt{\frac{2\hbar}{m\omega}}\alpha_r \quad (3.2.10)$$

$$p = \sqrt{\frac{m\hbar\omega}{2}}\frac{(\alpha - \alpha^*)}{i} = \sqrt{2m\hbar\omega}\alpha_i. \quad (3.2.11)$$

We then define the equivalent phase space volume element as,

$$dx dp = 2\hbar d\alpha_r d\alpha_i. \quad (3.2.12)$$

From here, we can define the Q-function of a pure state  $|\psi\rangle$  as

$$Q(\alpha_r, \alpha_i) = \frac{1}{\pi} \langle \alpha | \psi \rangle \langle \psi | \alpha \rangle. \quad (3.2.13)$$

Using the definition of the density matrix of a pure state  $\hat{\rho} = |\psi\rangle \langle \psi|$ , we can simplify Eq. (3.2.13) to,

$$Q(\alpha_r, \alpha_i) = \frac{1}{\pi} \langle \alpha | \hat{\rho} | \alpha \rangle \quad (3.2.14)$$

which shows that the Q-function is the expectation value of the density operator of the coherent state  $|\alpha\rangle$ . The main benefit of this method is that it is easy to compute expectation values from this distribution. However, we are unable to calculate the probability of one variable by integrating out the other. This is a major advantage of the Wigner function in our case as we have interest in both the momentum and position evolution of the matter-wave in our interferometer, but we are only interested in the probability of its location when we reach the stage of measurement.

### 3.3 Decoherence

Any quantum system that is not completely isolated from the environment is subject to decoherence. This is a process that reduces the coherence of the system, i.e. the off diagonals in the density operator tend to 0. As a result, this

can lead to a loss of interference and will bring the system into a single state as discussed in Sec. 3.1.

Consider a standard double slit experiment to show the effects of decoherence. We start by preparing the system  $S$  in a spatial superposition of states such that its wave function reads

$$|\psi_S\rangle = \alpha |\psi_+\rangle + \beta |\psi_-\rangle. \quad (3.3.1)$$

If the superposition interacts with another system  $|E\rangle$  such as a measurement apparatus or the environment, after a sufficient time the entangled state takes the form,

$$|\psi_{SE}\rangle = \alpha |\psi_+\rangle |E_+\rangle + \beta |\psi_-\rangle |E_-\rangle. \quad (3.3.2)$$

We can find the reduced density matrix, contains all the information of all possible measurements in  $S$ , for the system from the total density matrix of the system and environment  $\hat{\rho}_{SE}$  as

$$\begin{aligned} \hat{\rho}_S &= \text{Tr}_E(\hat{\rho}_{SE}) \\ &= |\alpha|^2 |\psi_+\rangle \langle \psi_+| + |\beta|^2 |\psi_-\rangle \langle \psi_-| \\ &\quad + \alpha\beta^* |\psi_+\rangle \langle \psi_-| \langle E_-|E_+\rangle + \alpha^*\beta |\psi_-\rangle \langle \psi_+| \langle E_+|E_-\rangle. \end{aligned} \quad (3.3.3)$$

By taking the trace of the reduced density matrix with the position operator, we can find the probability density function of recording the particle's position as

$$\begin{aligned} p(x) &= \text{Tr}_S(\hat{\rho}_S \hat{x}) = \\ &= |\alpha|^2 |\psi_+(x)|^2 + |\beta|^2 |\psi_-(x)|^2 + 2 \text{Re}\{\alpha\beta^* \psi_+(x) \psi_-^*(x) \langle E_-|E_+\rangle\} \end{aligned} \quad (3.3.4)$$

where  $\psi_{\pm}(x) = \langle \hat{x} | \psi_{\pm} \rangle$ . The last term of Eq. (3.3.4) is the interaction term. As a result, the visibility of the interference pattern is governed by the term  $\langle E_-|E_+\rangle$ . In the case that the states  $|E_-\rangle$  and  $|E_+\rangle$  are total distinguishable, i.e.  $\langle E_-|E_+\rangle = 0$ , there will be not interference pattern observed [69].

### 3.3.1 Deriving a General Form for Decoherence

We showed in Sec. 3.1.1 that the time evolution of the density operator in a closed system is given by  $\partial_t \hat{\rho} = [\hat{H}, \hat{\rho}]/(i\hbar)$ . The natural next step is to find an equivalent

equation for a system that is in contact with its environment. We begin, following the argument in [70], by defining the total system at time  $t = 0$  as  $\hat{\rho}_{SE}(0)$  and its time evolution as  $\hat{\rho}_{SE}(t) = \hat{U}(t)\hat{\rho}_{SE}(0)\hat{U}^\dagger(t)$ , where  $\hat{U}(t) = \exp[-i\hat{H}t/\hbar]$  is the unitary time operator. We can then define the time evolution of the system as,

$$\begin{aligned} \frac{\partial \hat{\rho}_S(t)}{\partial t} &= \frac{d}{dt} \text{Tr}_E \left( \hat{U}(t)\hat{\rho}_{SE}(0)\hat{U}^\dagger(t) \right) \\ &= \frac{1}{i\hbar} \text{Tr}_E \left( [\hat{H}_{SE}, \hat{\rho}_{SE}] \right). \end{aligned} \quad (3.3.5)$$

This evolution equation is known as a generalised master equation and is specified by linear operators that take the density operator of the system, along with its time evolution until time  $t$ , and map it to the differential change at that time. Should the time-scale be large compared to the time-scale of the environmental correlation, we can use a generator, often referred to as the Liouville super-operator  $\mathcal{L}$ ,

$$\frac{\partial}{\partial t} \hat{\rho} = \mathcal{L} \hat{\rho} \quad (3.3.6)$$

to describe the time evolution of a density operator  $\hat{\rho}$ .

We introduce the dynamical map  $\mathcal{W}_t : \hat{\rho}_0 \mapsto \hat{\rho}_t$  which maps the state  $\hat{\rho}_0$  to a valid state at some later time  $t$ . This is given in the operator-sum representation as,

$$\mathcal{W}_t(\hat{\rho}) = \sum_{k=1}^N \hat{W}_k(t) \hat{\rho} \hat{W}_k^\dagger(t) \quad (3.3.7)$$

where  $N \leq d^2$  and  $d$  is the number of dimensions in the system. Eq. (3.3.7) is the formal solution to Eq. (3.3.6) under the condition that  $\mathcal{W}_t = e^{\mathcal{L}t}$  for all  $t > 0$ .

We introduce a set of operators  $E_j$ , where  $1 \leq j \leq d^2$  that satisfy,

$$\text{tr}(\hat{E}_i^\dagger \hat{E}_j) = \delta_{ij}. \quad (3.3.8)$$

This allows us to define the operator  $\hat{W}_k$  as,

$$\hat{W}_k = \sum_{j=1}^{d^2} \text{tr}(\hat{E}_j^\dagger \hat{W}_k) \hat{E}_j. \quad (3.3.9)$$

Letting the operator  $\hat{E}_{d^2}$  be proportional to the identity operator  $E_{d^2} = \mathbb{I}/\sqrt{d}$ ,

such that the other elements are traceless,

$$\text{tr}(\hat{E}_j) = \begin{cases} 0 & \text{for } j = 1, \dots, d^2 - 1 \\ \sqrt{d} & \text{for } j = d^2 \end{cases} \quad (3.3.10)$$

lets us rewrite the dynamical map Eq. (3.3.7) in terms of  $\hat{E}_j$  as,

$$\mathcal{W}_t(\hat{\rho}) = \sum_{i,j=1}^{d^2} c_{ij}(t) \hat{E}_i \hat{\rho} \hat{E}_j^\dagger \quad (3.3.11)$$

with the hermitian and positive coefficient matrix,

$$c_{ij}(t) = \sum_{k=1}^N \text{tr}(\hat{E}_i^\dagger \hat{W}_k(t)) \text{tr}(\hat{E}_j \hat{W}_k(t))^*. \quad (3.3.12)$$

By setting  $\mathcal{L}\hat{\rho} = \lim_{\tau \rightarrow 0} (\mathcal{W}_\tau(\hat{\rho}) - \hat{\rho})/\tau$ , and performing some lengthy algebra that is given fully in [70, Sec. 5.3.2], we find the first standard form of the generator as,

$$\mathcal{L}\hat{\rho}_S = \frac{1}{i\hbar} [\hat{H}, \hat{\rho}_S] + \sum_{i,j=1}^{d^2-1} \alpha_{ij} \left( \hat{E}_i \hat{\rho}_S \hat{E}_j^\dagger - \frac{1}{2} \hat{E}_j^\dagger \hat{E}_i \hat{\rho}_S - \frac{1}{2} \hat{\rho}_S \hat{E}_j^\dagger \hat{E}_i \right) \quad (3.3.13)$$

where the complex coefficients are given by,

$$\alpha_{ij} = \lim_{\tau \rightarrow 0} \frac{c_{ij}(\tau)}{\tau} \quad (3.3.14)$$

and have dimensions of frequency and make up the matrix  $\boldsymbol{\alpha}$ .

We find the Lindblad form of the generator  $\mathcal{L}$  by diagonalising  $\boldsymbol{\alpha}$ . In this case, the unitary matrix is given by,  $\mathbf{U}\boldsymbol{\alpha}\mathbf{U}^\dagger = \text{diag}(\gamma_1, \dots, \gamma_{d^2-1})$ . From this, we define the operator  $\hat{L}_k = \sum_{j=1}^{d^2-1} E_j U_{jk}^\dagger$ , and thus,

$$\mathcal{L}\hat{\rho}_S = \frac{1}{i\hbar} [\hat{H}, \hat{\rho}_S] + \sum_{k=1}^N \gamma_k \left( \hat{L}_k \hat{\rho}_S \hat{L}_k^\dagger - \frac{1}{2} \hat{L}_k^\dagger \hat{L}_k \hat{\rho}_S - \frac{1}{2} \hat{\rho}_S \hat{L}_k^\dagger \hat{L}_k \right) \quad (3.3.15)$$

where,  $N \leq d^2 - 1$ , and  $U_{jk}$  are the elements of the unitary matrix. The generator is specified by a single Hermitian operator  $\hat{H}$  that does not have to be the Hamiltonian of the system, and  $N$  Lindblad jump operators  $\hat{L}_k$  which describe transformations due to the environment (jumps) at rates  $\gamma_k$ .

As we are mostly interested in how the decoherence from the environment recovers classical behaviour from a quantum system, we can choose the Lindblad operator to be proportional to the Hamiltonian,  $\hat{L} = \sqrt{\gamma}\hat{H}$ . This gives the Lindblad equation of motion,

$$\frac{\partial}{\partial t}\hat{\rho}_S(t) = \frac{1}{i\hbar}[\hat{H}, \hat{\rho}_S(t)] + \gamma \left( \hat{H}\hat{\rho}_S(t)\hat{H} - \frac{1}{2}\hat{H}^2\hat{\rho}_S(t) - \frac{1}{2}\hat{\rho}_S(t)\hat{H}^2 \right). \quad (3.3.16)$$

### 3.4 The Quantum-to-Classical Transition

In classical mechanics we can describe the state of a system at some initial time  $t_0$  as a point in phase space  $(q, p)$  with zero uncertainty. We can then describe the system at some later time  $t$  as a new point in phase space determined by the Hamiltonian-Jacobi equation,

$$-\frac{\partial S}{\partial t} = H\left(q, \frac{\partial S}{\partial q}, t\right) \quad (3.4.1)$$

where  $S$  is called *Hamilton's Principal Function* and is the solution to the differential equation [71]. The zero uncertainty we have assumed in the initial state cannot carry over into discussions about quantum mechanics due to the Heisenberg uncertainty principle.

We can use an equivalent method to describe the dynamics of a system in the quantum regime using the Schrödinger equation,

$$i\hbar\frac{\partial\psi}{\partial t} = H\psi. \quad (3.4.2)$$

We consider a single particle of mass  $m$  moving in one dimension as this facilitates an easy comparison between the two approaches. In this case, we define the wave function in position representation to be  $\psi \equiv e^{iS/\hbar}$ . When we put this into Eq. (3.4.2) and expand the Hamiltonian, we find,

$$-\frac{\partial S}{\partial t} = \frac{1}{2m}\left(\frac{\partial S}{\partial q}\right)^2 + V(q) - \frac{i\hbar}{2m}\frac{\partial^2 S}{\partial q^2}. \quad (3.4.3)$$

In the limit  $S \gg \hbar$  and is real, the final term of Eq. (3.4.3) can be neglected. This recovers the classical Hamiltonian-Jacobi equation (3.4.1),

$$-\frac{\partial S}{\partial t} = \frac{1}{2m}\left(\frac{\partial S}{\partial q}\right)^2 + V(q). \quad (3.4.4)$$

This is a clear case of the quantum dynamics recovering the classical dynamics in the macroscopic regime. However, the Schrödinger equation is linear, that is, if both  $\psi_1$  and  $\psi_2$  are solutions to Eq. (3.4.2), then  $c_1\psi_1 + c_2\psi_2$  is also a solution, where  $c_1$  and  $c_2$  are complex coefficients, which is the source of superpositions observed in quantum mechanics. The same is not true of the Hamiltonian-Jacobi equation however. Eq. (3.4.1) is non linear, meaning that if  $S_1$  and  $S_2$  are solutions to Eq. (3.4.1), then  $a_1S_1 + a_2S_2$  is not necessarily also a solution. This means that superpositions are not allowed in classical mechanics as expected by observation.

We cannot use this non-linearity to explain the lack of observed macroscopic superpositions, because in this description, the classical dynamics are only an approximation to the quantum dynamics. No matter how small, the last term in Eq. (3.4.3), it is not always zero and can therefore be used to recover the Schrödinger equation and thus, superposition. This lack of observed macroscopic superpositions is the core of the “quantum measurement problem” [8].

### 3.4.1 The Measurement Problem

This measurement problem can be neatly explained by using the Von Neumann scheme for an ideal measurement process [72]. We consider the microscopic system  $S$  with some discrete and non-degenerate observable  $\mathcal{O}$  that has eigenvalues  $O_n$  and eigenvectors  $|O_n\rangle$ . We also have some measurement apparatus  $M$  that is used to measure the value of  $\mathcal{O}$ . At the start of the measurement, the apparatus is in its ready-state  $|M_0\rangle$ . After the measurement,  $M$  will be in the state  $|M_n\rangle$  which corresponds to different possible macroscopic configurations of  $M$ , such as different positions of a pointer on a scale. We take a moment here to note that there exist a number of measurement devices, such as semiconductor photon detectors, that are not traditionally macroscopic. However, the read-out, such as a pointer on a scale, is macroscopic. As a result there may be a number of steps between the measurement and macroscopic regime. We also assume that the interaction between the system  $S$  and apparatus  $M$  obeys the Schrödinger equation, as this should govern all natural processes, and is thus linear. We also assume that there is a perfect correlation between the initial state of the system



and the final state of the apparatus such that,

$$\text{Initial State: } |O_n\rangle \otimes |M_0\rangle \rightarrow \text{Final State: } |O_n\rangle \otimes |M_n\rangle. \quad (3.4.5)$$

From this we are able to say that if we observe  $M$  to be in the state  $|M_n\rangle$  the system is in the state  $|O_n\rangle$  and thus the observable  $\mathbf{O}$  has a value  $O_n$ .

The measurement problem arises when the system is prepared in a superposition of states, i.e.

$$|\psi\rangle = c_m |O_m\rangle + c_l |O_l\rangle \quad (3.4.6)$$

In this situation the linearity of the Schrödinger equation leads to the final state of the system  $S$  and apparatus  $M$  to be,

$$\begin{aligned} |\psi\rangle \otimes |M_0\rangle &= [c_m |O_m\rangle + c_l |O_l\rangle] \otimes |M_0\rangle \\ &\rightarrow c_m |O_m\rangle \otimes |M_m\rangle + c_l |O_l\rangle \otimes |M_l\rangle \end{aligned} \quad (3.4.7)$$

This final state is an entanglement between the micro-system  $S$  and the macro-apparatus  $M$ . Eq. (3.4.7) preserves the superposition in the microscopic state into the macroscopic measurement apparatus. But that is not what is observed. We do not measure macroscopic systems to be in a superposition, therefore  $M$  in the above *must* be in either the state  $|M_m\rangle$  or the state  $|M_l\rangle$ , but not both. Because the apparatus is entangled to the system, the system  $S$  into either the state  $|O_m\rangle$  or  $|O_l\rangle$  depending on which state of the detector is measured. This is the key result leading to the measurement problem.

By taking repeated measurements with the same initial conditions, we can observe the states  $|O_m\rangle$  and  $|O_l\rangle$  with relative probabilities  $|c_m|^2$  and  $|c_l|^2$ . This is the Born Probability Rule. The apparent emergence of these probabilities is another surprising outcome. Both the Schrödinger and Hamiltonian-Jacobi equations are deterministic for closed systems. Open systems in quantum mechanics are described by decoherence, where the coherence of the wave-function becomes tied up in the environment. Classical open systems are also in contact with their environments. Consider a pendulum that acts as a harmonic oscillator. If the pendulum is not in a vacuum, the air will act as the environment damping the pendulum's motion. At no point in the transition from quantum regime to the

classical do we encounter any probabilities. This is because the initial state in both cases is stated exactly. Probabilities in quantum mechanics are truly unique as classical probabilities arise as a result of uncertainty in our knowledge of the initial state [73].

Throughout this section we have defined a divide between a *quantum* system  $S$  and a *macroscopic* measurement apparatus  $M$ . However, we have not given a definition of where this divide takes place. This is another issue that remains unsolved, that is: where is the quantum-classical divide? There is no clear parameter (or set of parameters) about a system that defines it as either quantum or classical, nor is there any definition of the scale the parameter, e.g. how much mass a system must have or how many degrees of freedom lead to it being classical. Interferometry experiments have shown that spatial superposition hold masses of over 25,000u, or  $4.2 \times 10^{-23}$ kg [5]. On the other side of the scale, there is a clear lack of any quantum effect on macroscopic systems.

Any solution to the measurement problem must solve both, the lack of observed superpositions in the macroscopic regime and the emergence of probabilities that occur when a quantum system is driven into a specific outcome in agreement with the Born rule. Solutions should also aim to define the quantum-to-classical transition. This should be achieved by defining the parameter that leads to collapse and at what values we transition between the two theories. This chapter is dedicated to exploring proposed solutions to the measurement problem. Special focus will be given to objective collapse models where we will also discuss some tests of these models.

## 3.5 Proposed Solutions to the Measurement Problem

There are a number of proposed solutions to the measurement problem. In this section we introduce some of these possible solutions and discuss their merits and faults. This leads us into the next chapter where we begin by introducing the idea that quantum and classical dynamics are both approximations to a theory of universal dynamics.

### 3.5.1 The Copenhagen Interpretation

One of the most commonly used solution to the measurement problem, and perhaps the one most taught to students, is the Copenhagen interpretation proposed by Bohr in 1928 [6]. This postulate aims to solve the apparent contradiction between classical and quantum physics by applying an arbitrary divide between the quantum and classical worlds. It suggests that microscopic systems are governed by the rules of quantum mechanics (i.e. superpositions are allowed) and that macroscopic systems are governed by classical mechanics (i.e. superpositions are repressed). It also suggests that during the measurement process a quantum system interacts with a classical system causing the wave function to ‘collapse’ forcing the superposition of eigenstates of the observable into just one in a way governed by the Born rule. The major issues with this interpretation is that it fails to determine the scale the transition from a quantum system to a classical one occurs and what parameter of the system drives this change, i.e. is it the system mass, or the physical dimensions, or even something else that cause the transition. The Copenhagen interpretation also fails to give any mechanism to govern the transition or the ‘collapse’ of the wave function.

On the surface, this seems like a sensible model to use. We can make accurate predictions about the outcome of measurements on both quantum and classical systems without issue. However, we still don’t know how to treat mesoscopic systems between these two regimes, or if there is a hard border, where it is. Although the Copenhagen interpretation can be useful for making predictions about quantum systems, it does not give us much, if any, insight into the quantum-to-classical transition.

### 3.5.2 Decoherence as a Solution

The effect of decoherence is observed in laboratory experiments and describes the role that the environment plays during the act of measurement. For the purposes of our argument, it is sufficient to define the environment as the set of particles in the radius  $R = cT$  where  $c$  is the speed of light and  $T$  the time during which the measurement takes place. This gives us all the particles that could causally interact with the experiment.

Let us consider a simple two-state quantum system to demonstrate the effect of decoherence as done by Adler in [74]. Take a quantum system, such as atomic spin, with an initial state vector,

$$|\psi_0\rangle = \alpha |A\rangle + \beta |B\rangle \quad (3.5.1)$$

where  $|\alpha|^2 + |\beta|^2 = 1$ . We then probe the system with an apparatus that has initial state vector  $|M_0\rangle$  which in turn interacts with the environment with initial state vector  $|E_0\rangle$ . This means the total initial state vector is,

$$|\Phi_0\rangle = |\psi_0\rangle |M_0\rangle |E_0\rangle. \quad (3.5.2)$$

We then allow the state  $|\Phi_0\rangle$  to evolve in time according to the deterministic unitary evolution giving the state at time  $t$  to be  $|\Phi_t\rangle = U |\Phi_0\rangle$ , where  $U = \exp(-iHt)$ . We can set up our experiment in such a way to ensure that the initial state evolves into the form,

$$|\Phi_t\rangle = \alpha |A\rangle |\phi_t^{(A)}\rangle + \beta |B\rangle |\phi_t^{(B)}\rangle \quad (3.5.3)$$

where the states  $|\phi_t^{(A)}\rangle$  and  $|\phi_t^{(B)}\rangle$  are the entangled states of the apparatus and environment. After time  $T$  these two states are macroscopically distinguishable. The effect of decoherence is to rapidly decay the inner product,

$$\langle \phi_t^{(A)} | \phi_t^{(B)} \rangle \quad (3.5.4)$$

from 1 at  $t = 0$  to 0 by  $t = T$ . The consequence of this is that the interference between the states  $|A\rangle$  and  $|B\rangle$  rapidly disappears as time evolves reducing the state to a statistical mixture of states with relative weights  $|\alpha|^2$  and  $|\beta|^2$ . This is not enough to explain the collapse of the wave function during a measurement. The time evolution of the state from Eq. (3.5.2) to Eq. (3.5.3) still obeys the linearity of the Schrödinger equation. We also see that the coherence is not lost, but is transferred to the environment as shown in Eqs. (3.3.3) and (3.3.4) where the only terms that include interference contain the environmental state. The use of decoherence also fails to explain the breakdown of superposition for isolated systems, such as the universe as a whole.

### 3.5.3 The Many-Worlds Interpretation

The many-worlds interpretation devised by Everett [7] proposes the idea that there is no real breakdown of the superposition. According to this theory, the linear evolution of the Schrödinger equation holds at all scales, including during the measurement process. This removes the need for any collapse into a single state. However, an observer will still only record a single outcome after a measurement. During a measurement in the many-worlds interpretation, the state of the system and measurement apparatus evolves as it does in Eq. (3.4.7) where  $|M_m\rangle$  is the state of the apparatus if it detects the system in the state  $|O_m\rangle$  and  $|M_l\rangle$  is the state of the apparatus if it detects the system in the state  $|O_l\rangle$ . In the many-worlds interpretation, the two parts of this equation exist simultaneously in different ‘branches’ of the universe, as if they existed in different worlds.

On the surface, this may seem like a sensible solution to the measurement problem. There is no real collapse of the wave function, only an apparent one. Observers can only see one branch of the universe causing this apparent collapse. It also removes the issue of on what scale does the Schrödinger equation breakdown by commenting that it is *always* valid. However, this interpretation does not provide an explanation on the origins of probabilities from the Born rule. Everett’s theory suggests that deterministic evolution always holds. So how do seemingly non-deterministic probabilities arise from this theory? Another criticism is the lack of falsifiability of the theory. There is no experiment that can be done to rule out the existence of these ‘other branches’ as all predictions in standard quantum mechanics agrees with the predictions of the many-worlds interpretation.

# Chapter 4

## Collapse Models

In this chapter we cover the so called quantum-to-classical transition and the measurement problem along with briefly discussing some proposed solutions to this apparent flaw in quantum theory. In the last chapter, we discussed a handful of proposed solutions that do not modify the framework of quantum mechanics.

We note that the Schrödinger picture is not the only model describing quantum mechanics. For example, quantum field theory (QFT) was derived out of the need for a relativistic quantum mechanics and strongly agrees with experimental evidence. However, QFT is still a linear process allowing superpositions and could be thought of as a first-order approximation [75]. This chapter introduces modifications to the formulation of quantum theory acting as a unified dynamics that will simplify to either quantum mechanics or classical mechanics on the relevant scales. We focus primarily on non-relativistic collapse models which allow for an instantaneous collapse of the wave function. There have been some attempts at applying collapse models to relativistic quantum theories [76,77]. However, these models have not shown much success.

### 4.1 Quantum Mechanics as an Approximation

This work discusses another possible solution to the measurement problem. That is, quantum and classical theory are approximations to a more general theory. As a result, the lack of superpositions in the macroscopic regime are attributed

to applying quantum theory to a regime where it is not valid. We also describe the collapse as a physical and dynamical process occurring during the interaction between the quantum system and the measurement apparatus. Any theory that encapsulates the full ‘universal dynamics’ must contain the following properties:

1. The universal dynamics must be non-linear to allow the breakdown of the superposition that occurs during measurement
2. This non-linearity must be sufficiently small in the microscopic regime to be negligible, thus recovering the linear superpositions experimentally verified on the microscopic scale
3. As we progress from the micro to the macro scale, the new dynamics must allow for non-unitary, norm-preserving evolution required to cause all but one of the possible outcomes to decay exponentially
4. The dynamics must be stochastic, such that the result of a measurement is random and cannot be predicted, however, the results of multiple measurements must obey the Born rule

Any universal dynamics will be defined by a set of parameters that take values such that on the microscopic scale, the theory is indistinguishable from quantum mechanics. The theory must also contain an amplification mechanism such that for macroscopic scales, these parameters force the theory to be indistinguishable from classical mechanics. This creates a mesoscopic region where the dynamics are distinct from both quantum and classical mechanics, and are therefore experientially distinguishable [8].

Non-linear modifications to quantum theory have been explored for many years. One of the reasons for this is not to solve the measurement problem (although they can, and often do, provide the solutions we are looking for), but instead because many of the differential equations that describe physical phenomena are non-linear. Proponents of these non-linear modifications ask why the Schrödinger equation, which seems to be the most fundamental of these equations, should be an exception. There are two branches of modifications, deterministic and stochastic non-linear equations.

### 4.1.1 Deterministic Non-Linear Modifications

There exist a small number of proposed deterministic non-linear Schrödinger equations. In this section we introduce two of these theories as a brief introduction, but it should be noted that other deterministic non-linear theories have been proposed. The first is the logarithmic Schrödinger equation from Bialynicki-Birula [78],

$$i\hbar \frac{\partial}{\partial t} \psi(\mathbf{x}, t) = \left[ -\frac{\hbar^2}{2m} \nabla^2 + V(\mathbf{x}, t) - b \ln(|\psi(\mathbf{x}, t)|^2 a^n) \right] \psi(\mathbf{x}, t) \quad (4.1.1)$$

where  $a$  is an arbitrary real and positive constant with dimensions of length,  $n$  is the dimensionality of the configuration space, and  $b$  is a real universal constant with an upper limit of  $4 \times 10^{-10}$  eV.

By following Weinberg [79], we find a non-linear equation for wave functions of discrete variables, which we call  $k$ , as,

$$i \frac{d\psi_k}{dt} = \frac{\partial h(\psi_k, \psi_k^*)}{\partial \psi_k^*} \quad (4.1.2)$$

where  $h$  is a real function satisfying the requirement that for any complex  $\lambda$ ,

$$h(\lambda\psi_k, \psi_k^*) = h(\psi_k, \lambda\psi_k^*) = \lambda h(\psi_k, \psi_k^*) \quad (4.1.3)$$

thus ensuring that if  $\psi_k$  is a solution of Eq. (4.1.2), then  $\lambda\psi_k$  is also a solution. By considering the two component ( $k = 1, 2$ )  ${}^9\text{Be}^+$  ion without a time-varying external field, Weinberg derived the following equation for the function  $h$ ,

$$h = n\bar{h}(a) \quad (4.1.4)$$

where  $n = |\psi_1|^2 + |\psi_2|^2$  is the norm and  $\bar{h}(a) = 2\epsilon a^2$  is a real function of the variable  $a = |\psi_2|^2/n$  and the term  $\epsilon$  which has units of energy and is bounded by the relation  $|\epsilon| < 10^{-15}$  eV.

There remains two major issues with these modifications. That is, deterministic non-linear modification can result in superluminal communication in direct violation of special relativity. This results from the density matrices of two initially equivalent statistical mixtures becoming inequivalent after evolution due to the non-linearity. Different, but equivalent mixtures can be prepared at a



distance. For example, we can define two equivalent mixtures such that one density matrix can be used to describe both,  $\rho = \sum_i A_i |\psi_i\rangle \langle \psi_i| = \sum_i B_i |\phi_i\rangle \langle \phi_i|$ . If we assume that mixtures of  $\{|\psi_i\rangle\}$  and  $\{|\phi_i\rangle\}$  are particles travelling to one observer from a distant point, and that they are entangled to two other mixtures  $\{|\alpha_i\rangle\}$  and  $\{|\beta_i\rangle\}$  travelling from the same point to another observer in the opposite direction. When the first observer measures either of the ensembles, the collapse drives the observed ensemble for the second observer into one of the defined ensembles. Because these ensembles are equivalent, the density matrix, and all expectation values, are the same. However, should there be some deterministic non-linearity, over time the density matrices of the two ensembles travelling to the second observer will become inequivalent. As a result, appropriate measurements will allow the second observer to determine which ensemble they have, and thus which ensemble the first observer measured [75, 80]. Another issue is the fact that stochasticity seems to be necessary to explain the origins of the probabilities that occur during measurement. For these reasons, investigations around non-linear modifications tend to focus on stochastic modifications.

### 4.1.2 Stochastic Non-Linear Modifications

One of the more well known of these stochastic non-linear modifications is given by Pearle [81]. In this system we replace the Schrödinger equation with a non-linear equation during measurement.

Before the measurement, the combined micro-system and measurement apparatus exists in an ensemble of state vectors  $|\chi_k\rangle$  each cosponsoring to a possible state of the system which all have equal probability of being true. Immediately after the interaction the state vector of the system takes on the form

$$|\chi_k\rangle = \sum_n x_n^{1/2} \exp[i\theta_n] |\phi_n\rangle \quad (4.1.5)$$

where the amplitude terms  $x_n$  are the same for all  $|\chi_k\rangle$  but the phase terms  $\theta_n$  are different. After the interaction, the non-linear Schrödinger equation will drive all the amplitudes  $x_n$  to 0 except one that is driven to 1 dependent on the phase terms of the true  $|\chi_k\rangle$ . A different starting  $|\chi_k\rangle$  can lead to different final

states  $|\phi_n\rangle$ . This is why we obtain different results as a consequence of repeated measurements.

By assigning the probability distribution of the phases over the parameter space, the Born rule is recovered. This probability must be put in by hand, and should be chosen to recover the probability rule we want to emerge. This is a fundamental limit of this phenomenological model. There should be a fundamental reason for the probability distribution to be the way it is, not simply to recover the Born rule.

## 4.2 Spontaneous Collapse Models

There exists a specific class of modifications to quantum mechanics known as Spontaneous Collapse Models. They form a dynamical reduction to the wave-function by inducing spontaneous collapses of the wave-function all the time. These ‘measurement-like’ collapse events occur for all particles regardless of whether or not they are interacting with the environment, and regardless if they are single atom systems, or a more complex system, like a macroscopic measurement device.

In order for a given collapse model to be an effective description of reality, it must contain a few key properties [8].

- **Non-linearity:** The modifications must break the linearity of the Schrödinger equation for macroscopic systems to ensure their localisation.
- **Stochastic:** Measurements of quantum systems lead to stochastic outcomes distributed according to the Born rule. Any modification to standard quantum theory must maintain this stochasticity. This is also necessary to prevent the non-linear terms from leading to super-luminal communication.
- **No super-luminal signalling:** In order to preserve the causal nature of space-time, and maintain agreement with special relativity, any modification must not allow for faster than light communication.
- **Amplification:** Any modification must not prevent the formation of superpositions on the quantum scale, but must localise macroscopic systems. In

order to account for this, there must be a mechanism that amplifies the rate of the collapse events as the system size increases such that macroscopic superpositions are suppressed, but quantum superpositions are able to last for sufficiently long time scales.

From here we cover a few examples of collapse models discussing their formalisation and how this leads to a collapse.

### 4.2.1 A Simple Example, The QMUPL Model

We begin by discussing a simplified example of a collapse model known as the Quantum Mechanics with Universal Position Localisation (QMUPL) model as described in [82]. In one dimension, the universal dynamics is represented by a stochastic differential equation,

$$d\psi_t = \left[ -\frac{i}{\hbar} \hat{H} dt + \sqrt{\lambda} (\hat{x} - \langle \hat{x} \rangle_t) dW_t - \frac{\lambda}{2} (\hat{x} - \langle \hat{x} \rangle_t)^2 dt \right] \psi_t \quad (4.2.1)$$

where  $\hat{x}$  is the position operator,  $\langle \hat{x} \rangle_t$  is the expectation value of the position at time  $t$ , and  $W_t$  is a standard Wiener process describing the noise field as a random walk of the amplitudes of each definite state driving the collapse mechanism. We also define the collapse constant,

$$\lambda = \frac{m}{m_0} \lambda_0 \quad (4.2.2)$$

as proportional to the mass of the particle  $m$ . Here,  $m_0$  is the mass of one nucleon, and  $\lambda_0$  measures the collapse strength.

For a single Gaussian state of a free particle, the wave function is described by,

$$\psi_t(x) = \exp \left[ -a_t (x - \bar{x}_t)^2 + i \bar{k}_t x + \gamma_t \right] \quad (4.2.3)$$

where the functions  $a_t$  and  $\gamma_t$  are complex functions of time, and the mean position and mean momentum  $\bar{x}_t$  and  $\bar{k}_t$  are real valued functions of time. For this single Gaussian case, the function of  $\gamma_t$  can be omitted as a normalisation factor. The

remaining equations are then found by solving,

$$da_t = \left[ \lambda - \frac{2i\hbar}{m}(a_t)^2 \right] dt \quad (4.2.4)$$

$$d\bar{x}_t = \frac{\hbar}{m}\bar{k}_t dt + \frac{\sqrt{\lambda}}{2\operatorname{Re}[a_t]}dW_t \quad (4.2.5)$$

$$d\bar{k}_t = -\sqrt{\lambda}\frac{\operatorname{Im}[a_t]}{\operatorname{Re}[a_t]}dW_t. \quad (4.2.6)$$

By noting that the spread in momentum and position of the Gaussian wave function is

$$\sigma_q(t) = \sqrt{\langle q^2 \rangle - \langle q \rangle^2} = \frac{1}{2}\sqrt{\frac{1}{\operatorname{Re}[a_t]}} \quad (4.2.7)$$

$$\sigma_p(t) = \sqrt{\langle p^2 \rangle - \langle p \rangle^2} = \hbar\sqrt{\frac{\operatorname{Re}[a_t]^2 + \operatorname{Im}[a_t]^2}{\operatorname{Re}[a_t]}} \quad (4.2.8)$$

and then by solving Eq. (4.2.4) we find the spreads in position and momentum are given by,

$$\sigma_x(t) = \sqrt{\frac{\hbar}{m\omega} \frac{\cosh(\omega t + \varphi_1) + \cos(\omega t + \varphi_2)}{\sinh(\omega t + \varphi_1) + \sin(\omega t + \varphi_2)}} \quad (4.2.9)$$

$$\sigma_p(t) = \sqrt{\frac{\hbar m\omega}{2} \frac{\cosh(\omega t + \varphi_1) - \cos(\omega t + \varphi_2)}{\sinh(\omega t + \varphi_1) + \sin(\omega t + \varphi_2)}} \quad (4.2.10)$$

where

$$\omega = 2\sqrt{\frac{\hbar\lambda_0}{m_0}} \quad (4.2.11)$$

and the functions  $\varphi_i$  are functions of the initial conditions. These spreads do not increase indefinitely, but reach asymptotic values,

$$\sigma_x(\infty) = \sqrt{\frac{\hbar}{m\omega}} \quad (4.2.12)$$

$$\sigma_p(\infty) = \sqrt{\frac{\hbar m\omega}{2}} \quad (4.2.13)$$

such that  $\sigma_x(\infty)\sigma_p(\infty) = \hbar/\sqrt{2}$ , close to the Heisenberg limit. This results from the standard Hamiltonian causing the wave function to spread, while the

reduction terms try to localise the wave function. These two features compete against each other until an equilibrium is reached.

In the case that we have a superposition of two positional Gaussian states, our wave function is described by,

$$\begin{aligned}\psi_t(x) &= \psi_{1t}(x) + \psi_{2t}(x) \\ &= \exp[-a_{1t}(x - \bar{x}_{1t})^2 + i\bar{k}_{1t}x + \gamma_{1t}] \\ &\quad + \exp[-a_{2t}(x - \bar{x}_{2t})^2 + i\bar{k}_{2t}x + \gamma_{2t}]\end{aligned}\tag{4.2.14}$$

If we define the distance between the two pointer states in position and momentum space as  $X_t = \bar{x}_t^+ - \bar{x}_t^-$  and  $K_t = \bar{k}_t^+ + \bar{k}_t^-$ , we can use them in a set of linear deterministic differential equations,

$$\frac{d}{dt} \begin{pmatrix} X_t \\ K_t \end{pmatrix} = \begin{pmatrix} -A_1(t) & \hbar/m \\ -A_2(t) & 0 \end{pmatrix} \cdot \begin{pmatrix} X_t \\ K_t \end{pmatrix}\tag{4.2.15}$$

where in the limit of  $t \rightarrow \infty$ , the  $2 \times 2$  matrix  $A(t)$  becomes

$$A(\infty) = \begin{pmatrix} -\omega & \hbar/m \\ -2\lambda & 0 \end{pmatrix}.\tag{4.2.16}$$

From this we can determine that the distances  $X_t$  and  $K_t$  tend to 0. That is, the Gaussian wave functions converge towards each other.

The collapse occurs as a result of the measure of one of the states  $\psi_{1,2}(x)$  becoming rapidly small compared to the other such that one component effectively vanishes. We can define the relative damping of the components as,

$$\Gamma_t = \text{Re}[\gamma_{1t}] - \text{Re}[\gamma_{2t}]\tag{4.2.17}$$

which satisfies the stochastic differential equation,

$$d\Gamma_t = \lambda X_t^2 \tanh(\Gamma_t) dt + \sqrt{\lambda} X_t dW_t\tag{4.2.18}$$

that can be solved under the initial condition  $\Gamma_0$ . From here we can derive the

probability that the state will finish in either of the states  $\psi_1$  or  $\psi_2$  to be,

$$\begin{aligned} P_1 &\approx \frac{1}{2}[1 + \tanh \Gamma_0] \\ &= \frac{|\psi_{1,0}|^2}{|\psi_{1,0}|^2 + |\psi_{2,0}|^2} \end{aligned} \quad (4.2.19)$$

$$\begin{aligned} P_2 &\approx \frac{1}{2}[1 - \tanh \Gamma_0] \\ &= \frac{|\psi_{2,0}|^2}{|\psi_{1,0}|^2 + |\psi_{2,0}|^2} \end{aligned} \quad (4.2.20)$$

which recovers the Born rule.

## 4.2.2 GRW Model

Formulated in 1986 by Ghirardi, Rimini, and Weber [83], the GRW theory attempts to present a unified dynamical description that simplifies to standard quantum mechanics for sufficiently small systems while maintaining a classical descriptions of large objects. It introduces a localisation process that occurs at random times. The probability of such an event taking place in the time interval  $dt$  is  $\lambda_{GRW}dt$ . This provides a modification to the usual von Neumann equation Eq. (3.1.21) for a single particle,

$$\frac{\partial}{\partial t} \hat{\rho}(t) = -\frac{i}{\hbar} [\hat{H}, \hat{\rho}(t)] - \lambda_{GRW} (\hat{\rho}(t) - T[\hat{\rho}(t)]) \quad (4.2.21)$$

where the function  $T[\hat{\rho}(t)]$  describes the localisation process driving pure states into statistical mixtures matching the Born rule. In coordinate representation, the second term in Eq. (4.2.21) is,

$$\lambda_{GRW} \langle \hat{x} | (\hat{\rho} - T[\hat{\rho}]) | \hat{y} \rangle = \lambda_{GRW} \left( 1 - \exp \left[ -\frac{\alpha(x-y)^2}{4} \right] \right) \langle \hat{x} | \hat{\rho} | \hat{y} \rangle \quad (4.2.22)$$

where  $\lambda_{GRW}$  is the rate at which the localisation events occur, and  $1/\sqrt{\alpha}$  is the localisation distance.

It can often be advantageous to separate the centre of mass motion of the composite system and the individual quantum particles that make them up. In order to achieve this, we can assume that the localisation process, described by  $T[\hat{\rho}(t)]$  occurs individually for each particle in the system. Considering a system

of  $N$  particles that are each affected by the localisation process with a frequency  $\lambda_{GRW}^{(i)}$ , we can modify Eq. (4.2.21) to be,

$$\frac{\partial}{\partial t}\hat{\rho}(t) = -\frac{i}{\hbar}[\hat{H}, \hat{\rho}(t)] - \sum_{i=1}^N \lambda_{GRW}^{(i)} (\hat{\rho}(t) - T^{(i)}[\hat{\rho}(t)]). \quad (4.2.23)$$

By separating out the center of mass and internal motion Hamiltonians,  $\hat{H}_x$  and  $\hat{H}_r$ , respectively, we find Eq. (4.2.23) becomes,

$$\frac{\partial}{\partial t}\hat{\rho}(t) = -\frac{i}{\hbar} \left( [\hat{H}_x, \hat{\rho}(t)] + [\hat{H}_r, \hat{\rho}(t)] \right) - \sum_{i=1}^N \lambda_{GRW}^{(i)} (\hat{\rho}(t) - T^{(i)}[\hat{\rho}(t)]) \quad (4.2.24)$$

where  $T^{(i)}[\dots]$  contains contribution from the center of mass motion and the relative motion of the constituent particles. By taking the trace of this over the internal motion, we recover exactly Eq. (4.2.21) with  $\lambda_{GRW} = \sum_{i=1}^N \lambda_{GRW}^{(i)}$ . This gives us the amplification mechanism we need. As the system increases in size, the rate of collapse increases.

### 4.2.3 Diósi-Penrose Model

In 1987 Diósi produced a stochastic modification to quantum mechanics based on gravity induced collapse [84]. By introducing a gravity dependant white-noise term, the Von Neumann master equation is modified to be,

$$\partial_t \hat{\rho}_t = -\frac{i}{\hbar}[\hat{H}, \hat{\rho}_t] - \frac{G}{2\hbar} \iint [\hat{f}(\mathbf{r}), [\hat{f}(\mathbf{r}'), \hat{\rho}_t]] \frac{d^3 r d^3 r'}{|\mathbf{r} - \mathbf{r}'|} \quad (4.2.25)$$

where  $G$  is the usual Newtonian gravitational constant, and  $\hat{f}(\mathbf{r})$  is the mass density operator of the system. From here, we can introduce the characteristic damping time,

$$[\tau_d(x, x')]^{-1} = \frac{G}{2\hbar} \iint [f(\mathbf{r}|x) - f(\mathbf{r}'|x')]^2 \frac{d^3 r d^3 r'}{|\mathbf{r} - \mathbf{r}'|} \quad (4.2.26)$$

where the mass density at the point  $\mathbf{r}$  is given by  $f(\mathbf{r}|x)$ . As the distance between the positions  $x$  and  $x'$  decrease, the damping time increases, tending to  $\tau_d = \infty$  when the positions coincide, i.e. when  $x = x'$ .

A similar model of gravitational collapse was independently conceived of by Penrose [85, 86]. In this formulation, Penrose considers a superposition of the states  $|\alpha\rangle$  and  $|\beta\rangle$ . These states both have the energy  $E$ ,

$$i\frac{\partial|\alpha\rangle}{\partial t} = E|\alpha\rangle \qquad i\frac{\partial|\beta\rangle}{\partial t} = E|\beta\rangle. \quad (4.2.27)$$

In a standard quantum superposition, i.e. ignoring gravity, where  $|\psi\rangle = a|\alpha\rangle + b|\beta\rangle$ , the total state will also have the same energy

$$i\frac{\partial|\psi\rangle}{\partial t} = E|\psi\rangle. \quad (4.2.28)$$

By introducing the effect of gravity the differential operator  $\partial/\partial t$  corresponds to the action of a Killing vector representing the time displacement of stationarity for each state. In this case, the Killing vector refers to a vector field that moves the Schwarzschild metric by an amount  $dt$  but does not change the metric.

In general, the Killing vector for each state is different. However, the Schrödinger equation applies to each state and the superposition of the states. This is at odds with the general relativity view point. Penrose thus suggests taking an approximate point-wise identification between the two space-times arising from the two states. This leads to an energy uncertainty in the superposition  $E_G$  which is considered a fundamental aspect of the superposition. From the Heisenberg uncertainty principle, we find that  $\hbar/E_G$  is the rate at which the superposition decays, equivalent to Diósi's  $\tau_d$ .

#### 4.2.4 Continuous Spontaneous Localisation

The Continuous Spontaneous Localisation (CSL) model, originally described in [87], is the most advanced and well studied collapse model. For this reason, it will be the focus of our simulations, although in principle our simulations are general enough to work for any collapse model that can be described as manifesting as a decoherence term.

In the mass proportional form derived by Pearle and Squires [88] we have a



differential equation similar to the form of Eq. (4.2.1),

$$\frac{d}{dt} |\psi\rangle_t = \left[ -\frac{i}{\hbar} \hat{H} dt + \frac{\sqrt{\gamma}}{m_0} \int [M(\mathbf{x}) - \langle M(\mathbf{X}) \rangle_t] dW_t(\mathbf{x}) d\mathbf{x} - \frac{\gamma}{2m_0^2} \int [M(\mathbf{x}) - \langle M(\mathbf{x}) \rangle_t]^2 dt d\mathbf{x} \right] |\psi\rangle_t. \quad (4.2.29)$$

Here we have used the standard Hamiltonian  $\hat{H}$ , a reference mass  $m_0$  often chosen to be the mass of one nucleon, the coupling constant  $\gamma$  that sets the strength of the decoherence term, and an ensemble of Wiener processes for each point in space  $W_t(\mathbf{x})$ . We have also used the smeared mass density operator,

$$M(\mathbf{X}) = \sum_j m_j N_j(\mathbf{x}) \quad (4.2.30)$$

$$N_j(\mathbf{x}) = \int g(\mathbf{y} - \mathbf{x}) \alpha_j^\dagger(\mathbf{y}) \alpha_j(\mathbf{y}) d\mathbf{y} \quad (4.2.31)$$

where  $\alpha_j^\dagger(\mathbf{y})$  and  $\alpha_j(\mathbf{y})$  are the creation and annihilation operators for particle of type  $j$  at the position  $\mathbf{y}$ . The smearing function is given by,

$$g(\mathbf{x}) = \frac{\exp[-\mathbf{x}^2/2r_c^2]}{\sqrt{2\pi}r_c} \quad (4.2.32)$$

where  $r_c = 1/\sqrt{\alpha}$  is the localisation distance.

The collapse is governed by the density number operators  $\alpha_j^\dagger(\mathbf{y})\alpha_j(\mathbf{y})$  which means that superposition of different numbers of particles in different locations are suppressed. This is the second-quantised version of collapsing the wave-function. Second quantised collapse models are formulated in the language of quantum field theory and allow us to work with systems of indistinguishable particles. In position representation, the suppression of the off diagonal elements of the matrix is given by,

$$\frac{d}{dt} \langle \mathbf{x}' | \rho_t | \mathbf{x}'' \rangle = -\Gamma(\mathbf{x}', \mathbf{x}'') \langle \mathbf{x}' | \rho_t | \mathbf{x}'' \rangle \quad (4.2.33)$$

with decay function,

$$\Gamma(\mathbf{x}', \mathbf{x}'') = \frac{\gamma}{2} \sum_{i,j=1}^N [G(\mathbf{x}'_i - \mathbf{x}'_j) + G(\mathbf{x}''_i - \mathbf{x}''_j) - 2G(\mathbf{x}'_i - \mathbf{x}''_j)] \quad (4.2.34)$$

where the  $N$  is the number of nucleons in the system, an approximation allowed because the effect of electrons are negligible in comparison to that of nucleons. We also have the function,

$$G(\mathbf{x}) = \frac{\exp[-\mathbf{x}^2/4r_c^2]}{(4\pi r_c^2)^{3/2}}. \quad (4.2.35)$$

We find that for a single nucleon, Eq. (4.2.34) reduces to,

$$\Gamma(\mathbf{x}', \mathbf{x}'') = \frac{\gamma}{(4\pi r_c^2)^{3/2}} \left( 1 - \exp \left[ -\frac{|\mathbf{x}' - \mathbf{x}''|^2}{4r_c^2} \right] \right) \quad (4.2.36)$$

which is equivalent to the one particle GRW collapse term in Eq. (4.2.22) [8].

# Chapter 5

## Interferometric Tests of Collapse Models

The values of the constants of the collapse models discussed in the previous chapter, such as the rate and length scale  $\lambda_c$  and  $r_c$  in CSL, must be determined experimentally. A matter wave interferometer is an effective tool to probe the superposition of massive objects which we can use to put bounds on the values of the model parameters. Similar interferometry techniques have often been used to test the wave nature of various phenomena, from Thomas Young proving the wave nature of light [89], to the verification of the de Broglie wavelength using scattered electrons [90]. The work in this chapter primarily follows the discussion given in [91]. However, we begin by briefly discussing non-interferometric tests of CSL. We then introduce the theory of the Talbot interferometer and extend this into the Mie regime. Section 5.4.3 provides new contributions including the polarisation of scattered light in the scattering decoherence in the grating.

### 5.1 Non-Interferometric Tests of Collapse Models

Non-interferometric tests measure the collapse noise of a system. This is a modification that results in Brownian motion in addition to the standard quantum dynamics. Various non-interferometric experiments aim to detect this Brownian

motion and use this to inform the bound of collapse models. This results in exclusion plots of the type given in Fig. 5.1.

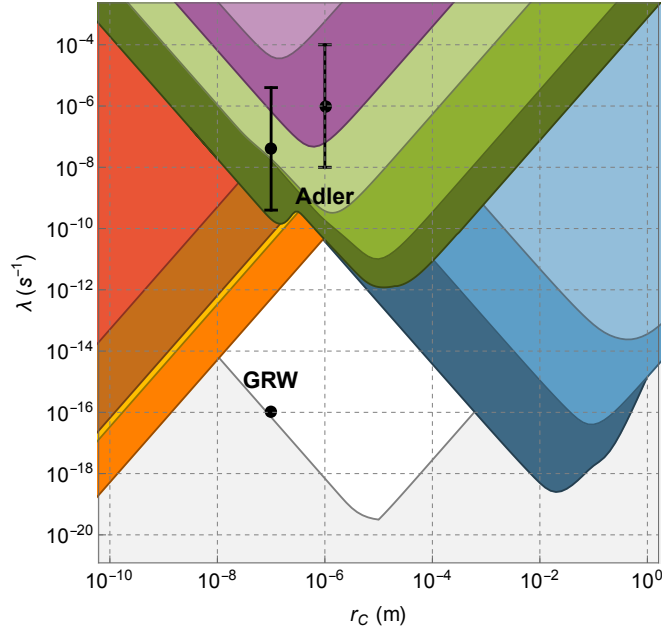


Figure 5.1: A plot of the CSL parameter space showing regions excluded by various non-interferometric experiments reproduced from [9]. The shaded exclusion regions are discussed in the main text. The shaded grey region is the theoretical lower bound for the CSL parameters. It ensures that macroscopic systems are localised sufficiently quickly. These bounds are chosen to ensure that a  $10\mu\text{m}$  radius graphine disk collapses in 0.01s, ensuring that the smallest object the human eye can realise is localised within the time resolution of the eye.

The Yellow region of Fig. 5.1 is found by measuring the increase in internal energy of a system due to the collapse noise. CSL predicts an energy gain rate of

$$\frac{dE}{dt} = \frac{3}{4} \frac{\lambda_c \hbar^2 m}{r_c^2 m_0^2} \quad (5.1.1)$$

where  $m_0$  is the mass of a nucleon and  $m$  is the total mass of the particle. By dividing by the mass we find the energy gain rate per unit mass. Low temperature experiments are able to reduce their heating rates to  $10^{-10}\text{W/kg}$  with a residual heating from unknown sources at  $10^{-11}\text{W/kg}$ . This corresponds to a maximum value of  $\lambda_c = 3.1 \times 10^{-11}\text{Hz}$  at  $r_c = 10^{-7}\text{m}$  [92].

We find the bounds in red in Fig. 5.1 by considering the diffusion in position of a cloud of cold atoms [9, 93]. CSL predicts an increase to the heating rate of particles given by Eq. (5.1.1) which manifests in a cloud of cold atoms as an increase to the spread of the cloud equal to

$$\langle \hat{\mathbf{x}}^2 \rangle_t = \langle \hat{\mathbf{x}}^2 \rangle_t^{\text{QM}} + \frac{\lambda_c \hbar^2}{2r_c^2 m_0^2} t^3. \quad (5.1.2)$$

where  $\langle \hat{\mathbf{x}}^2 \rangle_t^{\text{QM}}$  is the expansion predicted by standard quantum mechanics. Experiments are able to cool clouds of  $^{87}\text{Rb}$  atoms down to the temperatures in the pK range [94]. By measuring the standard deviation of the gas cloud after it has been allowed to expand for a short time and comparing this data to Eq. (5.1.2) with various values of  $\lambda_c$  and  $r_c$  we find an upper bound to  $\lambda_c$  of  $5.1 \times 10^{-8} \text{Hz}$  for  $r_c = 10^{-7} \text{m}$ .

We can also infer the collapse noise from anomalous noise in optomechanical systems. We can describe the noise spectrum of a mechanical resonator observed by a light field as

$$S_{\text{DNS}}(\omega) = S_{\text{OPTO}}(\omega) + S_{\text{ENV}}(\omega) + S_{\text{CM}} \quad (5.1.3)$$

where  $S_{\text{OPTO}}(\omega)$  is the standard optomechanical contribution,  $S_{\text{ENV}}(\omega)$  is the contribution from environmental sources, and  $S_{\text{CM}}$  is the residual noise from the collapse model. There are three main classes of systems that can be used to test collapse models. First are the cantilever experiments, shown in green in Fig. 5.1, where the motion of a ferromagnetic sphere attached to a silicon cantilever is observed. The second are various gravitational wave detectors shown in blue in Fig. 5.1. The final type are levitated systems, where the motion of a levitated sphere is observed, shown in purple in Fig. 5.1 [9].

The Brownian motion induced by the collapse noise accelerates particles causing them to radiate if they are charged [95]. The rate of emission of photons with energy  $E$  is found from

$$\frac{d\Gamma}{dE} = N_{\text{atoms}}(N_A^2 + N_A) \frac{\lambda_c \hbar e^2}{4\pi^2 \epsilon_0 m_0^2 r_c^2 c^3 E} \quad (5.1.4)$$

where  $N_{\text{atoms}}$  is the number of atoms of atomic number  $N_A$ .

The heating effects of cosmological bodies, such as Neutron stars and Neptune, can also be used to estimate the bounds on collapse models [96]. Assuming that the thermal emission of radiation, described by the Stefan-Boltzmann law is balanced by the heading from CSL, we find an estimate of the collapse rate given by,

$$\lambda_c = \frac{16R^2 m_0^2 \pi r_c^2 T^4 \sigma}{3m\hbar^2} \quad (5.1.5)$$

where  $T$  is the black-body temperature,  $\sigma$  is Stefan's constant equal to  $5.6 \times 10^{-8} \text{W m}^{-2} \text{K}^{-4}$ ,  $R$  is the radius of the body, and  $m$  is its mass.

The tests of collapse models, that are discussed above, are useful tools for imposing bounds on potential collapse models. However, for a more direct bound, we must directly probe the superposition of macroscopic scale objects. The remainder of this chapter introduces a Talbot style interferometer with a phase grating created by a standing wave laser beam. We build the theory of a Talbot interferometer using a single, optically trapped and cooled particle, as a coherent source. Then we extend this theory beyond the point-like approximation to allow spherical particles in the Mie regime and apply the effects of known decoherence sources and CSL to the final interference pattern. Our theory is used to produce simulations that can be analysed via a Bayesian approach in the next chapter to inform later experiments.

## 5.2 Talbot-Lau Interferometry

In 1836, Talbot observed a self-imaging effect of periodic structures in near-field diffraction [97]. That is, the image of the grating will be repeated at regular intervals of length, called the Talbot Length  $L_T = d^2/\lambda$ , where  $d$  is the grating period and  $\lambda$  is the incident wavelength. This self-image is off-set by half a period when the distance is an odd integer multiple of  $L_T$  and reproduces exactly for even multiples of  $L_T$  [98] and is shown in Fig. 5.2.

A Talbot interferometer can be simply described by a periodic grating a distance  $L_1$  from a point source and a screen a distance of  $L_2$  after the grating. In the paraxial approximation, this grating introduces a set of wave vectors each separated by the diffraction angle  $\lambda/d$ . In the near-field, these diffraction orders

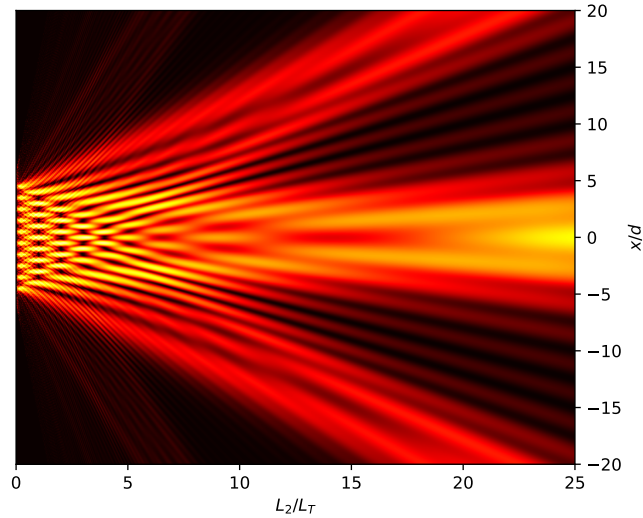


Figure 5.2: The interference pattern from a periodic grating with 10 slits. Near the grating on the left, we see the near-field Talbot effect and the characteristic self-imaging feature. This image is reproduced from the supplementary of [99].

overlap and are able to interfere with each other. A grating that extends infinitely in the  $x$  direction can be described by an amplitude transmission function,

$$t(x_2) = \sum_{j=-\infty}^{\infty} b_j \exp \left[ 2\pi i j \frac{x_2}{d} \right] \quad (5.2.1)$$

where  $x_2$  is the position on the grating. We have used the eikonal approximation which treats scattering problems as differential equations, in this scenario it allows us to find the transmission functions by integrating over straight lines. A Fresnel-Kirchoff integral then gives the intensity of the pattern at some point  $x_3$  on the screen,

$$I_T(x_1, x_3) \propto \left| \int t_2(x_2) \exp \left[ \frac{2\pi}{\lambda} i(l_1 + l_2) \right] dx_2 \right|^2 \quad (5.2.2)$$

where  $l_1 = \sqrt{L_1^2 + (x_2 - x_1)^2}$  and  $l_2 = \sqrt{L_2^2 + (x_3 - x_2)^2}$  are the distances traversed by the light ray originating at  $x_1$ , passing through the grating at  $x_2$ , and arriving on the screen at  $x_3$ .

A Talbot-Lau set up, as shown in Fig. 5.3, works by replacing the point source and screen by gratings with periods  $d_1$  and  $d_2$  respectively. The first grating is

illuminated by an uncollimated particle beam and acts as a spatially incoherent source with an intensity given by,

$$|t_1(x_1)|^2 = \sum_{l=-\infty}^{\infty} a_l \exp \left[ 2\pi i l \frac{x_1}{d_1} \right] \quad (5.2.3)$$

where the coefficients  $a_l$  ensures symmetry for the components around  $l = 0$  and that the  $l = 0$  component is equal to 1 thus, the imaginary parts of each coefficient cancel out for  $\pm l$ . The detector captures particles from a wide area and thus has poor spatial resolution. To account for this, the third grating is moved through a distance  $x_{3s}$  to produce a periodic detection function determined by the flux transmission function,

$$|t_3(x_3 - x_{3s})|^2 = \sum_{n=-\infty}^{\infty} c_n \exp \left[ 2\pi i n \frac{x_3 - x_{3s}}{d_3} \right]. \quad (5.2.4)$$

The final detection pattern is then a function of the translation of the third grating [100],

$$S_{TL}(x_{3s}) \propto \int |t_3(x_3 - x_{3s})|^2 I_{TL}(x_3) dx_3 \quad (5.2.5)$$

where

$$I_{TL}(x_3) \propto \int |t_1(x_1)|^2 I_T(x_1, x_3) dx_1. \quad (5.2.6)$$

Such a set-up can be applied to  $C_{70}$  fullerene molecules [10]. This experiment was performed with free-standing gratings made of gold. As the particle gets larger, the distance between its surface and the walls of the grating decrease. This leads to a deviation in the potential from the eikonal approximation and more realistic results using the full Casimir-Polder potential [101, 102]. Particles passing through the grating are then likely to suffer attractive forces when they get too close to the walls leading to many of them being removed from the beam. The grating then risks becoming clogged with particles from the beam further deviating from the given theory. The result of this is that the interferometer can only work with very specific de Broglie wavelengths for the particle beam [103].

### 5.2.1 Laser Gratings

A viable solution to this is to replace the second material grating with a retro-reflected coherent laser beam creating a standing wave polarised in the  $x$  direction



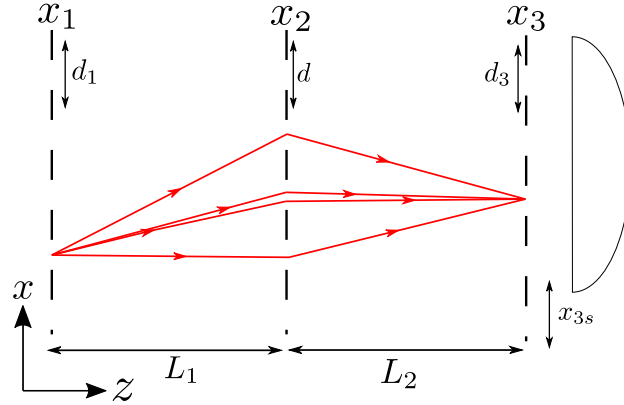


Figure 5.3: A Talbot-Lau interferometer set up. A coherent sum of all paths (four are shown) from each point  $x_1$  to  $x_3$  gives the interference effect. The grating  $x_3$  can move to create a position dependant signal on the detector.

with a function  $\mathbf{E} = 2E_0 \sin(kz) \cos(\omega t)\hat{\mathbf{x}}$ . This creates a periodic variation in the electric field amplitude that couples to the particle's polarisability. The resulting shift in energy leads to a periodic phase shift in the matter-wave beam. In the Fourier transform picture, this manifests as the particles acquiring integer multiples of the grating momentum  $p_d = 2h/\lambda_G$  to the transverse motion of the particle beam. The different diffraction orders are then able to interfere with each other leading to a measurable interference pattern after some free-evolution [104].

In a laser grating, the coherent phase shift effect is governed by the integral over the electric field potential. The position dependant phase shift is then given by [11, 105],

$$\phi(z) = \frac{1}{\hbar} \int V(z, t) dt = \phi_0 \cos^2 kz \quad (5.2.7)$$

where  $V(z, t) = \mathbf{P} \cdot \mathbf{E}$  and  $\mathbf{P} = \alpha \mathbf{E}$  is the polarisation of the particle due to the electric field and  $k = 2\pi/\lambda_G$  is the wave-number of the grating laser.

Using a laser as a grating introduces the complexity that we must consider the possibility of grating photons being either absorbed or scattered from the particle. If we consider the absorbed photons and define the photon absorption rate as,

$$\Gamma_{\text{abs}}(z, t) = \frac{\sigma_{\text{abs}}}{h\nu} |\mathbf{E}(z, t)|^2 \quad (5.2.8)$$

where  $\sigma_{\text{abs}}$  is the absorption cross section, we find the position dependant number of absorbed photons to be,

$$n_{\text{abs}}(z) = \int \Gamma_{\text{abs}}(z, t) dt = n_0^{\text{abs}} \cos^2(kz). \quad (5.2.9)$$

The equivalent equations for scattering are,

$$\Gamma_{\text{sca}}(z, t) = \frac{\sigma_{\text{sca}}}{h\nu} |\mathbf{E}(z, t)|^2 \quad (5.2.10)$$

$$n_{\text{sca}}(z) = \int \Gamma_{\text{sca}}(z, t) dt = n_0^{\text{sca}} \cos^2(kz) \quad (5.2.11)$$

where  $\sigma_{\text{sca}}$  is the scattering cross section [11, 104].

### 5.3 A Single Source Talbot Interferometer

Most Talbot interferometers use a Talbot-Lau set-up. This uses three gratings. The first creates coherence in the particle beam. The second creates a phase shift generating the diffraction pattern. And the final grating is shifted to measure the particle transmission as a function of this shift. However, by using a single particle prepared with sufficient coherence, and with large enough spatial separations to be detectable by optical means, allows us to do away with the first and third grating. The interferometer, as shown in Fig. 5.4, discussed here uses the derivation found in the supplementary of [11] to inform the derivation of the interference pattern that will be observed from the single source Talbot interferometer. In order to reach the masses necessary to constrain the parameters of collapse models, we must run the experiment for long times. To achieve this we will need to isolate the system from the environment very well, and have a long drop for the particle to fall. Both of these issues are solved by performing the experiment in space, such as in the proposed MAQRO mission [106]. This allows us to reach low environmental temperatures and low pressures to minimise the effects of decoherence. The low gravity means that we do not have to build impractically large drop towers to reach the necessary free-fall times to witness interference of matter-waves of large scale objects.

There are a number of possible ways to load the particle into the optical trap. The most simple way is to suspend the particles in an ethanol solution

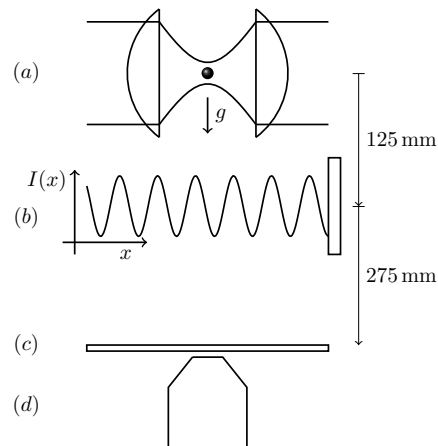


Figure 5.4: Diagram of the proposed interferometer from [11]. (a) a particle is trapped and cooled to 20mK in a harmonic potential then released. (b) the particle passes a phase grating provided by a retro-reflected standing wave laser. (c) after another free-fall the particle arrives on a glass slide where (d) a microscope records its position.

and, using commercially available medical nebulisers, spray the particles into the trap [107]. This is an effective technique in earth based systems. The particles can be sprayed into the vacuum chamber, and when one is caught, the chamber is sealed and pumped down. Methods like this have the issue of needing to work in normal air pressures, they also introduce droplets of the suspension liquid in the chamber potentially adding to the background residual gas. To load the particle in vacuum, which is the more likely case for space based missions such as MAQRO, we have two options. The first is to use a laser-induced desorption technique. The particles are initially attached to a substrate above the trap. A pulsed laser is then focused to the back of the substrate inducing acoustic shock-waves that eject particles from the substrate [108]. This has been shown to work at pressures as low as 1mbar. Alternately, it is possible to use a piezoelectric transducer for particle loading in vacuum [109]. In this method, a glass substrate containing the particles to be trapped is clamped to a piezoelectric ring that is driven at the resonant frequency of the glass. This shaking releases nano particles that can be trapped. Piezo launching has been widely used to trap particles ranging from 170nm to  $3\mu\text{m}$  in diameter [110–112] as well as clumps of particles [113]. It

has been demonstrated that this method works in vacuum down to pressures of 0.6mbar. Due to the lower pressures that it works in, the piezoelectric method of particle loading is perhaps the most efficient method to be used.

Using one of the techniques discussed in section 2.3, we are able to cool the centre of mass motion of a massive particle to a state sufficiently cool enough to provide us with the necessary coherence. After interaction with the laser grating, the particle's location can be measured in a number of different ways. One possibility is to deposit the particle onto a glass slide and determine its arrival location via a microscope [11]. We can also use interferometric means of detecting the particle's position after the interferometer. When the particle is illuminated by the same laser used for the initial trapping and cooling, it will scatter light that interacts with the coherent laser light. The intensity of the measured light will vary with the position of the particle which can be used to estimate the particle's position [114]. More recent proposals for measuring the position of the particle include a self-interference method [115]. In this method the particle is located between a detector and a mirror. The light scattered from the particle passes through one of two lenses. The image created by one lens is reflected back. This reflected image interferes with the directly scattered light and the other lens focuses both fields on a detector. The phase of the interference, and thus the measured intensity, is a function of the distance between the particle and the mirror. By simply holding the mirror stationary, the interferometric signal is a function of the particle's position. To maximise the re-usability of the particle, thus ensuring the same mass between runs, it would be most advantageous to use an interferometric method of position detection.

This process can be repeated  $N$  times, with identically fabricated particles or even by reusing the same particle, to build up the interference pattern. This pattern can then be compared to the pattern we would expect from a more classical treatment to determine how 'quantum' the particle behaves. Alternately, we can use a Bayesian treatment, which will be discussed in full in Chapter 6, of the measured arrival locations to gain more information from each data point, and to provide an objective measure as to how sure we are that we can rule out a given classicalisation model.

### 5.3.1 MAQRO Experiment

We envision a space-based platform on which these experiments would be performed. Our simulations primarily use the conditions that would be present in the proposed MAQRO experiment as described in [114]. This is a proposed medium-sized space-based experiment first submitted in response to the 2010 ‘M3’ call of the ESA as a part of the Cosmic Vision program. In this section we introduce the MAQRO experiment and the conditions that our simulations will use.

The time scale for a given experiment is based on the Talbot time  $t_T = md^2/h$  and so scales with the mass and grating period squared. In order to add any new information to the bounds on a collapse model, we must use sufficiently massive particles. Increasing the mass of the test particle necessitates a longer free-fall time in order to create a clear interference pattern. For this reason it may be more convenient to perform these experiments in space, where the particle remains effectively at rest with respect to the apparatus. We also potentially have the benefit of not having to pump down the apparatus to a low pressure to decrease the effect of collisional decoherence, although the concept of having the platform exposed to space remain a point of discussion. The experimental parameters we have assumed for a ‘MAQRO-like’ experiment are given in Table 5.1.

The values chosen for the center of mass and internal temperatures are realistic experimental values that have been reached in laboratory settings for particles of similar sizes to the ones we are considering [51, 116]. We are able to achieve the center of mass temperature via feedback cooling as described in section 2.3.2. Although ground state cooling has been achieved [19, 54], this remains a potential challenge for a MAQRO-like experiment. In our simulations, we do not reach the ground state of motion for the particle, this thermal state will still provides a sufficiently coherent source for our experiments. This also prevents excessive internal heating reducing the amount of black-body thermal emission, see section 5.5.2.

The environmental temperature of 20K is given in [114] as the maximum temperature to minimise decoherence from black-body absorption of photons. Although the temperature of space is approximately ten times lower than this value, we note that the spacecraft on which the experiment is situated will emit some amount of heat, so the value of 20K is a realistic value to choose here.

Symbol	Name	Value
$\rho$	Si particle density	$2329\text{kg m}^{-3}$
$\lambda_G$	Grating laser wavelength	$2d = 354\text{nm}$
$\nu$	Trapping frequency	$200\text{kHz}$
$T_{\text{com}}$	Initial center of mass temperature	$20\text{mK}$
$T_{\text{int}}$	Initial internal temperature	$25\text{K}$
$T_{\text{env}}$	Environmental temperature	$20\text{K}$
$P_g$	Residual gas pressure	$10^{-13}\text{Pa}$
$t_1$	First free-fall time	$2t_T$
$\phi_0$	Phase parameter	Chosen based on particle mass
$t_2$	Second free-fall time	Chosen based on particle mass
$\sigma_z$	Gaussian Position Width	$\sqrt{k_B T / (4\pi^2 m \nu_m^2)}$
$\sigma_m$	Measurement Position Uncertainty	$\sigma_z + (10\text{nm}/100\text{s})t$

Table 5.1: Control parameters used in the MAQRO-like scenario. The values of the free-fall time  $t_2$ , and phase parameter  $\phi_0$  are the control parameters and are varied for each new experimental set-up, such as changing the particle mass.

### 5.3.2 Initial State

In the first stage of the experiment, a dielectric nano-particle is trapped in and optical trap. The centre of mass motion of this particle is cooled to  $T_{CM}$ . We only need to cool motion of the particle in the z-axis as we only consider the motion of the particle in this direction. This assumption requires that the x and y motion of the particle are separable from the z motion throughout the experiment, and that the grating interaction does not depend on the x and y coordinates. This can be achieved by aligning the grating laser to the z axis and using a sufficiently wide spot area such that the particle is uniformly illuminated by the grating laser over the duration of the laser pulse.

The optical trap that cools the particle can be described by a harmonic oscillator model as discussed in section 2.2.1. Therefore, when the particle is released from the trap, it will have a motional state that can be modelled by a thermal harmonic oscillator [66],

$$\begin{aligned} \langle x | \hat{\rho} | x' \rangle &= \psi(x)\psi^*(x) = \sqrt{\frac{m\nu_M}{\hbar\pi}} \tanh\left(\frac{\hbar\nu_M}{2k_B T_{CM}}\right) \\ &\times \exp\left[-\frac{m\nu_M}{4\hbar} \tanh\left(\frac{\hbar\nu_M}{2k_B T_{CM}}\right) (x+x')^2 - \frac{m\nu_M}{4\hbar} \coth\left(\frac{\hbar\nu_M}{2k_B T_{CM}}\right) (x-x')^2\right]. \end{aligned} \quad (5.3.1)$$

By inserting Eq. (5.3.1) into Eq. (3.2.2) and setting  $x = z + s/2$  and  $x' = z - s/2$ , we can describe this state by the following Gaussian Wigner function of its one dimensional motion,

$$w_0(z, p) = \frac{1}{2\pi\sigma_z\sigma_p} \exp\left(-\frac{z^2}{2\sigma_z^2} - \frac{p^2}{2\sigma_p^2}\right) \quad (5.3.2)$$

where where the standard deviations of the position and momentum are,

$$\sigma_z = \sqrt{\frac{\hbar}{4\pi m\nu_M} \coth\left(\frac{\hbar\nu_M}{2k_B T_{CM}}\right)} \quad (5.3.3a)$$

$$\sigma_p = \sqrt{\pi\hbar m\nu_M \coth\left(\frac{\hbar\nu_M}{2k_B T_{CM}}\right)} \quad (5.3.3b)$$

and  $\nu_M$  is the trap frequency [66]. For the realistic values considered here such that  $\hbar\nu_M \ll k_B T_{CM}$  and  $\coth x \approx 1/x$  giving the form of  $\sigma_z$  given in Table 5.1,

the Wigner function given in Eq. (5.3.2) appears the same as a classical thermal phase-space distribution in a harmonic oscillator. All of the diffraction effects and all relevant decoherence mechanisms can be contained within this phase-space description. However, it is more convenient to use a characteristic function representation which is defined as the Fourier transform of the Wigner function,

$$\chi(s, q) = \int w(z, p) e^{i(qz - ps)/\hbar} dz dp. \quad (5.3.4)$$

As the particle is released from the optical trap its characteristic function reads,

$$\chi_0 = \exp\left(-\frac{\sigma_z^2 q^2 + \sigma_p^2 s^2}{2\hbar^2}\right). \quad (5.3.5)$$

We find that for realistic experimental values, the width of the particle's momentum spread is much larger than the momentum unit of the grating laser  $P_d = h/d$ , for the values  $\nu_M = 200\text{kHz}$  and  $T_{CM} = 20\text{mK}$  on a grating with  $2d = 355\text{nm}$ , we find that  $\sigma_p/P_d \approx 10^4$ . As a result the initial state of the particle extends over many grating periods. If we only look at the centre of the interference pattern we can make the approximation that the distribution is flat, we are therefore justified in using the expression,

$$\chi_0(s, q) \approx \frac{\sqrt{2\pi}\hbar}{\sigma_p} \exp\left(-\frac{\sigma_z^2 q^2}{2\hbar^2}\right) \delta(s) \quad (5.3.6)$$

where  $\delta(s)$  is the Dirac delta function and approximates the Gaussian as arbitrarily narrow, which greatly simplifies our equations [11].

### 5.3.3 Propagation

While the particle is in free-fall, that is between the trap, grating pulse, and position detection, the matter-wave of the particle will be allowed to evolve freely. In an ideal system, we could represent this free evolution for a time  $t$  as a sheering transformation in phase space of the form  $\chi_t(s, q) = \chi_0(s - rt/m, q)$ . However, for a realistic description of the interferometer, we must consider the effects of any external accelerations and all sources of decoherence.

The presence of an acceleration leads to the Hamiltonian,

$$\hat{H}(t) = \frac{\hat{P}^2}{2m} + ma(t)z \quad (5.3.7)$$



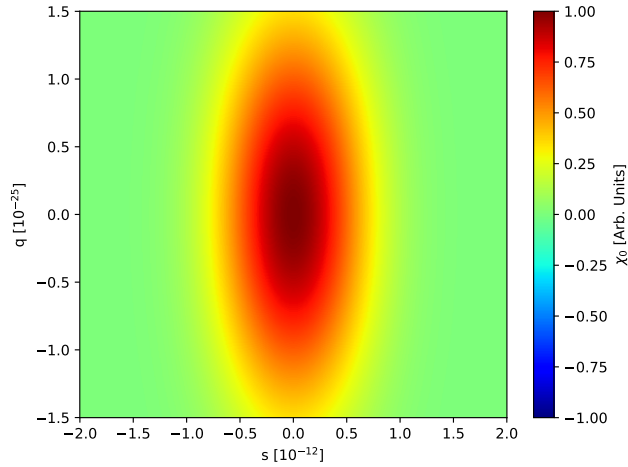


Figure 5.5: The characteristic function Eq. (5.3.5) as the particle is released from the trap

for motion in the  $z$  axis, where  $a(t)$  is the time dependant acceleration. We must also consider any decoherence effects that take place during the particle's free-evolution. We describe the evolution of the particle's state in the presence of decoherence by the equation,

$$\partial_t \rho = -i[\hat{H}(t), \rho] + \mathcal{L}(t)\rho \quad (5.3.8)$$

where the first term is the pure quantum evolution and the second term includes the effects of decoherence. Each source of decoherence that we consider will add an extra time dependant Lindblad supperoperator  $\mathcal{L}(t)$  which, in position representation, takes the form,

$$\langle z | \mathcal{L}\rho | z' \rangle = \Gamma(t)[g(z - z') - 1] \langle z | \rho | z' \rangle \quad (5.3.9)$$

which describes random jump events  $\langle z | \rho | z' \rangle \rightarrow g(z - z') \langle z | \rho | z' \rangle$  taking place with rate  $\Gamma(t)$  which may or may not have a time dependence. The spatial resolution function of the decoherence is normalised such that  $g(0) = 1$ . Super positions with a width  $z - z'$  for which  $g \approx 0$  decohere with the full rate  $\Gamma(t)$ .

In our phase-space picture, the decoherence effect is represented by a momentum averaging transformation. This transforms the characteristic function

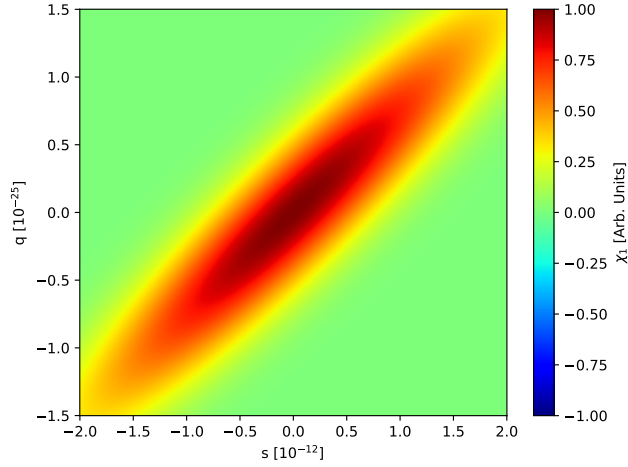


Figure 5.6: The characteristic function Eq. (5.3.10) after the matter-wave has evolved for  $t_1 = 2 \times 10^6$ s. We have ignored the effects of decoherence in this plot.

as,

$$\chi_t(s, q) = \chi_0 \left( s - \frac{qt}{m}, q \right) \exp \left( \frac{i}{\hbar} [q\Delta z(t) - \Delta p(t)s] + \int_0^t d\tau \Gamma(\tau) \left[ g \left( s - \frac{q\tau}{m} \right) - 1 \right] \right) \quad (5.3.10)$$

where the momentum and position shifts are given by,

$$\Delta p(t) = m \int_0^t a(t') dt' \quad (5.3.11a)$$

$$\Delta z(t) = \int_0^t \Delta p(t') / m dt'. \quad (5.3.11b)$$

### 5.3.4 Grating Transformation and Interference Effect

After a free-evolution time  $t_1$  the particle is illuminated by a pulsed retro-reflected laser to create a standing wave. This standing wave provides a modulation  $\phi(z)$  to the phase of the particle's matter-wave which leads to an interference after the grating. In position space, this position dependant phase shift has the effect

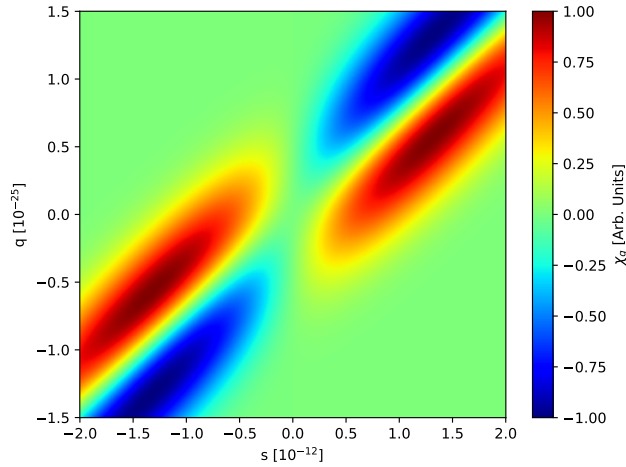


Figure 5.7: The characteristic function Eq. (5.3.13) after the particle has evolved for a time  $t_1 = 2 \times 10^6$ s and interacted with the standing wave laser grating. We have assumed the point-like approximation given in Sec. 5.4.1.

of multiplying the wave function by  $\exp[i\phi(z)]$  [104]. Because the characteristic function is a Fourier transform, we are able to make use of the convolution theorem that states [117, Eq. 9],

$$\mathcal{F}[a \times b] = \{\mathcal{F}[a] * \mathcal{F}[b]\} \quad (5.3.12)$$

The effect of the grating on the characteristic function is thus a convolution expressed in terms of Talbot coefficients  $B_n(\xi)$ ,

$$\chi_G(s, q) \rightarrow \sum_n \tilde{B}_n\left(\frac{s}{d}\right) \chi_t\left(s, q + n\frac{h}{d}\right) \quad (5.3.13)$$

where  $d = \lambda_G/2$  is the grating period determined by the wave length of the grating laser  $\lambda_G$ . The Talbot coefficients contain all the coherent and decoherent effects of the laser grating. A full treatment, in both the Rayleigh and Mie regimes, is given in section 5.4.

After the grating pulse, the particle is allowed to freely evolve again for a time  $t_2$ . This is achieved in the characteristic function by applying the transformation in Eq. (5.3.10) to Eq. (5.3.13). This results in the characteristic function where

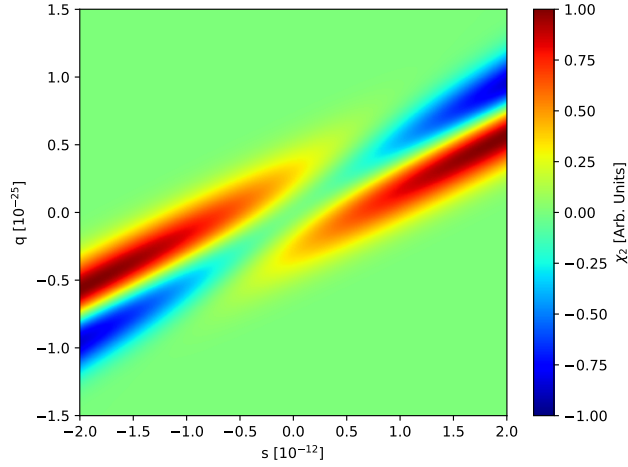


Figure 5.8: The characteristic function Eq. (5.3.14) after the particle has evolved for times  $t_1 = t_2 = 2 \times 10^6$ s and passed through the phase grating. We have ignored all sources of decoherence in this graph for simplicity.

the particle's position is measured becoming,

$$\begin{aligned}
 \chi_{t_2}(s, q) = & \sum_n \tilde{B}_n \left( \frac{s}{d} - \frac{qt_2}{md} \right) \\
 & \exp \left\{ \frac{i}{\hbar} [q\Delta z(t_2) - \Delta p(t_2)s] + \int_0^{t_2} \Gamma(t_1 + \tau) \left[ g \left( s - \frac{q\tau}{m} \right) - 1 \right] d\tau \right\} \\
 & \times \exp \left\{ \frac{i}{\hbar} \left[ \left( q + n \frac{h}{d} \right) \Delta z(t_1) - \Delta p(t_1) \left( s - \frac{qt_2}{m} \right) \right] + \right. \\
 & \quad \left. \int_0^{t_1} \Gamma(\tau) \left[ g \left( s - q \frac{t_2 + \tau}{m} - n \frac{h\tau}{md} \right) - 1 \right] d\tau \right\} \\
 & \times \chi_0 \left( s - q \frac{t_1 + t_2}{m} - n \frac{ht_1}{md}, q + n \frac{h}{d} \right) \quad (5.3.14)
 \end{aligned}$$

We recover the density distribution of the final state of the particle, i.e. the interference pattern, by projecting the position from the density matrix. This has the same effect as computing the marginal distribution from the Wigner function (see Eq. (3.2.4)). To find this from our characteristic function, we perform the inverse Fourier transform over  $q$  holding  $s = 0$  which retains the effect of the  $\delta(s)$

in Eq. (5.3.6),

$$\begin{aligned}
 w(z) &= \langle z | \rho | z \rangle = \frac{1}{2\pi\hbar} \int \chi_{t_2}(0, q) \exp \left[ -i \frac{qz}{\hbar} \right] dq \\
 &= \frac{m}{\sqrt{2\pi}\sigma_p(t_1 + t_2)} \sum_n \exp \left[ \frac{2\pi i n}{\mu d} (z - \delta z) \right] \tilde{B}_n \left( \frac{nt_2}{\mu t_T} \right) \exp \left\{ -\frac{1}{2} \left[ \frac{2\pi n \sigma_z t_2}{d(t_1 + t_2)} \right]^2 \right\} \\
 &\quad \times \exp \left\{ \int_0^{t_2} \Gamma(t_1 + \tau) \left[ g \left( \frac{nh\tau}{\mu m d} \right) - 1 \right] d\tau + \int_0^{t_1} \Gamma(\tau) \left[ g \left( \frac{nh t_2 t_1 - \tau}{\mu m d t_1} \right) - 1 \right] d\tau \right\}
 \end{aligned} \tag{5.3.15}$$

where the Talbot time  $t_T = md^2/h$  appears as a natural time scale for the experiment. The resultant function is a periodic fringe pattern oscillating at the geometrically magnified grating period  $D = \mu d$ , where  $\mu = (t_1 + t_2)/t_1$ . We also have a shift in the fringe pattern that occurs in the presence of a time-dependant homogeneous acceleration  $a(t)$  given by,

$$\delta z = \Delta z(t_1 + t_2) - \mu \Delta z(t_1) = \int_0^{t_1+t_2} \int_0^t a(\tau) d\tau dt - \mu \int_0^{t_1} \int_0^t a(\tau) d\tau dt. \tag{5.3.16}$$

However, we do not consider any accelerating being present in experiments, so this is set to  $\delta z = 0$ . The final interference pattern can be further simplified by using Euler's formula  $e^{i\theta} = \cos \theta + i \sin \theta$  and by noticing that the Fourier components are symmetrical about  $n = 0$  and are identically equal to 1 when  $n = 0$  as discussed for Eq. (5.2.3). By also recalling that  $\sin(-\theta) = -\sin(\theta)$  we can also remove the imaginary components, which will sum to 0. Finally, we make the substitution

$$R_n = \exp \left\{ \int_0^{t_2} \Gamma(t_1 + \tau) \left[ g \left( \frac{nh\tau}{\mu m d} \right) - 1 \right] d\tau + \int_0^{t_1} \Gamma(\tau) \left[ g \left( \frac{nh t_2 t_1 - \tau}{\mu m d t_1} \right) - 1 \right] d\tau \right\}. \tag{5.3.17}$$

This leave the final interference pattern as

$$w(z) = \frac{m}{A} \left[ 1 + 2 \sum_{n=0}^{\infty} R_n \tilde{B}_n \left( \frac{ndt_2}{t_T D} \right) e^{-2 \left( \frac{n\pi\sigma_z t_2}{D t_1} \right)^2} \cos \left( \frac{2\pi n z}{D} \right) \right] \tag{5.3.18}$$

where  $A = \sqrt{2\pi}\sigma_p(t_1 + t_2)$ .

## 5.4 Derivation of the Talbot Coefficients

In this section we derive the Talbot coefficients discussed in section 5.3.4. We start by deriving the Talbot coefficients in the Rayleigh limit following the argument given in the supplementary of [11]. Next we introduce the concepts of Mie theory and apply this to extend the Talbot coefficients to particle in the Mie regime. This application to Mie theory was first done in [105], however, we build upon this work by considering the polarisation of the scattered light to provide a more accurate description of the decoherence in the grating.

The electric field of the grating couples to the polarizability of the particle and induces a phase shift given by  $\phi(z)$ . The effect of the grating is expressed in terms of Talbot coefficients as described in Eq. (5.3.13). The coherent effects of the grating are given by,

$$B_n(\xi) = J_n(\phi_0 \sin \pi \xi) \quad (5.4.1)$$

where  $J_n(x)$  is the Bessel function of the first kind, and  $\phi_0$  is the amplitude of the phase shift. The phase shift is found by integrating the optical potential the particle feels over the pulse duration as done in Eq. (5.2.7).

### 5.4.1 Talbot Coefficients in the Rayleigh Regime

For a point-like dipole, the real part of the particle's polarizability determines the optical potential in the presence of the standing wave electric field  $\mathbf{E}(z, t)$ . Under the assumption that the laser spot area is much larger than the size of the particle, such that the laser can be approximated as a plane-wave during the duration of the laser pulse, and that the laser propagates in the  $z$  direction, the potential is given by [11, 104],

$$V(z, t) = -\frac{1}{4} \text{Re}[\alpha(\omega)] |\mathbf{E}(z, t)|^2. \quad (5.4.2)$$

where  $\alpha(\omega)$  is the frequency dependant polarisability [118],

$$\alpha(\omega) = 4\pi\epsilon_0 R^3 \frac{\epsilon(\omega) - 1}{\epsilon(\omega) + 2}. \quad (5.4.3)$$

Combining Eqs (5.2.7) and (5.4.2), we find the magnitude of the phase shift as,

$$\phi_0 = \frac{2 \operatorname{Re}[\alpha(\omega)] E_G}{\hbar c \epsilon_0 a_G} \quad (5.4.4)$$

where the pulse energy is  $E_G = \int P_G(t) dt$ , the integral of the laser power over the pulse duration, and the area of the laser is  $a_G$ . The quantity  $E_G/a_G$  is the fluence and determines the amount of energy that passes through a unit area. Our assumption that the laser's waist is much wider than the radius of the particle means the fluence is constant across the particle.

We must also consider a number of incoherent effects taking place whilst the particle is illuminated by the grating laser to fully describe the effect on the matter wave. Whilst in the grating, the particle will absorb photons from the beam which will transfer momentum to the particle in units of photon momentum  $P_d$ . The stochastic absorption process is governed by the master equation [119],

$$\mathcal{L}_{\text{abs}} \rho = \gamma_{\text{abs}} \left[ \cos\left(\frac{\pi x}{d}\right) \rho \cos\left(\frac{\pi x}{d}\right) - \frac{1}{2} \left\{ \cos^2\left(\frac{\pi x}{d}\right), \rho \right\} \right] \quad (5.4.5)$$

where the absorption rate  $\gamma_{\text{abs}}$  determines the mean number of absorbed photons  $n_0^{\text{abs}}$ , which can be found by solving Eq. (5.2.9) with the Rayleigh absorption cross-section  $\sigma_{\text{abs}}(\omega) = \omega \operatorname{Im}[\alpha]/c\epsilon_0$ .

$$n_0^{\text{abs}} = \frac{4\sigma_{\text{abs}} \lambda_G E_G}{hc a_G}. \quad (5.4.6)$$

Because the laser pulse is only active for a short time, 10ns [11], we can neglect the motion of the particle during the pulse and integrate (5.4.5) explicitly to find the Fourier coefficients of the absorption mask in terms of modified Bessel functions as,

$$R_n^{(\text{abs})}(\xi) = \exp\left[-\frac{n_0^{\text{abs}}}{2}(1 - \cos \pi \xi)\right] I_n\left[\frac{n_0^{\text{abs}}}{2}(1 - \cos \pi \xi)\right]. \quad (5.4.7)$$

We can then describe the total effect of the grating by convolving the coherent and absorption effects

$$\tilde{B}_n\left(\frac{s}{d}\right) = \sum_k B_{n-k}\left(\frac{s}{d}\right) R_k\left(\frac{s}{d}\right) \quad (5.4.8)$$

to arrive at our total Talbot coefficients

$$\tilde{B}_n(\xi) = e^{n_0 \sin^2(\pi\xi/2)} \sum_k J_{n-k}(\phi_0 \sin \pi\xi) I_k \left\{ \frac{n_0^{\text{abs}}}{2} [1 - \cos(\pi\xi/2)] \right\}. \quad (5.4.9)$$

By noting that  $J_{-n}(x) = J_n(x)$  and using Graf's addition theorem for mixtures of modified and regular Bessel functions, which in this case reads [120],

$$\left( \frac{a-b}{a+b} \right)^{n/2} J_n(-\text{sgn}(b+a)\sqrt{a^2-b^2}) = \sum_k J_k(a) I_{k+n}(b) \quad (5.4.10)$$

we can simplify the Talbot coefficients to be

$$\tilde{B}_n(\xi) = e^{-\zeta_{\text{abs}}(\xi)} \left[ \frac{\zeta_{\text{coh}}(\xi) + \zeta_{\text{abs}}(\xi)}{\zeta_{\text{coh}}(\xi) - \zeta_{\text{abs}}(\xi)} \right]^{n/2} J_n \left[ \text{sgn}\{\zeta_{\text{coh}}(\xi) - \zeta_{\text{abs}}(\xi)\} \sqrt{\zeta_{\text{coh}}^2(\xi) - \zeta_{\text{abs}}^2(\xi)} \right] \quad (5.4.11)$$

where we have made the substitutions  $\zeta_{\text{coh}}(\xi) = \phi_0 \sin \pi\xi$  and  $\zeta_{\text{abs}}(\xi) = \frac{n_0^{\text{abs}}}{2}(1 - \cos \pi\xi)$ .

If the effects of scattering are of any concern, they can be included by another convolution with the scattering mask derived from the equivalent Lindblad term as the absorption [119]

$$R_n^{(\text{Sca})}(\xi) = \exp \left[ -\frac{n_0^{\text{sca}}}{2} \left( 1 - 3 \cos(\pi\xi) \frac{\sin \pi\xi - j_1(\pi\xi)}{2\pi\xi} \right) \right] I_n \left[ \frac{n_0^{\text{sca}}}{2} \left( 3 \frac{\sin \pi\xi - j_1(\pi\xi)}{2\pi\xi} - \cos \pi\xi \right) \right] \quad (5.4.12)$$

where the mean number of photons is  $n_0^{\text{sca}} = \frac{\sigma_{\text{sca}} \lambda \epsilon_0}{\pi \text{Re}[\alpha_p]} \phi_0$  and the scattering cross-section is  $\sigma_{\text{sca}} = (2\pi/\lambda)^4 |\alpha_p|^2 / 6\pi\epsilon_0^2$ . For the materials considered here,  $n_0^{\text{sca}} \ll 1$  in the point-like regime. Therefore the scattering effect is negligible. This, however, does not continue to hold in the Mie regime.

### 5.4.2 Mie Theory

In order to put sufficiently low bounds on the collapse model we are testing, we must use larger systems. For tests of CSL this means we must increase the mass of



our particles. Increasing the mass of a spherical particle necessarily means that we must increase its radius. The treatment to find the Talbot coefficients given in the preceding section is only valid for particles whose radii is significantly smaller than the wavelength of the grating laser. That is  $kR \ll 1$ . For particles with a size parameter  $kR \gtrsim 1$  we can no longer use the Rayleigh approximation. Thankfully, however, Mie theory provides us with exact solutions to the scattering problem for particles of arbitrary size. In this section we follow the derivation of Mie theory following the treatment given in [26]. We begin by finding a set of vector harmonic functions which we can use to rewrite the electric field as a weighted sum of these functions. Then we solve for the relevant expansion coefficients to simplify the expression of the electric field. Finally, we use this formulation to solve for the scattering amplitudes of each component of the scattered electric field.

As we are interested in the scattering by a sphere we aim to rewrite the fields in spherical polar coordinates. The fields must solve the Helmholtz equation,

$$\begin{aligned}\nabla^2 \mathbf{E} + k^2 \mathbf{E} &= 0 \\ \nabla^2 \mathbf{H} + k^2 \mathbf{H} &= 0\end{aligned}\tag{5.4.13}$$

where  $k = \omega^2 \epsilon \mu$ . They must also be divergence free,

$$\begin{aligned}\nabla \cdot \mathbf{E} &= 0 \\ \nabla \cdot \mathbf{H} &= 0\end{aligned}\tag{5.4.14}$$

and cannot be independent,

$$\begin{aligned}\nabla \times \mathbf{E} &= i\omega\mu\mathbf{H} \\ \nabla \times \mathbf{H} &= i\omega\epsilon\mathbf{E}.\end{aligned}\tag{5.4.15}$$

We find that the spherical vector harmonics fulfil all necessary conditions,

$$\mathbf{M}_{e,m,n} = \nabla \times (\mathbf{r}\psi_{e,m,n})\tag{5.4.16a}$$

$$\mathbf{M}_{o,m,n} = \nabla \times (\mathbf{r}\psi_{o,m,n})\tag{5.4.16b}$$

$$\mathbf{N}_{e,m,n} = \frac{\nabla \times \mathbf{M}_{e,m,n}}{k}\tag{5.4.16c}$$

$$\mathbf{N}_{o,m,n} = \frac{\nabla \times \mathbf{M}_{o,m,n}}{k}.\tag{5.4.16d}$$

Type	First Kind	Second Kind
Spherical Bessel Functions	$j_n(x)$	$y_n(x)$
Spherical Hankel Functions	$h_n^{(1)}(x) = j_n(x) + iy_n(x)$	$h_n^{(2)}(x) = j_n(x) - iy_n(x)$

Table 5.2: Spherical Bessel and Hankel functions.

These are extensions to the scalar spherical harmonics that are solutions to the Laplace equation in spherical coordinates [121]. We use  $\mathbf{r}$  as the radius vector and we have the generating functions,

$$\psi_{e,m,n} = \cos m\phi P_n^m(\cos\theta) z_n(kr) \quad (5.4.17a)$$

$$\psi_{o,m,n} = \sin m\phi P_n^m(\cos\theta) z_n(kr) \quad (5.4.17b)$$

where  $z_n(x)$  is any of the spherical Bessel functions given in Table 5.2, and  $P_n^m(\cos\theta)$  are the Legendre functions of the first kind with degree  $n$  and order  $m$ . These generating functions give us four vector spherical harmonic functions,

Any solution to the field equations can be expanded into an infinite series of the equations (5.4.16). We can expand the electric field for an  $x$ -polarized wave in spherical harmonics,  $\mathbf{E}_i = E_0 \mathbf{e}_x \exp[ikr \cos\theta]$  in our vector spherical harmonics as,

$$\begin{aligned} \mathbf{E}_i = \sum_{m=0}^{\infty} \sum_{n=m}^{\infty} ( & B_{e,m,n} \mathbf{M}_{e,m,n} + B_{o,m,n} \mathbf{M}_{o,m,n} \\ & + A_{e,m,n} \mathbf{N}_{e,m,n} + A_{o,m,n} \mathbf{N}_{o,m,n} ) \end{aligned} \quad (5.4.18)$$

where the  $A$  and  $B$  coefficients are to be determined. From the orthogonality between  $\sin m\phi$  and  $\cos m'\phi$  for all  $m$  and  $m'$ , we can say that the vectors  $\mathbf{M}_{e,m,n}$  and  $\mathbf{M}_{o,m,n}$  are orthogonal. We also note that  $(\mathbf{N}_{o,m,n}, \mathbf{N}_{e,m,n})$ ,  $(\mathbf{M}_{o,m,n}, \mathbf{N}_{o,m,n})$ , and  $(\mathbf{M}_{e,m,n}, \mathbf{N}_{e,m,n})$  are all mutually orthogonal sets of functions. From these orthogonality conditions we can find expressions for the  $A$  and  $B$  coefficients. We find that  $B_{e,m,n} = A_{o,m,n} = 0$  for all  $m$  and  $n$ , and the remaining coefficients

vanish unless  $m = 1$ . This then leaves us with the following expansion coefficients,

$$A_{e,1,n} = -iE_0i^n \frac{2n+1}{n(n+1)} \quad (5.4.19a)$$

$$B_{o,1,n} = i^n E_0 \frac{2n+1}{n(n+1)}. \quad (5.4.19b)$$

We can now fully describe the wave in terms of spherical harmonics,

$$\mathbf{E}_i = \sum_{n=1}^{\infty} E_n (\mathbf{M}_{o,1,n}^{(1)} - i\mathbf{N}_{e,1,n}^{(1)}) \quad (5.4.20)$$

where  $E_n = i^n E_0(2n+1)/n(n+1)$  and we append the superscript (1) to the harmonics whose radial component is dependant on the generating functions specified by  $j_n(x)$ . If the field  $\mathbf{E}_i$  is incident on a homogeneous, isotropic sphere of radius  $R$  and we apply the boundary conditions,

$$(\mathbf{E}_i + \mathbf{E}_s - \mathbf{E}_I) \times \mathbf{e}_r = 0 \quad (5.4.21)$$

we can determine the internal  $\mathbf{E}_I$  and scattered  $\mathbf{E}_s$  fields,

$$\mathbf{E}_I = \sum_{n=1}^{\infty} E_n (c_n \mathbf{M}_{o,1,n}^{(1)} - i d_n \mathbf{N}_{e,1,n}^{(2)}) \quad (5.4.22a)$$

$$\mathbf{E}_s = \sum_{n=1}^{\infty} E_n (i a_n \mathbf{N}_{e,1,n}^{(3)} - b_n \mathbf{M}_{o,1,n}^{(3)}) \quad (5.4.22b)$$

where the superscript (3) specifies that the radial component of the relevant generating function is determined by the spherical Hankel function  $h_n^{(1)}(x)$ . For a particle with a permeability  $\mu$  equal to that of the surrounding medium, we find the coefficients inside the particle to be,

$$c_n = \frac{\sqrt{\epsilon} \psi_n(x) \xi_n'(x) - \sqrt{\epsilon} \xi_n(x) \psi_n'(x)}{\psi_n(\sqrt{\epsilon}x) \xi_n'(x) - \sqrt{\epsilon} \xi_n(x) \psi_n'(\sqrt{\epsilon}x)} \quad (5.4.23a)$$

$$d_n = \frac{\psi_n(x) \xi_n'(x) - \xi_n(x) \psi_n'(x)}{\psi_n(\sqrt{\epsilon}x) - \xi_n'(x) \psi_n'(\sqrt{\epsilon}x)} \quad (5.4.23b)$$

and the coefficients of the scattered functions are,

$$a_n = \frac{\sqrt{\epsilon}\psi_n(\sqrt{\epsilon}x)\psi'_n(x) - \psi_n(x)\psi'_n(\sqrt{\epsilon}x)}{\sqrt{\epsilon}\psi_n(\sqrt{\epsilon}x)\xi'_n(x) - \xi_n(x)\psi'_n(\sqrt{\epsilon}x)} \quad (5.4.24a)$$

$$b_n = \frac{\psi_n(\sqrt{\epsilon}x)\psi'_n(x) - \sqrt{\epsilon}\psi_n(x)\psi'_n(\sqrt{\epsilon}x)}{\psi_n(\sqrt{\epsilon}x)\xi'_n(x) - \sqrt{\epsilon}\xi_n(x)\psi'_n(\sqrt{\epsilon}x)} \quad (5.4.24b)$$

where  $\epsilon$  is the relative permittivity of the particle, such that  $\sqrt{\epsilon} = m$  is its complex refractive index, and we have made use of the Riccati-Bessel functions,

$$\psi_n(\rho) = \rho j_n(\rho) \quad (5.4.25a)$$

$$\xi_n(\rho) = \rho h_n^{(1)}(\rho). \quad (5.4.25b)$$

We can now define the scattering, extinction, and absorption cross-sections for a large particle,

$$\sigma_{sca} = \frac{2\pi}{k^2} \sum_{n=1}^{\infty} (2n+1)(|a_n|^2 + |b_n|^2) \quad (5.4.26a)$$

$$\sigma_{ext} = \frac{2\pi}{k^2} \sum_{n=1}^{\infty} (2n+1) \operatorname{Re}[a_n + b_n] \quad (5.4.26b)$$

$$\sigma_{abs} = \sigma_{ext} - \sigma_{sca}. \quad (5.4.26c)$$

Finally we define the scattering matrix elements,

$$S_1(\theta) = \sum_n \frac{2n+1}{n(n+1)} (a_n \pi_n(\theta) + b_n \tau_n(\theta)) \quad (5.4.27a)$$

$$S_2(\theta) = \sum_n \frac{2n+1}{n(n+1)} (a_n \tau_n(\theta) + b_n \pi_n(\theta)) \quad (5.4.27b)$$

which makes use of the angle-dependant functions,

$$\pi_n(\theta) = -\frac{dP_n(\cos\theta)}{d\theta} \frac{1}{\sin\theta} \quad (5.4.28a)$$

$$\tau_n(\theta) = \frac{d}{d\theta} \left( -\frac{dP_n(\cos\theta)}{d\theta} \right). \quad (5.4.28b)$$

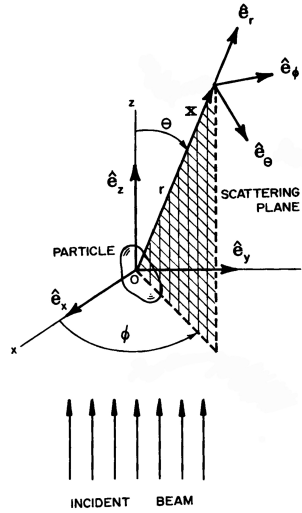


Figure 5.9: Light scattering off a particle showing the scattering plane and the components of the scattered light  $\hat{e}_\theta$ ,  $\hat{e}_\phi$ , and  $\hat{e}_r$ . Because the wave is transverse in the far-field,  $\hat{e}_r = 0$  [26].

From this, we define the components of the scattered light to be,

$$E_{s\theta} = E_0 \frac{e^{ikr}}{-ikr} \cos \phi S_2(\theta) \quad (5.4.29a)$$

$$E_{s\phi} = -E_0 \frac{e^{ikr}}{-ikr} \sin \phi S_1(\theta). \quad (5.4.29b)$$

Here we have defined the scattered field in terms of its  $\theta$  and  $\phi$  components relative to the scattering plane as shown in Fig. 5.9.

### 5.4.3 Talbot Coefficients Beyond the Point-Like Approximation

This section builds on the theory set out in [105] and progresses to correct an error presented in that paper. The previous work uses a scalar scattering function ignoring the polarisation of the scattered light, thus underestimating the decoherence due to the scattering of grating photons. However, we consider the polarization of the scattered light, by using a vector scattering function, to ensure the full scattering decoherence that takes place in the laser grating and produce a more accurate function describing the Talbot coefficients.

To model the coherent effects we must first find the longitudinal force on the particle as a result of the laser beam. We also note that for the short pulse durations that we consider here, we can neglect transverse forces. By integrating the stress tensor over a spherical surface surrounding the particle, we find the longitudinal force to be,

$$\begin{aligned} \frac{F_z(z)}{I_0 k^{-2} c^{-1}} = & -(kR)^4 \sum_{l=1}^{\infty} \sum_{m=\pm 1} \text{Im} \left[ l(l+2) \sqrt{\frac{(l-m+1)(l+m+1)}{2l+3}(2l+1)} \right. \\ & (2a_{l+1,m} a_{l,m}^* + a_{l+1,m} A_{l,m}^* + A_{l+1,m} a_{l,m}^* + 2b_{l+1,m} b_{l,m}^* + b_{l+1,m} B_{l,m}^* + B_{l+1,m} b_{l,m}^*) \\ & \left. + m(2a_{l,m} b_{l,m}^* + a_{l,m} B_{l,m}^* + A_{l,m} b_{l,m}^*) \right] \end{aligned} \quad (5.4.30)$$

where  $a_{l,m} = a_l A_{l,m}$  and  $b_{l,m} = b_l B_{l,m}$ . Here  $a_l$  and  $b_l$  are the scattering coefficients from Mie theory given in Eq. (5.4.24). We also use the coefficients,

$$A_{l,m} = \frac{i^{l+1} \sqrt{4\pi(2l+1)}}{2\alpha^2 \sqrt{l(l+1)}} m \zeta(l+1) \quad (5.4.31a)$$

$$B_{l,m} = \frac{i^l \sqrt{4\pi(2l+1)}}{2\alpha^2 \sqrt{l(l+1)}} \zeta(l) \quad (5.4.31b)$$

where  $\zeta(l) = \frac{1}{2}[(-1)^l \exp(-ikz) + \exp(ikz)]$  where  $z$  represents the  $z$  coordinate of the particle's center of mass. Because we only consider a linearly polarized standing wave, the force takes the form  $F_z(z) = -F_0 \sin 2kz$ . We determine  $F_0$  by evaluating Eq. (5.4.30) at  $z = -\lambda/8$ . We can compare this to the value expected from the Rayleigh approximation for various sizes of particles to see the deviation from Mie theory as the particle size increases. The relationship between the force and the potential is simply given by  $F(z) = -\nabla V(z)$ , which gives a potential of  $V(z) = -\frac{F_0}{k} \cos^2 kz$ . Now if we perform the same integral as in Eq. (5.2.7) we find the phase parameter to be,

$$\phi_0 = \frac{F_0 \tau}{k \hbar}. \quad (5.4.32)$$

If we assume a rectangular pulse such that the laser intensity  $I_0 = 4P_G/a_G = c\epsilon_0 |E_0|^2/2$  remains constant during the duration of the pulse, we can show that the pulse duration has the relation,

$$\tau = \frac{8}{c\epsilon_0 |E_0|^2} \frac{E_G}{a_G}. \quad (5.4.33)$$

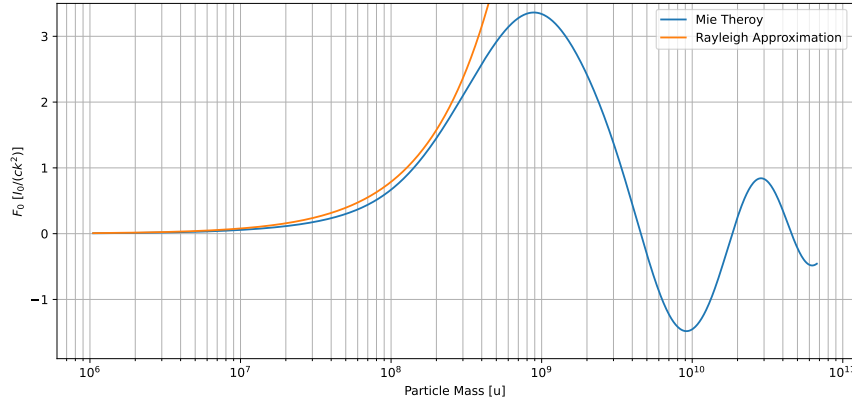


Figure 5.10: Amplitude of the optical force  $F_0$ , in units of  $I_0/(ck^2)$ , as a function of the mass of a silicon nano-sphere in a beam with wavelength  $\lambda = 354\text{nm}$ . In orange is the Rayleigh approximation result, and in blue is the result as calculated by Eq. (5.4.30) based on a Mie theory treatment.

From this we can write the phase parameter as,

$$\phi_0 = \frac{8F_0}{\hbar c \epsilon_0 k |E_0|^2} \frac{E_G}{a_G} \quad (5.4.34)$$

The incoherent effects resulting from the scattering of grating photons can be described by the Lindblad superoperator which gives the decoherence effect of the scattered grating photons,

$$\mathcal{L}_{sca}^\mu(\rho) = |\alpha(t)|^2 \int (2\mathcal{T}_{\mathbf{k},\mathbf{c},\mu}(\hat{r})\rho\mathcal{T}_{\mathbf{k},\mathbf{c},\mu}^*(\hat{r}) - \{|\mathcal{T}_{\mathbf{k},\mathbf{c},\mu}(\hat{r})|^2, \rho\}) \delta(\omega_k - \omega_0) d\mathbf{k} \quad (5.4.35)$$

where here  $\alpha(t)$  is the photon number, and  $\mu = \hat{e}_\theta, \hat{e}_\phi$  is the polarization vector of the scattered light with respect to the scattering plane as shown in Fig. 5.9. The collisional operators  $\mathcal{T}_{\mathbf{k},\mathbf{c},\mu}(\hat{r})$  describe the scattering out of the cavity mode and are defined as,

$$\begin{aligned} \mathcal{T}_{\mathbf{k},\mathbf{c},\mu}(\hat{r}) &= \int \langle \mathbf{k} | \hat{T}^\mu(\hat{r}) | \mathbf{k}' \rangle \langle \mathbf{k}' | \mathbf{c} \rangle d\mathbf{k}' \\ &= \frac{ic^2}{2\pi\omega_0} \int \langle \mathbf{k}' | \mathbf{c} \rangle f_\mu(\mathbf{k}, \mathbf{k}') e^{-i(\mathbf{k}-\mathbf{k}')\cdot\hat{r}} d\mathbf{k}' \end{aligned} \quad (5.4.36)$$

where  $f_\mu(\mathbf{k}, \mathbf{k}')$  is the scattering amplitude with polarisation  $\mu$ , and  $|\mathbf{c}\rangle$  is the mode function of the standing wave. The mode function is defined such that

in position representation it reads,  $\langle \mathbf{r} | \mathbf{c} \rangle = f(\mathbf{r})/\sqrt{V_0}$ , where  $V_0$  is the mode volume of the standing wave. If we assume that the laser pulse duration is short enough that free evolution during the interaction is negligible and we are working in the longitudinal eikonal approximation as discussed in section 5.2, we can describe the effect on the matter wave due to scattering by the scattering mask  $R_{sca}^\mu(z, z') = \exp[\int \mathcal{L}_{sca}^\mu(z, z') d\tau]$  in the position representation, which is given by,

$$\mathcal{L}_{sca}^\mu(z, z') = |\alpha(t)|^2 \int \delta(\omega_k - \omega_0) [2\mathcal{T}_{\mathbf{k}, \mathbf{c}, \mu}(z) \mathcal{T}_{\mathbf{k}, \mathbf{c}, \mu}^*(z') - |\mathcal{T}_{\mathbf{k}, \mathbf{c}, \mu}(z)|^2 - |\mathcal{T}_{\mathbf{k}, \mathbf{c}, \mu}(z')|^2]. \quad (5.4.37)$$

We also make the assumption that the waist of the laser is sufficiently larger than the particle radius such that we can approximate the standing wave by the function  $\mathbf{E}(\mathbf{r}) \approx E_0 \hat{\mathbf{x}} \cos(kz)$ . Thus we use the mode function  $\langle z | \mathbf{c} \rangle = \cos(kz)/\sqrt{V_0}$  to show,

$$\mathcal{T}_{\mathbf{k}, \mathbf{c}, \mu}(z) = \sqrt{\frac{2\pi^3}{V_0}} (\mathcal{T}_{\mathbf{k}_0, \mathbf{k}, \mu}^*(z) + \mathcal{T}_{-\mathbf{k}_0, \mathbf{k}, \mu}^*(z)) \quad (5.4.38)$$

where we have used the scattering operators  $\mathcal{T}_{\mathbf{k}_0, \mathbf{k}, \mu}(z) = \langle \mathbf{k}_0 | \hat{T}^\mu(z) | \mathbf{k} \rangle$ . By using the substitutions  $\mathbf{n} = \mathbf{k}'/|k|$ ,  $z \rightarrow z - s/2$ , and  $z' \rightarrow z + s/2$ , and assuming that the incoming wave  $\mathbf{k}$  is pointing in the  $z$  direction, we can rewrite Eq. (5.4.37) as,

$$\begin{aligned} \mathcal{L}_{sca}^\mu \left( z - \frac{s}{2}, z + \frac{s}{2} \right) &= \frac{|\alpha(t)|^2 \pi c}{V_0} \left[ \int |f_\mu(k, k\mathbf{n})|^2 (e^{-i(1-n_z)ks} - 1) d\Omega \right. \\ &\quad + \int f_\mu^*(k, k\mathbf{n}) f_\mu(-k, k\mathbf{n}) e^{-i2kz} (e^{ikn_z s} - \cos(ks)) d\Omega \\ &\quad + \int f_\mu^*(-k, k\mathbf{n}) f_\mu(k, k\mathbf{n}) e^{i2kz} (e^{ikn_z s} - \cos(ks)) d\Omega \\ &\quad \left. + \int |f_\mu(-k, k\mathbf{n})|^2 (e^{i(1+n_z)ks} - 1) d\Omega \right] \end{aligned} \quad (5.4.39)$$

where  $\Omega$  is the solid angle associated with the outgoing wave  $k'$ . Exploiting the spherical symmetry of the nano particle we obtain a symmetry in the scattering amplitude,  $f_\mu(-k, k\mathbf{n}) = f_\mu(k, -k\mathbf{n})$ , and the scattering mask,

$$R_{sca}^\mu \left( z - \frac{s}{2}, z + \frac{s}{2} \right) = \exp [F^\mu(s) + a^\mu(s) \cos(2kz) + ib^\mu(s) \sin(2kz)]. \quad (5.4.40)$$



Here we make use of the polarisation dependant scattering functions from Eq. (5.4.39) as,

$$a^\mu(s) = \frac{8\pi}{\hbar\omega} \frac{E_G}{a_G} \int \text{Re} [f_\mu^*(k, k\mathbf{n}) f_\mu(-k, k\mathbf{n})] [\cos(kn_z s) - \cos(ks)] d\Omega \quad (5.4.41a)$$

$$b^\mu(s) = \frac{8\pi}{\hbar\omega} \frac{E_G}{a_G} \int \text{Im} [f_\mu^*(k, k\mathbf{n}) f_\mu(-k, k\mathbf{n})] \sin(kn_z s) d\Omega \quad (5.4.41b)$$

$$F^\mu(s) = \frac{8\pi}{\hbar\omega} \frac{E_G}{a_G} \int |f(k, k\mathbf{n})|^2 [\cos((1 - n_z)ks) - 1] d\Omega \quad (5.4.41c)$$

where we have expressed the time integral in terms of the laser parameters  $\int |\alpha(t)|^2 d\tau = 4V_0 E_G / \hbar\omega a_G$ . The integrals over the sphere are solved numerically. This is not a trivial task. The area element of a sphere is  $d\Omega = \sin\theta d\theta d\phi$  which is a function of  $\theta$ . As a result the closer we get to the poles, i.e.  $\theta \rightarrow 0$ , the area element gets smaller leading to numerical errors. By assigning weights to each of the area patches, we can approximate the integral as,

$$\int f(\mathbf{r}) d\Omega \approx \sum_{i=0}^{N-1} w_i f(\mathbf{r}_i). \quad (5.4.42)$$

We use the Lebedev quadrature rules that determines the points  $\mathbf{r}_i$  and their relative weights  $w_i$  which are chosen to correctly reproduce spherical harmonics [122].

To complete this set of equations, we must determine the scattering amplitude for the polarisation  $\mu = \hat{e}_\theta, \hat{e}_\phi$  by using results from Mie theory. We can define the scattered light with respect to the incoming wave via [26],

$$E_{s,\theta} \approx E_0 \frac{e^{ikr}}{-ikr} \cos\phi S_2(\cos\theta) \quad (5.4.43a)$$

$$E_{s,\phi} \approx -E_0 \frac{e^{ikr}}{-ikr} \sin\phi S_1(\cos\theta) \quad (5.4.43b)$$

from which we can extract the scattering amplitudes,

$$f_\theta(k, k\mathbf{n}) = \cos\phi S_2(\cos\theta)/k \quad (5.4.44a)$$

$$f_\phi(k, k\mathbf{n}) = \sin\phi S_1(\cos\theta)/k \quad (5.4.44b)$$

where the functions  $S_1$  and  $S_2$  are the same as in Eq. (5.4.27). To account for the incoherent effects as a result of the absorption of grating photons, we follow

the same procedure as in section 5.4.1, but replace the absorption cross section with the Mie equivalent given in Eq. (5.4.26c).

Putting our absorption and scattering decoherence masks into a single mask we get,

$$\begin{aligned}
 R_{tot} \left( z - \frac{s}{2}, z + \frac{s}{2} \right) &= R_{Sca}^\theta \left( z - \frac{s}{2}, z + \frac{s}{2} \right) R_{Sca}^\phi \left( z - \frac{s}{2}, z + \frac{s}{2} \right) R_{abs} \left( z - \frac{s}{2}, z + \frac{s}{2} \right) \\
 &= \exp \left[ \int_0^{t_{pulse}} \left( F(s) + a(s) \cos(2kz) + ib(s) \sin(2kz) \right. \right. \\
 &\quad \left. \left. - 2n_0^{abs} \sin^2(kz) \sin^2(-2ks) \right) d\tau \right]
 \end{aligned} \tag{5.4.45}$$

where  $a(s) = a^\theta(s) + a^\phi(s)$ ,  $b(s) = b^\theta(s) + b^\phi(s)$ , and  $F(s) = F^\theta(s) + F^\phi(s)$ . We then take the Fourier components of the decoherence mask and convolve them with the coherent effects as we did in the Rayleigh regime to find the total Talbot coefficients to be,

$$\begin{aligned}
 \tilde{B}_n \left( \frac{s}{d} \right) &= e^{F - \zeta_{abs}} \sum_{k=-\infty}^{\infty} \left( \frac{\zeta_{coh} \left( \frac{s}{d} \right) + a(s) + \zeta_{abs} \left( \frac{s}{d} \right)}{\zeta_{coh} \left( \frac{s}{d} \right) - a(s) - \zeta_{abs} \left( \frac{s}{d} \right)} \right)^{\frac{n+k}{2}} \\
 &\quad J_k(b(s)) J_{n+k} \left( \operatorname{sgn} \left[ \zeta_{coh} \left( \frac{s}{d} \right) - a(s) - \zeta_{abs} \left( \frac{s}{d} \right) \right] \right) \\
 &\quad \sqrt{\zeta_{coh}^2 \left( \frac{s}{d} \right) - (a(s) + \zeta_{abs} \left( \frac{s}{d} \right))^2}
 \end{aligned} \tag{5.4.46}$$

where we have used the same definitions of  $\zeta_{coh}(\xi)$  and  $\zeta_{abs}(\xi)$  as before.

## 5.5 Decoherence within the Interferometer

We now include the effects of environmental sources of decoherence into our theory. We use [11] to inform our analysis of the decoherence. The last line in Eq. (5.3.15) gives the effect of environmental decoherence. It acts as a term reducing the amplitude of the interference fringes by an amount  $R_n$ . As we are considering multiple sources of decoherence, it is more convenient to consider the reduction term from each source. This gives a total reduction to the fringe

amplitudes of  $R_n^{tot} = \prod_i R_n^{(i)}$  for each source  $i$ . We can introduce the dimensionless integration variable  $\vartheta$  to simplify the decoherence terms to be

$$R_n^{(i)} = \exp \left\{ \int_0^1 [t_2 \Gamma_i(t_1 + t_2 \vartheta) + t_1 \Gamma_i(t_1 - t_1 \vartheta)] \left[ g_i \left( \frac{\hbar t_2 \vartheta}{mD} \right) - 1 \right] d\vartheta \right\}. \quad (5.5.1)$$

For sources of decoherence that have no time dependence, we can further simplify the decoherence reduction terms to be,

$$R_n^{(i)} = \exp \left\{ -\Gamma_i \left[ 1 - f_i \left( \frac{\hbar t_2}{mD} \right) \right] (t_1 + t_2) \right\} \quad (5.5.2)$$

where

$$f(x) = \int_0^1 g(x\vartheta) d\vartheta \quad (5.5.3)$$

which determines the decoherence strength for a finite interference path separation on average. The decoherence process takes away full information about the particle when  $f(x) = 0$  causing the matter-wave to decohere at the maximum rate  $\Gamma$ . We consider four independent sources of environmental decoherence:

1. Absorption of Thermal Radiation
2. Emission of Thermal Radiation
3. Elastic Scattering of Thermal Radiation
4. Collisions with Residual Gas Particles

For each source, we must determine the decoherence rate  $\Gamma(t)$  and the decoherence function  $g(x)$ .

### 5.5.1 Absorption of Thermal Radiation

While the particle is in free fall, it will absorb photons from the isotropic background field. Each photon of frequency  $\omega$  transfers  $\hbar\omega/c$  of momentum to the particle. In one dimension, the master equation for this process is,

$$\mathcal{L}_{abs}\rho = \int d\omega \gamma_{abs}(\omega) \left[ \int_{|\mathbf{n}|=1} \frac{d^2n}{4\pi} \exp \left( \frac{i\omega n_z \times}{c} \right) \rho \exp \left( -\frac{i\omega n_z \times}{c} \right) - \rho \right] \quad (5.5.4)$$

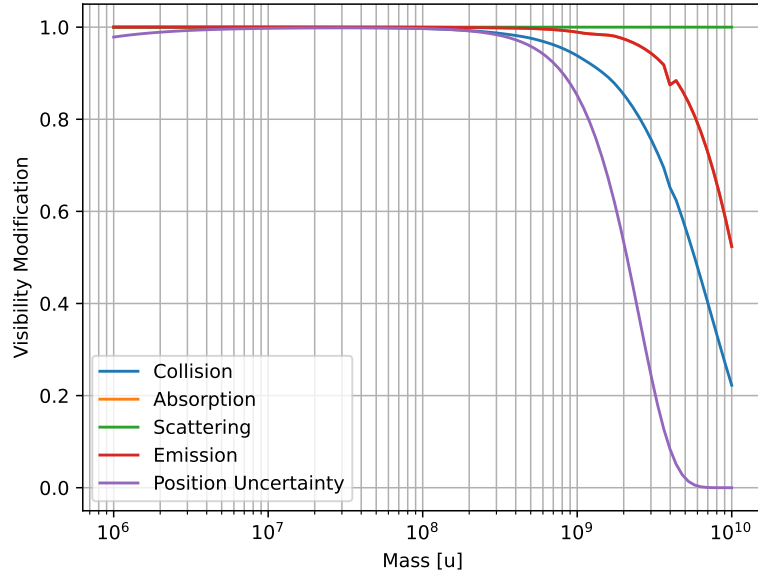


Figure 5.11: The effect on the visibility of the interference pattern by each source of decoherence and the measurement uncertainty for a MAQRO-like experiment for varying masses. The values of  $\phi_0$  and  $t_2$  are optimised using the method given in sec 6.5.

where the spectral absorption rate is given by,

$$\gamma_{abs}(\omega) = \frac{(\omega/\pi c)^2 \sigma_{abs}(\omega)}{\exp(\hbar\omega/k_B T_{env}) - 1}. \quad (5.5.5)$$

With these equations, we can now determine the decoherence parameters,

$$\Gamma_{abs} = \int \gamma_{abs}(\omega) d\omega \quad (5.5.6a)$$

$$g_{abs}(x) = \int \frac{\gamma_{abs}(\omega)}{\Gamma_{abs}} \text{sinc}\left(\frac{\omega x}{c}\right) d\omega \quad (5.5.6b)$$

$$f_{abs}(x) = \int \frac{\gamma_{abs}(\omega)}{\Gamma_{abs}} \frac{\text{Si}(\omega x/c)}{\omega x/c} d\omega \quad (5.5.6c)$$

where  $\text{Si}(x) = \int_0^x \sin(t)/t dt$  is the sine integral.

### 5.5.2 Emission of Thermal Radiation

The emission of radiation is the time reversal of the absorption and has the same effect on the particle's matter-wave. If the emission pattern is isotropic, we can use the absorption master equation Eq. (5.5.4) replacing the absorption rate with the spectral emission rate for internally hot particles,

$$\gamma_{emi}(\omega, T_{int}) = \left(\frac{\omega}{\pi c}\right)^2 \sigma_{abs}(\omega) \exp\left(-\frac{\hbar\omega}{k_B T_{int}}\right) \quad (5.5.7)$$

and we can use parameters of the same form as given in Eq. (5.5.6). If, however, the particle cools down significantly during its free-fall, the emission rate will be dependant on time and we must use the reduction term,

$$R_n^{(emi)} = \exp\left\{\int d\omega \int_0^1 [t_1 \gamma_{emi}(\omega, T_{int}(t_1 - t_1\vartheta)) + t_2 \gamma_{emi}(\omega, T_{int}(t_1 + t_2\vartheta))] \left[\text{sinc}\left(\frac{nh\omega t_1 t_2}{(t_1 + t_2)mcd}\vartheta\right) - 1\right] d\vartheta\right\}. \quad (5.5.8)$$

The time dependence of the particle's internal temperature can be estimated by solving the differential equation  $mc_m \partial_t T_{int} = \int \hbar\omega [\gamma_{abs}(\omega) - \gamma_{emi}(\omega, T_{int})] d\omega$  where  $c_m$  is the specific heat capacity of the particle material.

### 5.5.3 Elastic Scattering of Thermal Radiation

The long wavelengths of the thermal background radiation allows us to use the Rayleigh approximation to determine the rate of decoherence from this source. The decoherence is governed by the master equation,

$$\mathcal{L}_{sca} \hat{\rho} = \int \gamma_{sca}(\omega) \left\{ \exp\left[\frac{i\omega(n_z - n'_z)\hat{z}}{c}\right] \hat{\rho} \exp\left[\frac{i\omega(n'_z - n_z)\hat{z}}{c}\right] \frac{d^2 n d^2 n'}{16\pi^2} - \hat{\rho} \right\} d\omega \quad (5.5.9)$$

where the spectral scattering rate is,

$$\gamma_{sca} = \frac{(\omega/\pi c)^2 \sigma_{sca}(\omega)}{\exp(\hbar\omega/k_B T_{env}) - 1}. \quad (5.5.10)$$

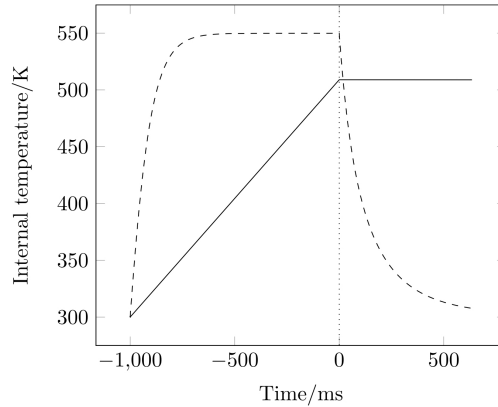


Figure 5.12: The internal temperature for  $10^6$ u spherical nano particles of different materials reproduced from [11]. While the particle is in the trap, the internal temperature increases as a result of absorbing photons from the trapping laser. The silica (dashed line) particle reaches an equilibrium temperature while the silicon particle (solid line) continues to heat. When the trap is switched off, the silica particle rapidly cools due to emission of thermal radiation while the silicon particle's temperature remains constant.

This gives the decoherence parameters,

$$\Gamma_{\text{sca}} = \int \gamma_{\text{sca}}(\omega) d\omega \quad (5.5.11\text{a})$$

$$g_{\text{sca}}(z) = \int \frac{\gamma_{\text{sca}}(\omega)}{\Gamma_{\text{sca}}} \text{sinc}^2\left(\frac{\omega z}{c}\right) d\omega \quad (5.5.11\text{b})$$

$$f_{\text{sca}}(z) = \int \frac{\gamma_{\text{sca}}}{\Gamma_{\text{sca}}} \left[ \frac{\text{Si}(2\omega z/c)}{\omega z/c} - \text{sinc}^2\left(\frac{\omega z}{c}\right) \right] d\omega. \quad (5.5.11\text{c})$$

#### 5.5.4 Collisions with Residual Gas Particles

To simplify the calculations, we can assume that each collision event transfers sufficiently many grating momenta that it fully resolves adjacent interference paths such that the decoherence function  $g_{\text{col}}(x)$  vanishes for  $x \neq 0$  simplifying the reduction term to  $R_n^{(\text{col})} = \exp[-\Gamma_{\text{col}}(t_1 + t_2)]$ . We also assume that the residual gas with pressure  $p_g$  is made up of nitrogen (with a mass of 28 amu) and

is in thermal equilibrium with the environment. The mean velocity of the gas particles thus reads as  $v_g = \sqrt{2k_B T_{env}/m_g}$ . We obtain an expression for the total scattering rate from a van der Waals scattering model,

$$\Gamma_{col} \approx \frac{4\pi\Gamma(9/10)}{5\sin(\pi/5)} \left( \frac{3\pi C_6}{2\hbar} \right)^{2/5} \frac{p_g v_g^{3/5}}{k_B T_{env}} \quad (5.5.12)$$

where  $\Gamma(x)$  is the gamma function and the van der Waals coupling constant  $C_6$  is determined by the London formula [123] to be,

$$C_6 \approx \frac{3\alpha_p(\omega = 0)\alpha_g I_g I_p}{32\pi^2 \epsilon_0^2 (I_p + I_g)}. \quad (5.5.13)$$

Here we have used the functions  $\alpha_p$ ,  $\alpha_g$  for the static polarizabilities of the particle and gas, and  $I_p$ ,  $I_g$  as their ionization energies. For nitrogen gas, we use the values  $\alpha_g = 1.74\text{\AA}^3 \times 4\pi\epsilon_0$  and  $I_g = 15.6\text{eV}$  [124]. We can estimate the ionization energy of our particle by using the bulk work function, and their static polarizability is found by using Eq. (5.4.3). For silicon nanospheres we find that  $I_p \approx 5\text{eV}$ , and we set the static permittivity in Eq. (5.4.3) to  $\epsilon = 11.9$ .

### 5.5.5 Position Resolution

We consider the finite position resolution that will affect any experiment. The measured position of the particle  $z$  after a total free-evolution time  $t_1 + t_2$  will be distributed around the “true” value. We assume a linear drift of the spacecraft position with time, as consistent with ESA estimates found during a design study [114] We model this as a convolution with a Gaussian kernel of width,

$$\sigma_m = \sigma_z + (10\text{nm}/100\text{s})(t_1 + t_2). \quad (5.5.14)$$

After applying the Fourier transform and the convolution theorem, we find that this uncertainty can be included as a decoherence term,

$$R_n^{\text{meas}} = \exp \left[ -\frac{1}{2} (nk\sigma_m)^2 \right]. \quad (5.5.15)$$

## 5.6 Including Collapse Models

The last thing we need to include in our theory is the effect of the collapse model we are testing. The effect of collapse models manifest in similar ways to

decoherence mechanisms in our theory, that is they reduce the visibility of the fringes. As a result, we are able to include them as an extra decoherence term,

$$R_n^{\text{Collapse}}(\boldsymbol{\theta}) = \exp \left\{ -\Gamma_{\text{CSL}}(\boldsymbol{\theta}) \left[ 1 - f_{\text{CSL}} \left( \frac{nh t_2}{mD}, \boldsymbol{\theta} \right) \right] (t_1 + t_2) \right\} \quad (5.6.1)$$

where  $\boldsymbol{\theta}$  is a vector containing the physical parameters defining the collapse model that we are interested in estimating. The theory discussed so far has been a general approach to the interferometer that can be applied to any collapse model that manifests as a decoherence source. In our simulations we mainly focus on the Continuous Spontaneous Localisation model (CSL) discussed in section 4.2.4. The CSL effect is constant in time so we can model the decoherence as done in Eq. (5.5.2).

### 5.6.1 CSL in the Rayleigh Regime

For small structures where the inter-particle distance is smaller than the localisation scale  $r_c$ , we can set the master equation for the CSL collapse in one dimension to be [125],

$$\mathcal{L}_{\text{CSL}}\rho = \lambda_c \left( \frac{m}{m_0} \right)^2 \left[ 8\pi^{3/2} r_c^3 \int dz' g(\hat{z} - z') \rho g(\hat{z} - z') - \rho \right] \quad (5.6.2)$$

where  $m_0$  is a reference mass taken to be the mass of a single nucleon. This allows us to determine the decoherence parameters needed for our model,

$$\Gamma_{\text{CSL}} = \left( \frac{m}{m_0} \right)^2 \lambda_c \quad (5.6.3a)$$

$$g(x) = \exp \left( -\frac{x^2}{4r_c^2} \right) \quad (5.6.3b)$$

$$f(x) = \frac{\sqrt{\pi} r_c}{x} \operatorname{erf} \left( \frac{x}{2r_c} \right) \quad (5.6.3c)$$

and we have found  $f(x)$  via Eq. (5.5.3).

### 5.6.2 CSL Beyond the Rayleigh Regime

For the larger particles that we want to use, we must generalise the master equation to particles of all possible radii. We can write the one-dimensional Linblad



superoperator for the state of the particle in the position representation as [126],

$$\mathcal{L}_{CSL}(z, z') = -\frac{\lambda_c(4\pi r_c^2)^{3/2}}{(2\pi\hbar)^3} \int \frac{\tilde{\mu}^2(\mathbf{q})}{m_0^2} e^{-r_c^2 \mathbf{q}^2 / \hbar^2} \left( e^{-iq_z(z-z')/\hbar} - 1 \right) d\mathbf{q} \quad (5.6.4)$$

where  $\tilde{\mu}$  is the Fourier transform of the particle's mass density  $\mu(\mathbf{x})$ ,

$$\tilde{\mu}(\mathbf{q}) = \int e^{-i\mathbf{q}\cdot\mathbf{x}/\hbar} \mu(\mathbf{x}) d\mathbf{x}. \quad (5.6.5)$$

If the particle is a homogeneous sphere, we find the Fourier transform of the mass density to be,

$$\tilde{\mu}(\mathbf{q}) = \frac{4\pi\hbar\rho R^2}{q} j_1\left(\frac{qR}{\hbar}\right) \quad (5.6.6)$$

where  $j_1(x)$  is the spherical Bessel function of the first kind,  $\rho_p$  is the density of the particle, and  $R$  is the radius of the nano-sphere. From this, we can now derive the decoherence parameters,

$$\Gamma_{CSL} = A\lambda_c \int_0^\infty e^{-\alpha^2} j_1^2\left(\frac{\alpha R}{r_c}\right) d\alpha \quad (5.6.7a)$$

$$f_{CSL}(x) = \frac{A}{\Gamma_{CSL}} \lambda_c \frac{r_c}{x} \int_0^\infty e^{-\alpha^2} j_1^2\left(\frac{\alpha R}{r_c}\right) \text{Si}\left(\frac{\alpha x}{r_c}\right) \frac{d\alpha}{\alpha} \quad (5.6.7b)$$

where we have used the dimensionless pre-factor  $A = (36/\sqrt{\pi})(m/m_0)^2(r_c/R)^2$  and have used the integration variable  $\alpha = qr_c/\hbar$ . Both equations must be solved numerically, however, the value of  $r_c$  is very small leading to underflow issues. The value  $r_c/\hbar$  gives us more sensible values over which to integrate and avoids these underflow errors.

# Chapter 6

## Bayesian Inference

Most experiments that aim to put bounds on the values of the CSL parameters  $\theta = [\lambda_c, r_c]$  apply a binary approach to their exclusion zones [9, 126] applying a hard border between regions of the parameter space that are excluded and regions that are not excluded. This chapter begins with a brief overview of Bayesian inference in Sections 6.1 and 6.2. In the remainder of this chapter we provide a novel approach using the techniques of Bayesian inference to apply a value to the probability that each set of parameters is not excluded by the experimental data, and use this to produce a predictive model to estimate the necessary control parameters for a real experiment.

### 6.1 Introduction to Bayesian Inference

The basis of Bayesian inference is built on the use of Bayes' rule,

$$P(Y|X) = \frac{P(X|Y)P(Y)}{P(X)} \quad (6.1.1)$$

where  $Y$  is some hypothesis and  $X$  is some data relating to that hypothesis. The *posterior*  $P(Y|X)$  is the probability that the hypothesis  $Y$  is true given some data  $X$ .  $P(Y)$  is the probability that  $Y$  is true before we have collected any data and is called the *Prior*, and contains all the previous information we have collected about the hypothesis.  $P(X|Y)$  is the probability of measuring the data  $X$  given that the hypothesis  $Y$  is true, called the *Likelihood*. And the term

$P(X)$  is a normalisation constant describing the probability of measuring the data  $X$ . This normalisation term is often referred to as the *Evidence*. In certain problems, such as parameter estimation problems, it is often convenient to omit the evidence term, replacing the equality in Eq. (6.1.1) with a proportionality,  $P(Y|X) \propto P(X|Y)P(Y)$  [12].

We introduce the coin toss, which is a typical example for the use of Bayes' theorem, as an illustrative example. This will allow us to explore how we make use of Bayes' rule such that we can then apply it to our own problem of collapse parameter estimation. A coin toss is a Bernoulli process following the binomial distribution,

$$P(x|\theta) = \theta^x(1 - \theta)^{1-x} \quad (6.1.2)$$

where  $\theta$  is the probability that the coin will give heads on any any given throw, and  $x$  is the outcome of the given throw (either 1 for heads or 0 for tails). If we assume that all possible weightings,  $\theta$ , for a given coin are equally likely, we create the uniform prior,

$$P(\theta) = \begin{cases} 1, & \text{if } 0 \leq \theta \leq 1 \\ 0, & \text{otherwise} \end{cases} \quad (6.1.3)$$

this is a good method of including ignorance about the parameters we are estimating, but may not always be the best case. We will return to this idea of an unbiased prior later in section 6.2.

If we proceed to run the experiment, that is flip the coin and record the outcome,  $N$  times, such that we collect a set of data  $\mathbf{X} = [x_1, x_2, x_3, \dots, x_N]$ , we can find the posterior for this set of data. We start by finding the posterior for the first outcome as  $P(\theta|x_1) \propto \theta^{x_1}(1-\theta)^{1-x_1}$ . Note that we have omitted the evidence as this will not affect the estimated parameter and because we have bounded  $\theta$  to lie in the region  $0 \leq \theta \leq 1$ , we allow  $P(\theta) = 1$ . Recall that the prior contains all of our previous knowledge about the system, that means for our second outcome, our prior should contain what we have learned from the first measurement such that our prior now takes the form  $P(\theta) = P(\theta|x_1) = \theta^{x_1}(1 - \theta)^{1-x_1}$ , where we once again do not include normalisation. Therefore our new posterior will be  $P(\theta|x_1, x_2) = \theta^{x_2}(1 - \theta)^{1-x_2}\theta^{x_1}(1 - \theta)^{1-x_1}$ . We can repeat this process to find the

posterior for all measured outcomes to be

$$P(\theta|\mathbf{X}) \propto \prod_{i=1}^N P(x_i|\theta)P(\theta) \quad (6.1.4)$$

such that the likelihood of measuring all  $\mathbf{X}$  is given by  $P(\mathbf{X}|\theta) = \prod_{i=1}^N P(x_i|\theta)$ . An example of this Bayesian updating for a specific coin toss example with different priors is given in Fig. 6.1.

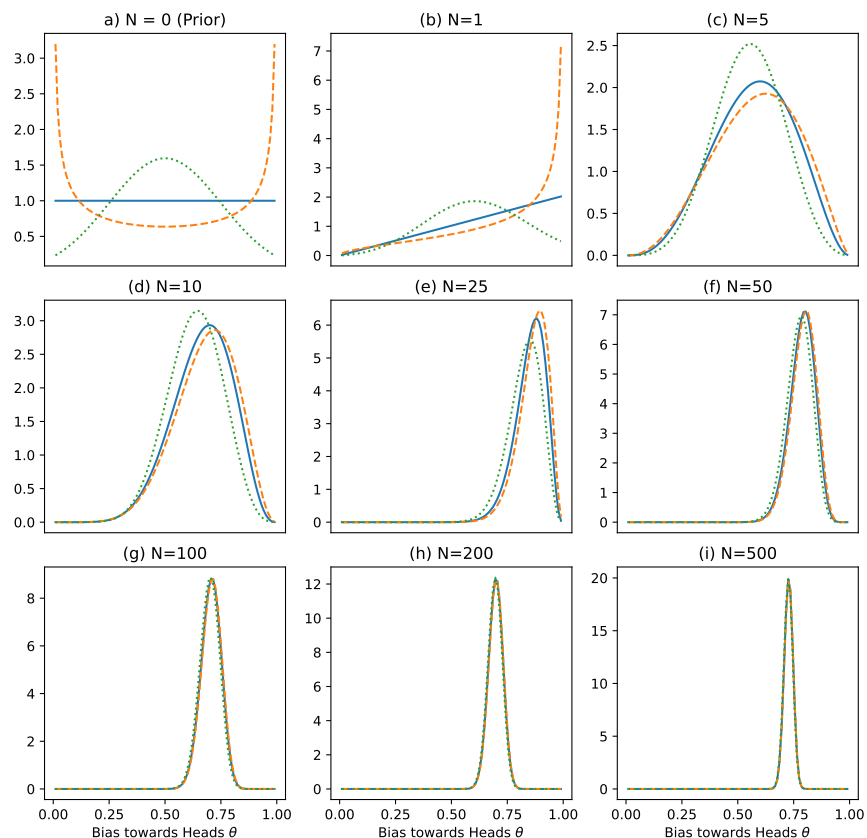


Figure 6.1: The results of  $N$  Bernoulli trials of tossing a coin weighted to give heads 70% of all tosses. The solid line is the result of using the uniform prior, while the dashed and dotted lines give the results of priors containing different assumptions about the coin.

Fig. 6.1 (a) gives the prior, i.e. our knowledge and assumptions before any measurements are taken. Three priors are shown in Fig. 6.1. The solid blue line

gives the uniform prior, the dashed orange line shows the Jeffreys' prior which is an uninformative prior based on the likelihood used in the experiment, and the dotted green line shows a Gaussian prior centred on 0.5 with a spread of  $\sigma = 0.25$ , i.e. an uncertain assumption that this is a fair coin. The following panels show the posteriors after  $N$  measurements for each prior. In panel (b) all the priors tend to 0 at  $\theta = 0$  as we have only measured a single value, a head. The only thing we can say with such a small sample is that the coin cannot be weighted such to always give tails. In panel (c) we have mostly measured heads, but have measured some tails. This allows us to say that it is impossible that the coin is weighted to only give heads. The data we have collected does suggest a bias towards heads which all the posteriors show to varying degrees. As we collect more data (panels (d) to (i)) the peaks of each posterior tend to the same value and their respective widths decrease. This suggests that the estimated  $\theta$  of all priors will tend to the same value given enough data. The outcome of only a few data points does not provide much information at all, therefore our understanding is heavily dominated by our prior expectations. However, after many data points, the posterior becomes dominated by the likelihood function, and so we are led to the same conclusion regardless of our prior beliefs. but we can see that *the choice of prior does affect how many test we must perform* to get a good estimate of  $\theta$ . The decrease in the peaks' widths suggest that we also become more sure of our estimate of  $\theta$ , the peak width corresponds to the uncertainty in our estimate. After around 100 runs (panels (g), (h), and (i)), we see that the estimate of  $\theta$  does not vary greatly, but our uncertainty of the value changes as  $\propto 1/\sqrt{N}$ .

### 6.1.1 The 2 Dimensional Case

In principle we are also able to expand our analysis to estimate the multivariate parameter  $\boldsymbol{\theta} = [\theta_1, \theta_2, \dots, \theta_N]$ . In the case of CSL, we have a 2 dimensional parameter  $\boldsymbol{\theta} = [r_c, \lambda_c]$ , so we shall limit our discussions here to a 2 dimensional example.

We can imagine a hypothetical system that leads to randomly distributed measurement data. For example, this could be the measured position of a particle in the 0th energy level of a 2-dimensional quantum harmonic oscillator. This

data is distributed via a Gaussian process in space about a position  $(x_0, y_0)$  that is unknown. This gives the likelihood of measuring a location  $(x, y)$  as,

$$p(x, y|x_0, y_0) \propto \exp \left[ -\frac{(x - x_0)^2}{2\sigma^2} - \frac{(y - y_0)^2}{2\sigma^2} \right] \quad (6.1.5)$$

where the value of  $\sigma$  is known. We assign a flat prior to the  $x_0, y_0$  parameter space. This flat prior is equivalent to the uniform prior discussed in the previous section and this choice of prior will be discussed in the next section. Then we measure the outcome of the process to estimate the parameters  $x_0$  and  $y_0$ .

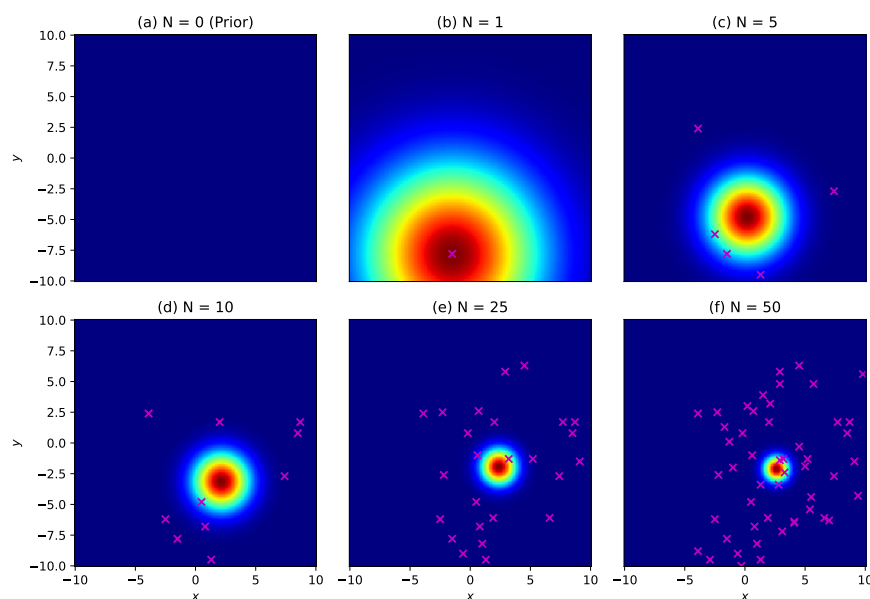


Figure 6.2: A flat prior and calculated posteriors after  $N$  measurements. The purple crosses indicate the measured data that leads to the given posterior.

Fig. 6.2 shows the data collected and the posteriors calculated for that data. As we collect more data, the peak in the posterior tends to a value of  $x_0 = 3$  and  $y_0 = -2$  which were the values used to generate the data. We also see that as  $N$  increases, the width of the peak decreases indicating that we are becoming more certain in our estimate of the unknown parameters.

## 6.2 Choice of Prior

As we have seen in Fig. 6.1 the choice we make for the prior has an impact on the final posterior for small numbers of data points. As a result we must choose the prior in the analysis of the results from the interferometry experiment carefully. We can choose either to base our prior on previous experimental results, or an uninformative prior that assumes no prior knowledge.

The first type, basing our prior on previous experimental results, is as simple as using the posterior from a previous experiment as our prior. If our coin toss example above ended after  $N = 10$ , we would not be sure exactly what the bias of the coin is, as the peak is very wide. However, using this posterior would mean we would approach the true value much quicker than if we started with a different prior. In the absence of such previous experiments, we must choose the prior carefully. While it may seem sensible to assign a constant probability density over the parameter space, this may not produce the most reliable results at small numbers of data points.

### 6.2.1 Uninformative Priors

We may also want to avoid injecting any bias into the Bayesian analysis of our results. This is achieved by the use of an uninformative prior. Uninformative priors are often useful when we want to maintain scientific objectivity and to better compare with other experiments [127, 128]. There are four main types of uninformative priors that we consider [128],

- Uniform Prior
- Jeffreys' Prior
- Reference Prior
- Maximal Data Information Prior (MDIP)

### 6.2.1.1 Uniform Prior

The uniform prior is the simplest of the priors and is found by setting the prior over the entire parameter space equal to a constant value. This is shown as the solid blue line in Fig. 6.1. In an experiment like the coin toss with a definite region of applicability, this prior is normalisable. However, if the region that the parameters of interest lie in is infinite, then the prior is not normalisable. For the case of CSL, we can make the claim that the probability of the parameters lying outside the region of parameter space we are interested in is 0. This allows us to normalise the prior within that region of parameter space.

### 6.2.1.2 Jeffreys' Prior

Proposed by Sir Harold Jeffreys, the Jeffreys' prior is designed to be invariant under reparametrisation of the model [129]. It is defined as  $P(\boldsymbol{\theta}) \propto \sqrt{\det(I(\boldsymbol{\theta}))}$  where

$$I_{i,j}(\boldsymbol{\theta}) = \int \left( \frac{\partial}{\partial \theta_i} \log p(x|\boldsymbol{\theta}) \frac{\partial}{\partial \theta_j} \log p(x|\boldsymbol{\theta}) \right) p(x|\boldsymbol{\theta}) dx \quad (6.2.1)$$

is the Fisher Information matrix. This is a measure of the sensitivity of the likelihood function to changes in  $\boldsymbol{\theta}$  [130]. Although the equations are given for multi-dimensional problems, Jeffreys' prior does not always cover these multi-dimensional problems well [127]. Therefore, care must be taken when choosing the prior for the types of problems such as parameter estimation in CSL.

### 6.2.1.3 Reference Prior

The reference prior is an attempt to modify the Jeffreys' prior by reducing the dependence amongst parameters. These dependencies are often introduced by Jeffreys' prior and can lead to poor performance or inconsistencies [128]. Introduced by Bernardo in 1979 [131] by maximising the expected Kulback-Liebler (KL) divergence, discussed below, to ensure the data has the maximal effect on the posterior.

To generate a reference prior, we maximise the discrepancy between the prior and the likelihood of a sufficient statistic  $t(\mathbf{X})$ . This is some quantity that, when evaluated from the sample of data, provides the same information about the



parameters as using the data directly. For an example of the sufficient statistic we can use the likelihood of the coin toss in Eq. (6.1.2) and recall the property  $P(\mathbf{X}|\theta) = \prod_{i=1}^n P(x_i|\theta)$ . In this case, for a set of measured outcomes  $\mathbf{X} = [x_1, x_2, \dots, x_N]$ , we have the total likelihood,

$$p(\mathbf{X}|\theta) \propto \theta^{\sum_{i=1}^N x_i} (1 - \theta)^{N - \sum_{i=1}^N x_i}. \quad (6.2.2)$$

From this, we can define the sufficient statistic as  $t(\mathbf{X}) = \sum_{i=1}^N x_i$ . Here we have used  $x_i \in (0, 1)$  where 0 represents tails and 1 represents heads as discussed in the coin toss example above.

To derive the reference prior we want to maximise the KL divergence [132],

$$\langle KL \rangle = \int \int p(\theta|t)p(t) \log \left[ \frac{p(\theta|t)}{p(\theta)} \right] d\theta dt. \quad (6.2.3)$$

And making use of the conditional probability rule  $p(\theta, t) = p(\theta|t)p(t)$  [12], we can find the mutual information between  $t$  and  $\theta$ , which is a measure of their dependence. We do this because we do not know the value of  $t(\mathbf{X})$  before we collect the data and this is akin to maximising the expected KL divergence,

$$M.I. = \int \int p(\theta, t) \log \left[ \frac{p(\theta, t)}{p(\theta)p(t)} \right] d\theta dt. \quad (6.2.4)$$

By maximising the mutual information, we maximise the dependence the variables  $\theta$  and  $t$  have on each other. As a result, this gives the data the maximum influence on the final posterior over the prior. This is a useful method for generating priors that can be extended to multi-parameter problems [132]. However, for these multi-parameter cases, it is often difficult to generate a reference prior due to the high dimensionality of the integrals used. There may also not be an obvious sufficient statistic that can be used making this prior not feasible for a given problem.

#### 6.2.1.4 Maximal Data Information Prior

The Maximal Data Information Prior (MDIP) is based on the likelihood function of the experiment [128],

$$p(\boldsymbol{\theta}) \propto \exp \left[ \int p(x|\boldsymbol{\theta}) \log p(x|\boldsymbol{\theta}) dx \right] \quad (6.2.5)$$

and is defined such that we maximise the average information contained in the likelihood relative to the prior. That is, the prior is chosen such that it maximises the function,

$$\iint p(x|\boldsymbol{\theta}) \log p(x|\boldsymbol{\theta}) dx p(\boldsymbol{\theta}) d\boldsymbol{\theta} + \int p(\boldsymbol{\theta}) \log p(\boldsymbol{\theta}) d\boldsymbol{\theta}. \quad (6.2.6)$$

Unlike the Jeffreys' prior, the MDIP is easily extendible to multi-parameter problems and maintains stability [133]. As a result, this makes the MDIP a more suitable choice of prior for the MAQRO experiment.

## 6.3 Simulations of the Interferometer

Using the theoretical model of the matter-wave interferometer derived in Chapter 5 we are able to build a simulation of the experiment. We can then apply Bayesian techniques to the simulated results to calculate the probability distribution we could achieve over the CSL parameter space in an actual experiment.

The key result of our theoretical model is equation (5.3.15) which describes the final interference pattern after the full propagation. In our simulations, we are only interested in the final observation point of the particle. Therefore, to model a particle traversing the interferometer we choose a random measurement location  $z$  weighted by the probability function  $w(z)$ . By running the simulation  $N$  times, and counting the number of times we measure a particle in the region  $z+\delta z$ , we reconstruct the interference pattern  $w(z)$ . Fig. 6.4 shows the theoretical likelihood of measuring a particle at some position  $z$  along with a histogram showing the number of times each  $z+\delta z$  bin measures a particle. The region  $z+\delta z$  appears naturally in the simulations due to the discrete nature of computational simulations, that is we must use a discrete  $z$ -axis. The size of the interval  $\delta z$  is controlled by the number of points we include on the  $z$ -axis. Using this set-up we can begin to collect data to predict the results of a given experiment.

### 6.3.1 Bayesian Analysis of Simulated results

We consider any collapse model that manifests as a decoherence term in the interferometer and is described by a set of unknown parameters  $\boldsymbol{\theta} = [\theta_1, \theta_2, \dots, \theta_N]$ .

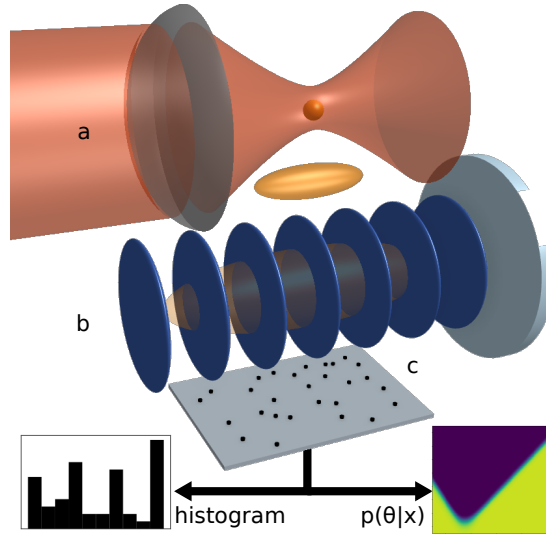


Figure 6.3: Illustration of the scenario considered showing a particle localised in a harmonic dipole trap as used in [91] (a) the wave function of which, when released, expands to cover several fringes of a standing wave grating (b) formed by retroreflection of a light pulse. The arrival location of particles is recorded (c) some time after the grating. In typical scenarios, the number of data points is small and taking a histogram of arrival positions (left) *may* be sufficient to evidence wave nature of the particle, the Bayesian inference approach makes fuller use of the available information and can hope to constrain free parameters in CSL.

We can then split the total decoherence in Eq. (5.3.18) into its component terms  $R_n = R_n^{\text{collapse}}(\boldsymbol{\theta})R_n^{\text{Env}}$  where  $R_n^{\text{collapse}}(\boldsymbol{\theta})$  is the decoherence caused by the collapse model, and  $R_n^{\text{Env}}$  is the effect of environmental decoherence sources. This gives us the joint probability  $p(z, \boldsymbol{\theta})$ . With this in mind, we are able to find the likelihood of measuring the particle at a location  $z$  after the interferometer as,

$$p(z|\boldsymbol{\theta}) = W(z) \frac{\beta m}{\int p(z, \boldsymbol{\theta}) dz} \left[ 1 + 2 \sum_{n=0}^{\infty} R_n^{\text{collapse}}(\boldsymbol{\theta}) R_n^{\text{Env}} A_n \cos(nkz) \right] \quad (6.3.1)$$

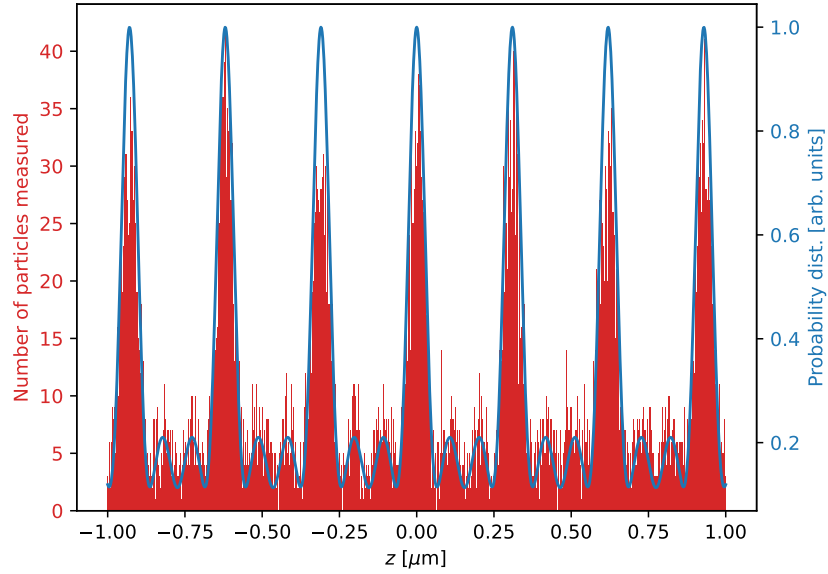


Figure 6.4: The probability distribution for a  $10^6\text{u}$  nano particle in a MAQRO-like experiment with control parameters  $\phi_0 = 4$  and  $t_2 = 1.6t_T$  which are given in Table 5.1. In blue is the result of equation (5.3.15) while the red histogram shows the number of times the particle is measured in the range  $z + \delta z$  after 10,000 experimental runs.

where we have simply rewritten Eq. (5.3.15). For brevity, we describe the pitch of the interference pattern with  $k = 2\pi/D$  and the Talbot terms with

$$A_n = B_n \left( \frac{ndt_2}{t_T D} \right) \exp \left[ -2 \left( \frac{n\pi\sigma_x t_2}{Dt_1} \right)^2 \right]. \quad (6.3.2)$$

We also include the multiplicative window  $W(z)$  that represents the limited spatial window over which we collect data. This limits the equation to a given spatial region  $S$  given by,

$$W(x) = \begin{cases} 1 & \text{if } x \in S \\ 0 & \text{if } x \notin S \end{cases} \quad (6.3.3)$$

Assuming independent and identically distributed position measurements, the joint probability of all  $N$  measurements  $\mathbf{Z} = (z_1, z_2, \dots, z_N)$  is  $p(\mathbf{Z}|\boldsymbol{\theta}) =$

$\prod_{i=1}^N p(z_i|\boldsymbol{\theta})$ . Thus the probability of a set of parameters  $\boldsymbol{\theta}$  is given by,

$$p(\boldsymbol{\theta}|\mathbf{Z}) \propto p(\mathbf{Z}|\boldsymbol{\theta})p(\boldsymbol{\theta}) \quad (6.3.4)$$

where we neglect the evidence as it has no bearing on  $\boldsymbol{\theta}$ .

The two parameter CSL model can be included by using Eq. (5.5.2) as the CSL decoherence term and setting  $\Gamma_i$  and  $f_i(x)$  to the relevant terms in Eq. (5.6.7). In principal, we can use any collapse model in this place, but due to the fact that CSL has been well studied, it is a useful theory to use to test our method.

We use the MDIP for our prior in this example. It is found by inserting Eq. (6.3.1) into Eq. (6.2.5). Then we can find the posterior  $p(\boldsymbol{\theta}|\mathbf{Z})$  after collecting data  $\mathbf{Z}$ . Initially, we distribute the data according to the conditional likelihood  $p(z_i|\boldsymbol{\theta} = 0)$ , i.e. the results we expect should there be no CSL effect. This has the benefit of maximising the extent of the regions on the parameter space that such an experiment could potentially exclude. Such posteriors are shown in Fig. 6.5.

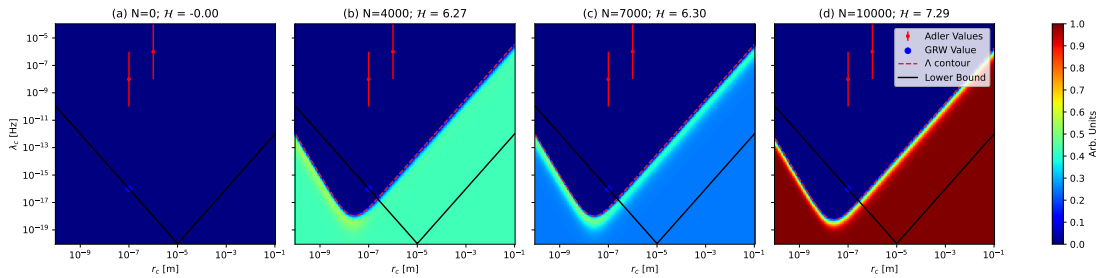


Figure 6.5: Probability distributions  $p(\boldsymbol{\theta}|\mathbf{Z})$  for the CSL model with MAQRO-like parameters, as detailed in the text, using the Maximal Data Information Prior, with  $N$  points picked from distribution  $p(z_i|\boldsymbol{\theta} = 0)$ . (a)  $N = 0$  is the prior; (b–d) are for  $N$  as indicated. The GRW value [83], Adler values [134], and lower bound, discussed in the text, are motivated by theoretical considerations. The red dashed upper bound is found such that 95% of the probability distribution is below this line.

### 6.3.2 Priors used to Estimate the CSL Parameters

As discussed in Sec. 6.2, the choice of prior used is critical to the outcome of the analysis of the collected data, especially in a MAQRO experiment where we

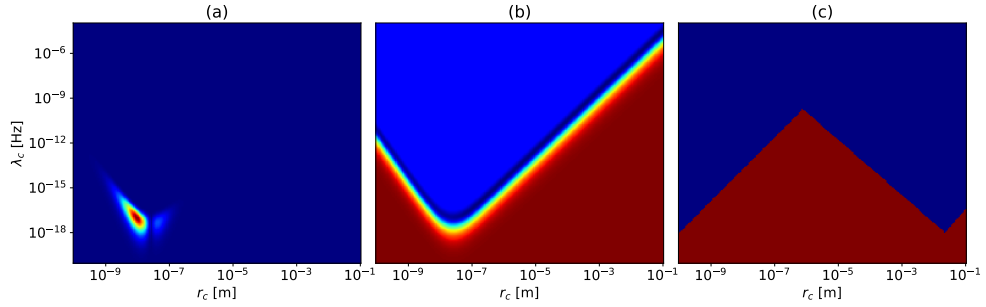


Figure 6.6: A set of possible priors to be used in the analysis of a matter-wave interferometry experiment using a silicon sphere with mass  $8u$ . (a) shows the Jeffreys’ prior, (b) is the MDIP, and (c) shows the experimental prior that sets all previously excluded values to a probability of 0.

are likely to have a small number of data points. The prior we choose could introduce unwanted assumptions affecting our final results, or if chosen well will lead to more informative posteriors or even reduce the number of measurements we need to take in order to exclude regions with sufficient confidence. Due to the numerical nature of our simulations, we must also consider a region over which our analysis can take place. This will introduce a region of parameter space  $\theta_S$  in which the prior follows the value of a given function, but outside of this region, the value of the prior will be 0,

$$p(\theta) = \begin{cases} f(\theta) & \text{if } \theta \in \theta_S \\ 0 & \text{if } \theta \notin \theta_S. \end{cases} \quad (6.3.5)$$

We must choose the region  $\theta_S$  such that we capture the information about the parameter values of interest. But we should avoid making this region too large as to avoid adding too much computational expense. We look to Fig. 5.1 as a guide. In this figure, we see an unshaded region that has not been ruled out by experiment or theory, so the chosen region must include this space. We also see a number of shaded regions relating to parts of the parameter space ruled out by various experiments. The purple region at the top shows the region that has been excluded by previous interferometry experiments, for comparison with these previous experiments, it is pertinent to set the maximum value of  $\lambda_c$  to  $10^{-4}\text{Hz}$

as well. We also note the theoretical lower bounds given by the grey line and shaded region. There is little need for the value of  $\lambda_c$  to go below  $10^{-20}\text{Hz}$  as these values are excluded by theory.

The bounds on  $r_c$  are chosen to cover the entire region that has not yet been experimentally, or theoretically, excluded. We choose to work in the region  $10^{-10} \leq r_c \leq 10^{-1}\text{m}$  as this also captures the regions excluded by various non-interferometric test that contain interesting features, such as the minimum in the blue region, for better comparison.

The first prior we consider is a uniform prior. In this case, we assume a constant prior in the region  $\theta_S$  and 0 elsewhere  $f(\theta) = \text{Const.}$ . On the surface this might seem like a sensible choice. However, as discussed in section 6.2, assuming that all possible parameters in a region are equally likely risks injecting a bias into our results, as this prior still contains an assumption. We aim to use a prior that contains as few assumptions as possible, preferably none. For this reason we initially look to the Jeffreys' prior.

In Jeffreys' prior we set  $f(\theta) = A\sqrt{\det[I(\theta)]}$  where  $A$  is a normalisation constant, and  $I(\theta)$  is the Fisher information matrix given in Eq. (6.2.1). It is invariant under reparametrisation, meaning that if we reparametrise  $\theta$  in our likelihood, we can perform the inverse change of variables on our posterior to recover our original parametrisation. It also follows from the Fisher information which measures how the likelihood changes with  $\theta$ . Therefore, the only assumptions that go into the prior are built into the experiment itself. This does have the issue that changing the experimental parameters, such as the particle's mass, will affect the prior making comparisons between experimental setups more difficult. The Jeffreys' prior does not always scale up to multidimensional problems effectively, often becoming unstable [127] which is a problem for our tests. We find that in the case of our experiments, this prior leads to poor posteriors, as was discussed in section 6.2.1.2. In this specific experiment, we also find that the Jeffreys' prior is sensitive to instabilities leading to unphysical posterior distributions.

When considering the reference prior, we must first start by defining a sufficient statistic  $t(\mathbf{Z})$ . This is already a difficult task due to the nature of the likelihood given in Eq. (6.3.1). The measured arrival locations are contained

within a Fourier sum. Along with the product function used to produce the likelihood of all measured arrival locations makes it such that there is no clear sufficient statistic to choose. We also must consider the computational complexity that would come with choosing this prior. We find the prior that maximises the mutual information between  $\boldsymbol{\theta}$  and  $\mathbf{Z}$ . This procedure is computationally expensive and would take a long time to run. This is especially an issue when we want to compare the results for multiple different scenarios, as a new prior must be found for each scenario.

We are left with the Maximal Information Data Prior (MDIP) as our best option. This prior is not only easy to implement to this experiment, it is also a good choice to maximise the information we gain from each data point. With ease we are able to find this prior numerically from the likelihood as,

$$f(\boldsymbol{\theta}) = A \exp \left[ \int p(z|\boldsymbol{\theta}) \log p(z|\boldsymbol{\theta}) dz \right], \quad (6.3.6)$$

where  $A$  is again a normalisation constant. This prior maximises the effect of each data point on the posterior quickly overwhelming the prior [133].

The final prior we consider is motivated by previous experimental results, which we call the “Experimental Prior”. This prior is defined as constant over all values of  $\boldsymbol{\theta}$  that have not been excluded by previous experiments, and zero to the values that have been excluded. The uncoloured region in Fig. 5.1 shows the regions of the parameter space that have, and have not been excluded by experiment.

## 6.4 Parametrisation by Information Gain

By considering the information gain, we make a more systematic use of all of the distribution with respect to previous methods that simply produced a histogram, like the one shown in Fig. 6.4. If we use the information gained from the experimental prior, we can use this to quantify how much we have learned about the CSL parameter space compared to previous exclusion plots. However, using other priors, such as the MDIP, considers the change of the full parameter space as we have collected data. This thus provides us with a robust method to compare similar experiments and optimise their control parameters.



A single valued macroscopicity constant has been suggested as a method to compare the results of various classicalisation experiments [135]. It considers any modification to the Von Neumann equation of the form,

$$\partial_t \rho = \frac{[\mathbf{H}, \rho]}{i\hbar} + \mathcal{L}\rho \quad (6.4.1)$$

where

$$\mathcal{L}\rho = \frac{1}{\tau} \left[ \int d^3s d^3q g(s, q) L(\mathbf{s}, \mathbf{q}) \rho L^\dagger(\mathbf{s}\mathbf{q}) - \rho \right] \quad (6.4.2)$$

and

$$L(\mathbf{s}, \mathbf{q}) = \exp \left[ \frac{i}{\hbar} (\mathbf{p} \cdot \mathbf{s} - \mathbf{q} \cdot \mathbf{x}) \right] \quad (6.4.3)$$

is a translation in position and momentum space. We also have the function  $g(s, q)$  which is a phase-space distribution with position and momentum standard deviations  $\sigma_s$  and  $\sigma_q$ . The effective coherence time is defined as  $\tau = \tau_e (m_e/m)^2$ , where  $\tau_e$  and  $m_e$  are a reference time-scale and reference mass respectively. For a given set of  $\sigma_s$  and  $\sigma_q$  we can perform an experiment to rule out various time parameters  $\tau_e$ . We then define the macroscopicity as,

$$\mu_m = \log_{10} \left( \frac{\tau_m}{1\text{s}} \right) \quad (6.4.4)$$

where  $\tau_m$  is the maximum value of  $\tau_e$  that has been excluded.

However, this method still contains a number of issues. Firstly, the value of  $\mu$  can only rank superposition experiments. Therefore, we cannot use this metric to quantify the benefit of non-interferometric experiments, such as anomalous heating experiments [136]. This metric is also based on the coherence time scale  $\tau$  not the decoherence rate  $\lambda_C$  that our models are built around. In order to use this metric, we must reparametrise our models. This limits our choice of prior to one that is invariant under reparametrisation, such as the Jeffreys' prior, which has issues previously discussed.

We can solve these issues by using a more general metric, such as information as defined by Shannon [13]. We can quantify the amount of information in a posterior relative to the prior by [12],

$$\mathcal{H}(\mathbf{Z}) = \int p(\boldsymbol{\theta}|\mathbf{Z}) \log_2 \left[ \frac{p(\boldsymbol{\theta}|\mathbf{Z})}{p(\boldsymbol{\theta})} \right] d\boldsymbol{\theta} \quad (6.4.5)$$

where the use of  $\log_2$  ensures that the units of  $\mathcal{H}$  is bits. For reference, we include the value of  $\mathcal{H}$  in each posterior in Fig. 6.5.

The use of an information based approach to quantifying the outcome of tests of collapse models allows for easier comparison between experiments. Using the *expected information gain* we can effectively compare the results of experimental realisations with different sets of control parameters.

### 6.4.1 Expected Information Gain

We can predict the information gain that we expect from an experiment before any data is collected. This then allows us to predict how useful an experiment will be, and thus optimise the experimental parameters. The expression for this *expected information gain* is the information weighted by the evidence, integrated over all possible data realisations, [12],

$$\langle \mathcal{H} \rangle = \int \mathcal{H}(\mathbf{Z}) p(\mathbf{Z}) d\mathbf{Z}. \quad (6.4.6)$$

Due to the large number of dimensions in  $\mathbf{Z}$ , this integral is very costly to integrate numerically. For this reason we use a Monte-Carlo estimation of the integral. The first point to be solved is how to pick the data  $\mathbf{Z}$ . A traditional Monte-Carlo estimation would approximate the integral  $\int f(x)p(x)dx$  by the sum  $\sum_{i=1}^N f(x_i)$  where the values  $x_i$  are distributed according to the function  $p(x)$ . It may seem sensible to approximate the expected information by  $\sum_{i=1}^N \mathcal{H}(\mathbf{Z}_i)$  where each set of measured points  $\mathbf{Z}_i = [z_i^{(1)}, z_i^{(2)}, \dots, z_i^{(M)}]$  where each  $z_i^{(m)}$  are chosen from the evidence  $p(z)$ . This is only a valid method of point-picking should  $p(\mathbf{Z}) = \prod_i p(z_i)$  be true. The evidence of a single data point is,

$$p(z_i) = \int p(z|\boldsymbol{\theta}) p(\boldsymbol{\theta}) d\boldsymbol{\theta}. \quad (6.4.7)$$

However, if we record multiple data points, the evidence of this is,

$$\begin{aligned} p(\mathbf{Z}) &= \int p(\mathbf{Z}|\boldsymbol{\theta}) p(\boldsymbol{\theta}) d\boldsymbol{\theta} \\ &= \int \left[ \prod_i p(z_i|\boldsymbol{\theta}) \right] p(\boldsymbol{\theta}) d\boldsymbol{\theta}. \end{aligned} \quad (6.4.8)$$

The product of Eq. (6.4.7) is not the same as Eq. (6.4.8). Therefore, this is not an acceptable method of point-picking.

Instead, we make use of Markov Chain Monte-Carlo (MCMC) techniques to estimate the equation [137,138]. Inserting Eqs. (6.1.1) and (6.4.5) into Eq. (6.4.6) we can rewrite the expected information as,

$$\langle \mathcal{H} \rangle = \int \int p(\mathbf{Z}|\boldsymbol{\theta})p(\boldsymbol{\theta}) \log_2 \left[ \frac{p(\mathbf{Z}|\boldsymbol{\theta})}{p(\mathbf{Z})} \right] d\boldsymbol{\theta}d\mathbf{Z} \quad (6.4.9a)$$

$$= \int \int \{\log_2[p(\mathbf{Z}|\boldsymbol{\theta})] - \log_2[p(\mathbf{Z})]\}p(\mathbf{Z}|\boldsymbol{\theta})p(\boldsymbol{\theta})d\boldsymbol{\theta}d\mathbf{Z} \quad (6.4.9b)$$

$$\approx \frac{1}{M} \sum_{i=0}^M \{\log_2[p(\mathbf{Z}^{(i)}|\boldsymbol{\theta}^{(i)})] - \log_2[p(\mathbf{Z}^{(i)})]\} \quad (6.4.9c)$$

where  $M$  is the number of runs to be performed, and the values of  $\boldsymbol{\theta}^{(i)}$  are distributed according to the prior  $p(\boldsymbol{\theta})$ , and the values of  $\mathbf{Z}^{(i)}$  are distributed according to the conditional likelihood  $p(\mathbf{Z}|\boldsymbol{\theta} = \boldsymbol{\theta}^{(i)})$ . In general, the value for  $p(\mathbf{Z}^{(i)})$  is found by a second Monte-Carlo integration, but because our parameter  $\boldsymbol{\theta}$  has only two dimensions, it is more practical to perform the numerical integration than to directly calculate this quantity.

## 6.4.2 Expected Information with no Collapse

Another useful metric is the information we would expect to see should there be no collapse effect. We can estimate this simply by calculating Eq. (6.4.5) with the value of  $\mathbf{Z}$  distributed about  $p(\mathbf{Z}|\boldsymbol{\theta} = 0)$ . Running this  $M$  times and taking the average helps to smooth out numerical fluctuations due to the random nature of the measured  $z_i$  locations. By assuming no CSL effect the results of the simulation will lead to the lowest bounds on the parameters possible under the given experimental conditions. we denote this value as  $\langle \mathcal{H} \rangle_{\boldsymbol{\theta}=0}$ .

Using the metric of expected information, we can make predictions about the optimum experimental set-up. The use of Bayesian analysis and the information metric at  $\boldsymbol{\theta} = 0$  allows us to clearly estimate the number of measurements that would be needed to put the lowest possible bounds on the CSL parameters in a given experiment. In Fig. 6.7, we see that for both priors there is a rapid gain in information below 2000 data points. After this, we gain much less information per

each new data point from the experimentally motivated prior (in blue). However, the information we gain from the MDIP is much greater and continues to grow more rapidly for each new data point. Despite this, we find that by the 10,000th data point, for both priors the information gain per new data point is relatively small, so this is a sensible point to end taking new measurements.

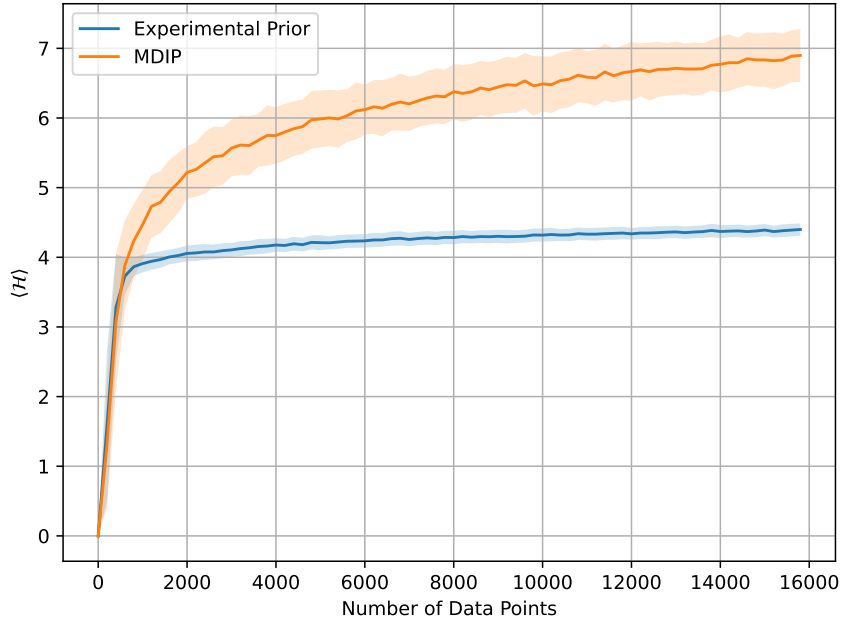


Figure 6.7: Expected information  $\langle \mathcal{H} \rangle_{\theta=0}$ , under the assumption that there is no CSL effect, as a function of the number of measurements for an experiment using a spherical particle of mass  $10^8 \text{u}$  with parameters given in Table 5.1 and  $\phi_0 = 0.917$  and free-evolution time  $t_2 = 1.177t_T$ . The blue line gives the information gained with respect to a prior based on previous experimental results, and the orange line is the information gained from the MDIP.

We can also use the same method to estimate the best mass of particle to use. In a MAQRO like experiment, it would be easier to load the space-craft with a set of particles of roughly equal mass. For this reason, it is pertinent to predict the most effective mass to use. Fig. 6.8 shows the information gain as a function of particle mass for both the MDIP (orange) and the prior motivated by experimental results (blue). This is shown with no assumptions about the true

parameters of CSL using Eq. (6.4.9c) in panel (a), and under the assumption that there is no CSL effect in panel (b).

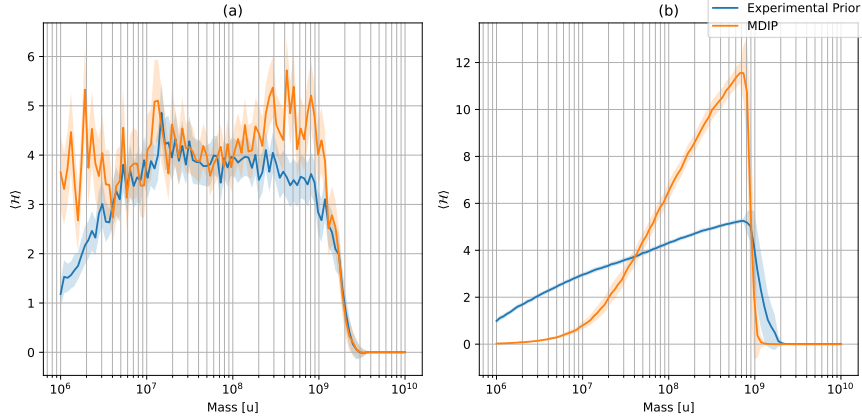


Figure 6.8: Expected information gain after 10,000 measurements when starting from the MDIP (orange line) and the experimental prior (blue line) with parameters given in Table 5.1 and  $\phi_0 = 0.917$  and free-evolution time  $t_2 = 1.177t_T$ . (a) shows the expected information with no assumptions about the true value of the CSL parameters  $\langle \mathcal{H} \rangle$ , while (b) shows the expected information assuming that there is no CSL effect in reality,  $\langle \mathcal{H} \rangle_{\theta=0}$ .

These figures show that the choice in our prior is critical to the amount of information we gain. This is because the information contained in the prior from Eq. (6.4.5) is always relative to the prior that the posterior is generated from. Thus, even when two equal posteriors are generated from different priors, their information gain will be different. It is perhaps unsurprising to find the MDIP often leads to more information gain than the experimental prior. This is because the MDIP is designed to maximise the KL divergence, and thus the information gain. Comparison between experiments is best performed by using the experimental prior. This will tell us how much information we have gained about the parameter space compared to what we have already learned. By then updating the experimental prior with the previous posterior, we can continue to quantify our information gain.

In Fig. 6.8 (a) we see that we would not expect to see any gain in the information relative to the MDIP until sufficiently large masses  $10^8 u$ . This information

peaks around  $10^9\text{u}$  where the information gain falls off rapidly. We note that at the masses at which the information falls to 0 corresponds to masses of particles with diameters close to the grating period. At this point, the effect of the grating is averaged out over the particle meaning we need a larger fluence to achieve the same phase shift. However, increasing the fluence also increases the scattering and absorption of grating photons leading to higher decoherence. To account for this, and thus use higher mass particles, we will consider particles with different geometries in Chapter 7. We also see that the information gained increases steadily when we use the experimental prior until it begins to fall off reaching 0 at the same mass as predicted from the MDIP. This suggests that we should aim to use masses around  $10^9\text{u}$  and the MDIP as our chosen prior to maximise the amount of information we can obtain from our experiments.

We can also compare this with Fig. 6.8 (b) plotting the information we could expect to learn should no CSL effect be measurable. This graph shows an increase in information with increasing particle mass, peaking at around  $10^9\text{u}$ . After this mass, the information gained relative to both priors falls off rapidly as it does in Fig. 6.8 (a). We also note that we gain significantly more information starting with the MDIP than we do starting with the experimental prior. This is as we expect. The MDIP is designed to contain minimum information, and thus maximise the information gained from each data point. The experimental prior on the other hand, contains information gained from previous experiments, and thus provides a limit to the amount of information we can gain.

### 6.4.3 Parametrisation by Decoherence rate $\lambda_c$

The information gain is a useful way to measure how much of the parameter space of a collapse model is ruled out by experiment and parametrise this by a single value. Previous works have achieved this by using the value of  $\lambda_c$  at a specific value of  $r_c$ , usually  $10^{-7}\text{m}$ . Fig. 6.9 shows how the upper bound we assign from the posterior, found under the assumption that there is no measurable CSL effect, changes with the mass of the particle starting with either the MDIP or the experimental prior. For a given posterior we can plot the upper bound as the line that splits the parameter space such that the integral of the probability

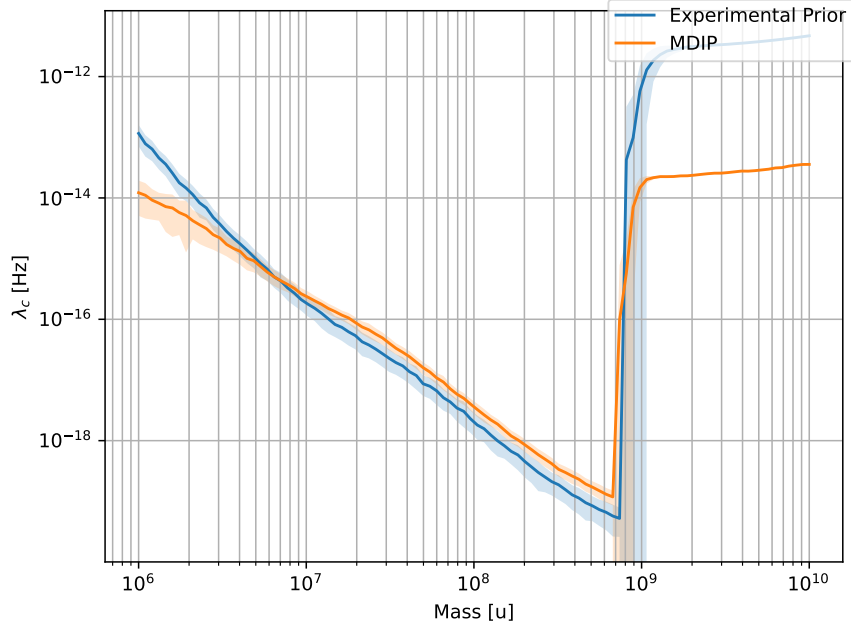


Figure 6.9: The height of the upper bound of  $\lambda_c$  at  $r_c = 10^{-7}\text{m}$  that we plot with 95% confidence under the assumption that there is no measurable CSL effect. The blue line shows the value we obtain starting from the experimental prior and the orange line show the value we obtain starting with the MDIP.

distribution below it is 95% of the integral over all of the parameter space. This line defines a curve in the  $\lambda_c, r_c$  parameter space is defined by the parameter  $\Lambda$  which we call the decoherence strength. It is used to govern the strength of a generic decoherence mechanism via,

$$R_n^{\text{deco}} = \exp \left[ -\frac{\Lambda(t_1 + t_2)(n\kappa d)^2}{2} \right] \quad (6.4.10)$$

where  $\kappa = \frac{t_1 t_2}{(t_1 + t_2)t_T}$  [106]. By setting  $n = 1$ , we can easily compare Eq. (6.4.10) to the decoherence from CSL Eq. (5.6.1). By equating the two functions,  $R_1^{\text{Collapse}}(\boldsymbol{\theta}) = R_1^{\text{deco}}$ , and some simple algebra, we can define a function,  $\lambda_c(\Lambda, r_c)$  which can be plotted over our posteriors,

$$\lambda_c = \frac{-\Lambda(\kappa d)^2}{C \int \exp[-\alpha^2] j_1(\alpha R/r_c) d\alpha (f(x) - 1)} \quad (6.4.11)$$

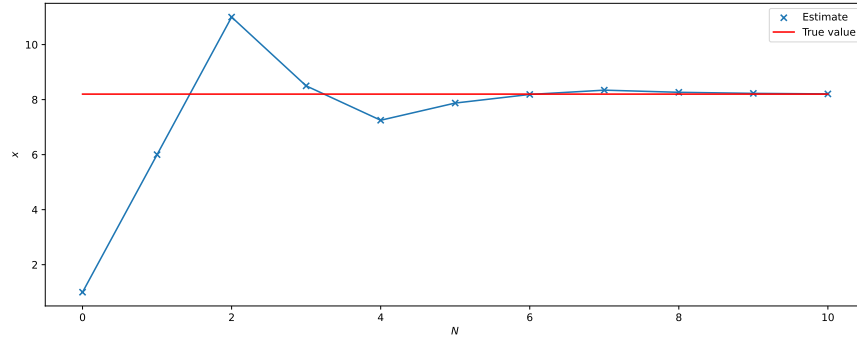


Figure 6.10: A representation of an iterative bisection algorithm attempting to find the true value of some parameter  $x$ . We start at  $N = 0$  with an initial guess of  $x_0 = 1$ . We find this is lower than the true value  $x_{\text{true}} = 8.2$  so we add 5 such that  $x_1 = 6$ . This is repeated until  $N = 2$  where  $x_2 > x_{\text{true}}$ . At this stage we know the value of  $x_{\text{true}}$  must be between  $x_1$  and  $x_2$  so we set these as the lower  $x_l$  and upper  $x_u$  bounds respectively. The next value is chosen between these values  $x_n = (x_l + x_u)/2$  until  $x_n$  converges on  $x_{\text{true}}$ . At each step we update the bounds such that if  $x_n > x_{\text{true}}$ , we set  $x_u = x_n$  and if  $x_n < x_{\text{true}}$  we set  $x_l = x_n$ .

where  $C = 36\sqrt{2/\pi}(M/m_0)^2(r_c/R)^2$ . In our simulations this line is found via an iterative bisection algorithm. This will increase or decrease the value of  $\Lambda$  until the integral  $\int_{\theta < \text{line}} p(\theta|\mathbf{Z})d\theta$  has passed 95% of the integral over the full parameter space. Then we choose values between the highest and lowest values of  $\Lambda$  until the integral is approximately 95% of the total. This is shown visually in Fig. 6.10

This gives us the upper bound that is shown as the dashed orange line in Fig. 6.5. To find the value for  $\lambda_c$  plotted in Fig. 6.9, we simply read off the value off the upper bound line at the point where  $r_c = 10^{-7}\text{m}$

Comparing Figs. 6.8 (b) and 6.9, we can see how the value of  $\lambda_c$  changes with the information gain. We see that as the information increases, the value of  $\lambda_c$  decreases. This is as we expect, as the value of  $\langle \mathcal{H} \rangle$  is a measure of how the posterior changes from the prior, and as the posterior deviates from the prior, we gain confidence in the bounds of the CSL parameters, and can thus put them lower.



## 6.5 Choosing the Control Parameters

In table 5.1, we do not give specific values for the phase parameter  $\phi_0$  or the second free-fall time  $t_2$ . These are two of the easiest parameters to control in the experiment. To change the phase, we need only change the power to the grating laser as the phase parameter is proportional to the energy in the laser as seen in Eq. 5.4.34. The free-evolution time is also easily altered because, in a space-based experiment such as MAQRO, the particle is at rest with respect to the apparatus, so we only need to change the time we wait between pulsing the grating laser and measuring the particle location.

Therefore, we should aim to choose values that will maximise the efficiency of the experiment. We begin by defining a vector of the control parameters we are interested in optimising as  $\mathbf{C} = [\phi_0, t_2]$ . For every new experimental scenario we wish to test, such as different particle mass or environmental parameters, we must optimise the parameters  $\mathbf{C}$ . We consider two main approaches, an information based approach, and a visibility based approach.

### 6.5.1 Choosing Parameters to Maximise Information Gain

We can use an information based approach to parametrise the results of our experiments. We aim to maximise the information gained from a hypothetical experiment performed with a given set of control parameters  $\mathbf{C}$  via a gradient ascent. This is performed by choosing a starting point in the parameter space,  $\mathbf{C}_0$  and evaluating the expected information gained by performing the experiment  $\langle \mathcal{H} \rangle(\mathbf{C}_0)$ . We then evaluate the same process taken at four points around the initial position in the parameter space. This is achieved by adding a value  $\pm \delta \phi_0$  to the position in the  $\phi_0$  axis or  $\pm \delta t_2$  to the value in the  $t_2$  axis to find the four values around our initial position. Then after evaluating to find the expected information gain at each of these new locations, we pick the location with the highest value as our new initial guess. This process is repeated, forming a path in the parameter space, until the expected information of our ‘initial guess’  $\langle \mathcal{H} \rangle(\mathbf{C}_0)$  is larger than any of the values surrounding it. At this point we assume that we have reached a maximum in the information gain and therefore, the optimum

parameters.

There still remains some issues with this approach. We must optimise the values  $\delta\phi_0$  and  $\delta t_2$  to ensure that the algorithm converges at a sensible rate and towards an accurate value. This method is also not guaranteed to converge on the true optimum set of parameters as local maxima can trick the algorithm into thinking it has reached the optimum value. See Fig. 6.11 for a one dimensional representation of this.

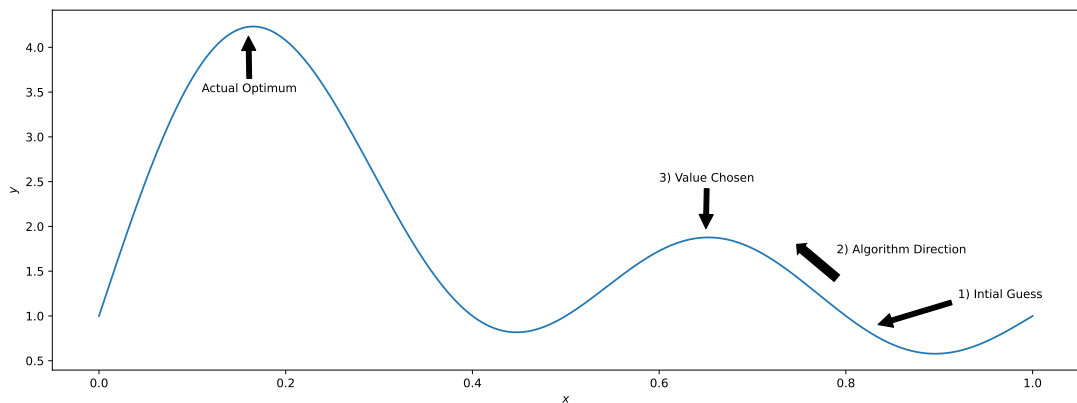


Figure 6.11: A simple 1D example of a gradient ascent algorithm. 1) We choose an initial value of  $x$  as  $x_0$ . 2) The algorithm changes the value of  $x_0$  moving up the peak. 3) The algorithm sees that the value of the function either side of the current  $x_0$  is less than at the current  $x_0$  so returns this value of  $x_0$ . However, this is only a local maximum, the global maximum is found at  $x \approx 1.65$ .

An easy solution to this is to raster over the whole parameter space and find the information gained for an experiment with every possible set of parameters  $\mathcal{C}$ . In order to make this computable, we must put bounds on the parameter space. The lower bounds on the  $\phi_0$  axis is simple, we must get as close to 0 as possible. We cannot set the lower bound to 0 as this corresponds to a laser power of 0, i.e. the laser is off. In this case there is no grating, and thus no interference pattern to observe. We set the bounds on  $\phi_0$  to be  $0.1 \leq \phi_0 \leq 4\pi$ . This value is chosen as the peak in the visibility of the final interference pattern is entirely in this range for all masses that we are considering here. For small free-evolution times, we recover the classical grating effect on the particle, which can be found by

using the small angle approximation  $\sin(x) = x$  on the coherent Talbot coefficients Eq. (5.4.1) to get  $B_n = J_n(\phi_0\pi\xi)$ . Longer free-evolution time scales also have the effect of increasing the amount of decoherence from environmental sources. Therefore, we stick to the regime of  $t_2 \approx t_T$  and set the range to  $0.5t_T \leq t_2 \leq 1.5t_T$  which is suggested in the supplementary to [11]. Using this we can plot the information gained from an experiment as a function of the control parameters  $\mathcal{H}(\mathbf{C})$ . When we have this data, we can easily find the optimum parameters by choosing the coordinates of the parameter space that leads to a maximum in  $\langle \mathcal{H} \rangle(\mathbf{C})$ .

This approach also requires a trade off between the accuracy of the outcome and the speed that it takes. The calculation of  $\langle \mathcal{H} \rangle(\mathbf{C})$  is computationally expensive, so it is more efficient to calculate the value at as few points in the  $\mathbf{C}$  space as possible. However, if the grid we use to represent the  $\mathbf{C}$  space is too coarse, we may lose important details, such as the global maximum. In order to ensure sufficient precision in the  $\mathbf{C}$  space, we must accept a long computation time. This becomes an issue when we want to compare the results between various experimental scenarios.

The issue of this approach taking a long time to run still exists. In order to solve this problem, we can run the optimisation function for various masses in the range we want to explore and find the optimum parameters for each mass. This will give us two sets of data that can be plotted for the optimum  $\phi_0$  and  $t_2$  with respect to the particle's mass. The sets of optimum parameters as functions of the particle mass are then saved and accessed when we want to find the optimum parameters for any mass. To find the optimum values between points that we have found we use an interpolation function. This is a function that allows us to estimate the value of a function between two points of data we have collected. We achieve interpolation via the `scipy interpolate library`. As a result, we can estimate the optimum parameters for any particle mass, as long as the rest of the experimental parameters match the values given in table 5.1. Although this seems like a sensible method to use, the interpolation function does not take into account any of the physics of the system. As a result it is likely to give us values that are not physically meaningful, such as negative phase and free-evolution

times.

In principle, these parameters are easy to modify even between experimental runs. As a result it is possible to maximise the information gained from the  $N$ th data point by maximising the expected information gain for one data point where the prior contains all of the previously collected data  $\langle \mathcal{H} \rangle(z_N | \mathbf{C}, z_1, z_2, \dots, z_{N-1})$  via one of the methods previously mentioned. This will take a significantly long time to calculate greatly increasing the amount of time needed between measurements. This may be a practical method should the lifetime of the experiment not be a limiting factor. However, should the experiment need to be completed in a short amount of time, it would be more practical to maximise the expected information gain for all measured locations as this will only need to be calculated once.

In this section we have discussed three methods to optimise the control parameters in our experiment. We have discussed a gradient ascent algorithm, rasterising the expected information over the whole parameter space, and attempting to maximise the information based on all previous data points. Using a gradient ascent requires us to optimise the parameters controlling the distance between each step to ensure speed and accuracy. This method also has an issue with finding only local maxima as opposed to the true maximum. To account for this, we considered finding the information for the full parameter space to find a global maximum. Calculating the expected information is computationally expensive and slow. This means that finding the information for every point in the multi-dimensional parameter space  $\mathbf{C}$  may be prohibitively time consuming. These issues also exist when finding the optimum parameters for each experimental run. If we use the gradient ascent, we risk finding local maxima, and if we raster over the full space  $\mathbf{C}$  this will take excessively long time scales made worse by having to repeat this every run. A significantly faster approach is to use the change in the visibility of the interference pattern as a result of the CSL decoherence to motivate our choice of the parameters.

### 6.5.2 Choosing Parameters to Maximise the Change in Visibility

The aim of an interferometry experiment is to observe the effect of CSL on the interference pattern of a matter-wave made by a massive particle. Therefore it is sensible to choose the parameters such that this effect is maximised. In previous works [11], the values have been chosen simply to maximise the sinusoidal visibility,

$$\nu_{\text{sin}}(\mathbf{C}) = \frac{2m}{\sqrt{2\pi}\sigma_p(t_1 + t_2)} \left| B_1 \left( \frac{t_2 d}{t_T D}, \mathbf{C} \right) \right| \exp \left[ -2 \left( \frac{\pi \sigma_z t_2}{t_1 D} \right)^2 \right]. \quad (6.5.1)$$

This assumes that maximising the visibility of the pattern maximises the potential reduction from CSL. However, we aim to maximise this quantity directly. We can define the CSL reduced visibility as,

$$\nu_{\text{red}}(\mathbf{C}) = \nu_{\text{sin}}(\mathbf{C}) R_1^{\text{collapse}}(\boldsymbol{\theta}, \mathbf{C}). \quad (6.5.2)$$

The optimum parameters are then found by maximising the equation  $\nu_{\text{sin}}(\mathbf{C}) - \nu_{\text{red}}(\mathbf{C})$ .

It is possible to use a similar gradient accent algorithm as discussed for the expected information based approach in Sec. 6.5.1. Using this method has many of the same issues as discussed in that section. We must optimise the parameters  $\delta\phi_0$  and  $\delta t_2$  to ensure accurate and fast results. But we still have the issue that we may sit on a local maximum and not a global maximum.

Due to the fact that calculating the values of both  $\nu_{\text{sin}}$  and  $R_1^{\text{collapse}}$  do not take a significantly long time, it is practical to raster a grid over the full  $\mathbf{C}$  space and find the value of  $\nu_{\text{sin}}(\mathbf{C}) - \nu_{\text{red}}(\mathbf{C})$  for each point in the parameter space to find the maximum. Although this still takes a large fraction of the total computation time for each simulated experimental scenario, it is faster than the information based approaches and is likely to provide more accurate results than the gradient accent version.

The optimum values for various masses of particles using the MAQRO-like parameters are given in Fig. 6.12. The graph shows that as the mass of the particle increases, the optimum values for both  $\phi_0$  and  $t_2$  decrease until they

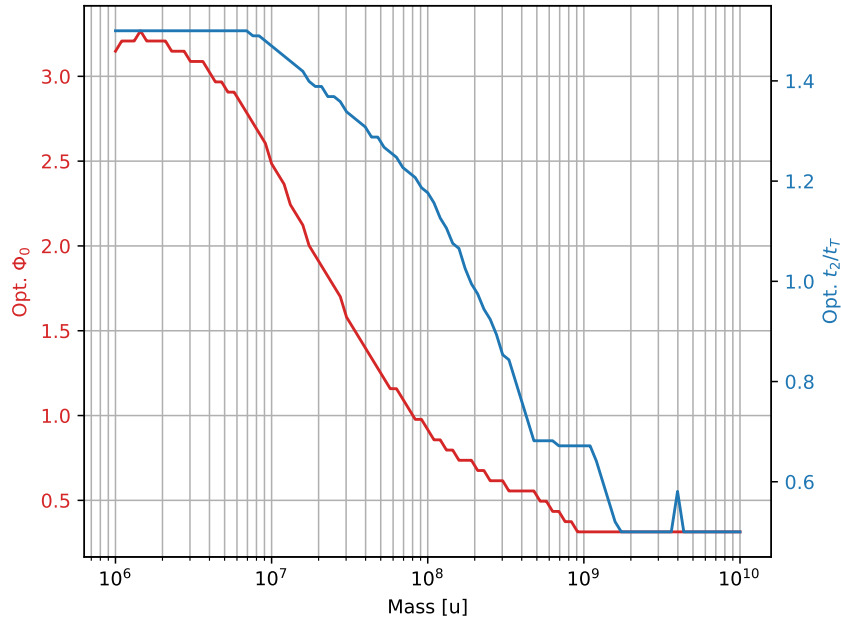


Figure 6.12: Optimum values of  $\phi_0$  and  $t_2$  for various nanosphere masses.

reach the lowest allowed values. This is a result of various decoherence mechanisms becoming more prominent as the particle mass increases. As the radius of the nanosphere increases, the scattering and absorption decoherence mechanisms within the grating beam become larger as shown in Eqs. (5.4.41) and (5.4.46), and so lower beam energies are required to prevent decoherence. The value of the free-evolution time  $t_2$  also reduces to reduce the effect of the matter-wave extending further in space and washing out the interference pattern.

## 6.6 Scenario Comparisons

The expected information metric introduced in Sec. 6.4.1 facilitates the comparison with different experiments and scenarios. For these comparisons we focus on the maximum information we could expect to get from the scenario. That is, the information we would expect to see if there was no CSL effect after 10,000 measurements, which is the point at which the information gain per data point has mostly levelled off as seen in Fig. 6.7.

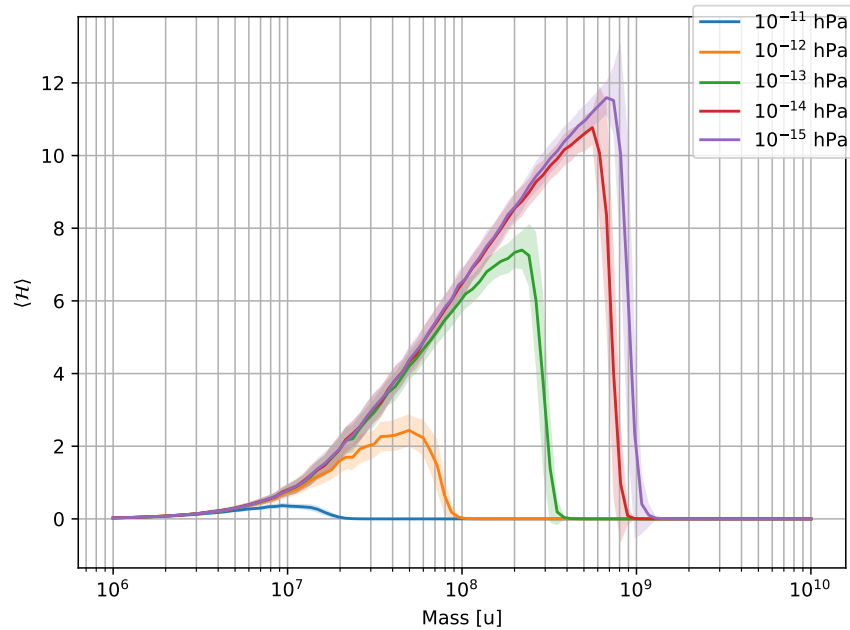


Figure 6.13: The expected information gain under the assumption that there is no CSL effect for various residual gas pressures as a function of particle mass.

We first compare the effect of different residual gas pressures as this is one of the key benefits of the space-based nature of experiments like MAQRO shown in Fig. 6.13.

We clearly see that minimising the gas pressure leads to a gain in the maximum obtainable information, and the maximum particle mass that can be used. This is true even when using the MDIP, which is based on the experimental scenario, as our prior and so will change as the parameters change. We also note that there reaches a point where the information can no longer increase. At this point, there is some other mechanism preventing the formation of the interference fringes. We also see that there is little improvement in reducing the pressure from  $10^{-14}$  hPa to  $10^{-15}$  hPa. Pressures this low are very difficult to achieve in practice. Previous work proposing parameters at which MAQRO will work often give more conservative estimates for the needed pressure [106]. However, with the detailed argument given here, we can argue that lower pressures are advantageous.

The second key parameter to control in a MAQRO-like mission is the space

craft drift. For all simulations we have performed, we have included an extra decoherence parameter to represent the position resolution for the final measurement of the particle,

$$R_n^{\text{Resolution}} = \exp \left[ -\frac{n(2\pi)^2}{2(D\sigma_m)^2} \right], \quad (6.6.1)$$

where  $\sigma_m$  (given in Table 5.1) is the position uncertainty that the initial state is prepared to, plus a constant rate of increase due to the spacecraft drift, which is informed by technical specifications such as [114]. As with the residual gas pressure scenarios, we can change the rate of increase in  $\sigma_m$  to see how that changes the information we can obtain from an experiment. Fig. 6.14, we change the length of this increase and observe the effects on the information gain for various particle masses.

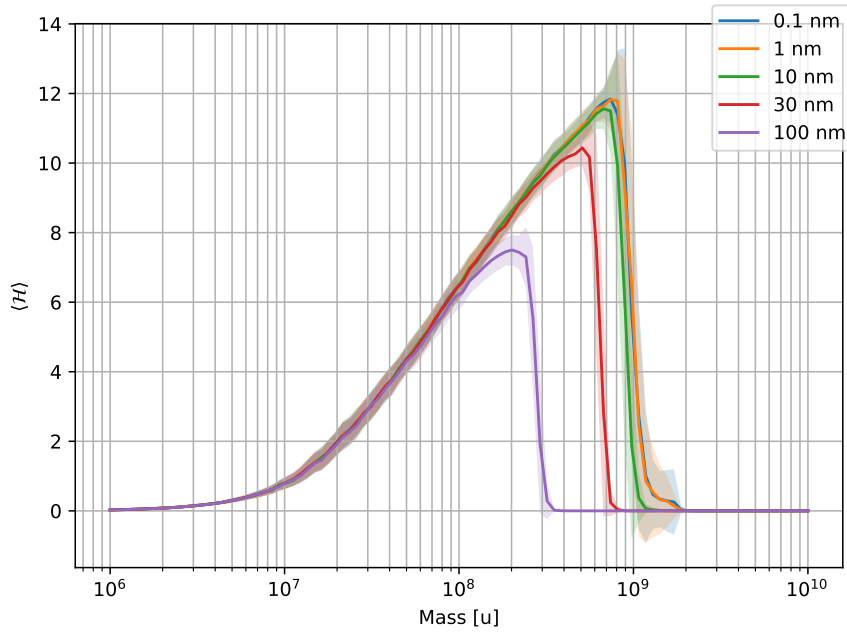


Figure 6.14: Total information gain after  $N = 10000$  data points under the assumption that there is no measurable CSL effect for various increase in measurement uncertainty as a result of space craft drift. Each plot is found by adjusting the width of the increase per 100s.

As we reduce the rate at which the width of  $\sigma_m$  increases, we are able to reach



higher masses of particles, and thus more information, before the uncertainty in the measured location overwhelms the interference pattern. Below around 10nm/100s we note that further decreasing this rate has very little effect. This is due to the limiting factor of the particle's diameter that was discussed previously.

We see in all the graphs of  $\langle \mathcal{H} \rangle$  plotted throughout this section that the information falls off rapidly as we pass a mass of  $2 \times 10^9$ u the radius of the particle becomes 70nm which is on the same order of magnitude as one half of the grating period. At this size, the phase shift effect of the Talbot grating begin to average over the whole particle, and begin to cancel out. A possible work around for this would be to use a different geometry of particle such that it can be extended in the  $x - y$  plane without increasing size in the  $z$  axis. In the next chapter, we consider a numerical approach to track the motion of arbitrary shaped particles in order to optimise their motional cooling. The approach developed for considering information translates directly into computing the Talbot coefficients. For spherical particles this was done via Mie theory, however, now we have the tools to find them for any shaped particle.

# Chapter 7

## Information Radiation in a Beam

So far, all of our discussion about the interferometer has assumed that we are using spherical particles. However, it may be more practical to use particles with different geometries. We have already discussed in Section 2.4 that it is possible to trap and control particles with different shapes, such as rods, disks, and ellipsoids. Using different shapes may allow us to reach higher mass particles and still observe an interference pattern in our interferometer. If we consider a flat disk, we can increase the radius of the disk without increasing its width allowing us to reach higher masses without reaching the size limit of the grating period. In our theoretical model, the shape of the particle is only considered in two places, in the mass density function  $\mu(\mathbf{x})$  in the CSL decoherence terms Eq. (5.6.5), and in the scattering amplitudes in the Talbot coefficients Eq. (5.4.41). This section is devoted to developing a numerical method to find the Talbot coefficients for any shaped particle. In doing this we also provide a method to find where information about the particle's motion is scattered to.

The work of this chapter was performed as part of a collaboration, which included an extended visit, with the Geraci group at Northwestern University. Their research involves trapping hexagonal plates in a standing wave trap for the purpose of high frequency gravitational wave detection. Understanding where the information of the particle's motion is scattered to is key in optimising the cooling scheme. Cooling the particle's motion is key to avoid unwanted noise and accurately detect gravitational waves [60, 139]. This work is then adapted

by taking the numerical scattering information that leads to the information patterns, and using this to build the vector scattering amplitudes in Eq. (5.4.44).

There exists a solution to the scattering amplitude under conditions of symmetry in the particle such as for spheres [26], spheroids [27], and infinite cylindrical rods [28], but not for arbitrary geometries. As a result, we must turn to numerical methods to solve this. We focus on using the program Scuff-EM [140] that uses a method of surface currents to solve the scattering problem. There are other software packages designed to solve scattering problems such as PyGDM2 and COMSOL. These work by discretising the volume of the object, while Scuff-EM only considers the surface of the object significantly reducing the computational resources required for large objects. However, these tools were used to cross check the Scuff-EM results during collaboration with the Geraci group. We are also interested in how information about the particle's position is scattered. Although we focus our discussions on hexagonal disks such as the ones used in [60], in practice our methods can be used for particles of any arbitrary shape.

In Sections 7.2.2 and 7.2.4, we develop a new method to find the information radiation patterns using the Fisher information and numerically calculated scattered electromagnetic fields. Then in Section 7.2.5 we apply this technique to hexagonal plates showing the applicability of this model for arbitrary shapes.

## 7.1 Scuff-EM

Scuff-EM (**S**urface **C**urrent/**F**ield **F**ormulation of **E**lectro**M**agnitism) is an open source implementation of the surface integral equation/boundary-element method (SIE/BEM) to solve electromagnetic scattering problems [140]. Starting with a known geometry in some medium (this could be vacuum, some fluid, or some gas) and illuminating the geometry with some known incident EM field, we can use these techniques to find the unknown scattered field as shown in Fig. 7.1. The SIE formulations solve for 2D surface currents,

$$\mathbf{K}(x) = \hat{\mathbf{n}}(x) \times \mathbf{H}(x) \tag{7.1.1a}$$

$$\mathbf{N}(x) = -\hat{\mathbf{n}}(x) \times \mathbf{E}(x) \tag{7.1.1b}$$

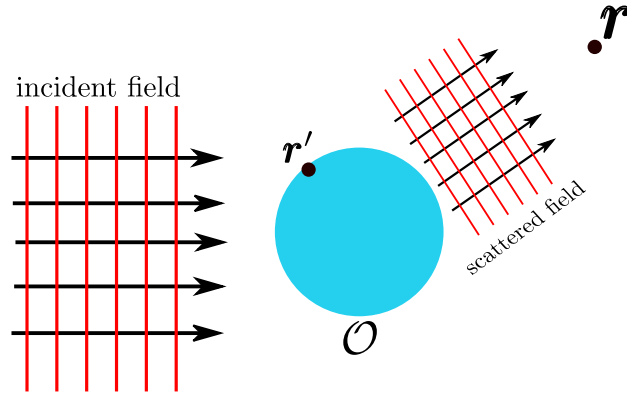


Figure 7.1: The scattered field at the point  $\mathbf{r}$  is calculated due to the surface currents at the point  $\mathbf{r}'$  on the surface of the object  $\mathcal{O}$  which arise from the incident field.

which are obtained from fields tangential to the body's surface. Here  $\hat{\mathbf{n}}(x)$  is the normal vector pointing out of the surface at the point  $x$  which lies on the surface of the body. For simplicity we adopt the following vector notation for fields, surface currents, and the Dyadic Green's function,

$$\mathcal{F} = \begin{pmatrix} \mathbf{E} \\ \mathbf{H} \end{pmatrix} \quad (7.1.2a)$$

$$\mathcal{C} = \begin{pmatrix} \mathbf{K} \\ \mathbf{N} \end{pmatrix} \quad (7.1.2b)$$

$$\mathcal{G} = \begin{pmatrix} \Gamma^{EE} & \Gamma^{EM} \\ \Gamma^{ME} & \Gamma^{MM} \end{pmatrix} \quad (7.1.2c)$$

where we have used the  $3 \times 3$  Dyadic Green's function  $\Gamma^{AB}$  giving the field of type  $A$  from the surface current of type  $B$ . We can now find the fields on the surface as a function of surface currents as

$$\mathcal{F} = \mathcal{M}\mathcal{C} \quad (7.1.3a)$$

$$\mathcal{M} = \begin{pmatrix} \frac{\hat{\mathbf{n}} \cdot \nabla}{i\omega\epsilon} & \hat{\mathbf{n}} \times \\ -\hat{\mathbf{n}} \times & \frac{\hat{\mathbf{n}} \cdot \nabla}{i\omega\mu} \end{pmatrix}. \quad (7.1.3b)$$

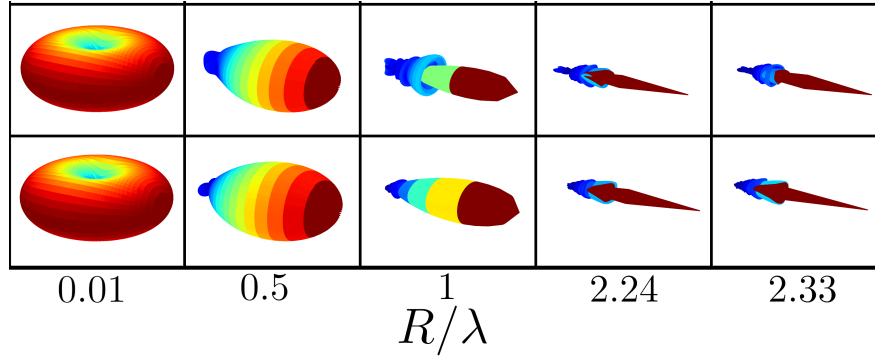


Figure 7.2: Electric fields scattered from dielectric spheres illuminated by plane waves with different size parameters  $R/\lambda$  and refractive index of  $n = 1.5$  suspended in a vacuum. The top row are analytical results while the bottom row are results from Scuff-EM. Differences in the scattered fields are the result of finite meshing in Scuff-EM.

where Eq. (7.1.3a) is the matrix-vector product,

$$\mathcal{F} = \begin{pmatrix} \frac{\hat{\mathbf{n}} \cdot \mathbf{K}}{i\omega\epsilon} + \hat{\mathbf{n}} \times \mathbf{N} \\ -\hat{\mathbf{n}} \times \mathbf{K} + \frac{\hat{\mathbf{n}} \cdot \mathbf{E}}{i\omega\mu} \end{pmatrix} \quad (7.1.4)$$

where the values of  $\epsilon$  and  $\mu$  are the permittivity and the permeability of either the object or surrounding medium respectively. Eq. (7.1.3) only describes fields on the surface of the object  $\mathcal{O}$ . The field at any point in space  $\mathbf{r}$ , either inside or outside the object, is given by

$$\mathcal{F}(\mathbf{r}) = \begin{cases} +\mathcal{G}^{\text{out}}(\mathbf{r}, \mathbf{r}') * \mathcal{C}(\mathbf{r}') + \mathcal{F}_{\text{sources}}^{\text{out}}(\mathbf{r}), & \mathbf{r} \notin \mathcal{O} \\ -\mathcal{G}^{\text{in}}(\mathbf{r}, \mathbf{r}') * \mathcal{C}(\mathbf{r}') + \mathcal{F}_{\text{sources}}^{\text{in}}(\mathbf{r}), & \mathbf{r} \in \mathcal{O} \end{cases} \quad (7.1.5)$$

where  $\mathcal{G}^{\text{out}, \text{in}}$  are the Green's functions (Eq. (7.1.2c)) for the medium outside and inside the body,  $\mathcal{F}_{\text{sources}}^{\text{out}, \text{in}}$  are the fields created by point sources, and  $*$  refers to a convolution [141].

### 7.1.1 Numerical solutions

We want to apply this method to a numerical solver so that we can find the field scattered by particles with arbitrary geometry. The first step is to discretise the

object. We use some chosen software package to convert an object into the right format. In our work, we use the software Gmsh [142] to generate basic meshes of an object and then pass this simple mesh to mmgs [143] which converts the mesh into a set of roughly equally sized triangles that Scuff-EM can use to optimise the calculations by reusing surface currents, though in principal any meshing software that can produce the correct form of meshes can be used. Now this mesh can be passed to Scuff-EM.

This first thing Scuff-EM does is to assign a basis function to each interior edge on the mesh. These basis functions are given by

$$\mathbf{f}_n(\mathbf{r}) = \begin{cases} \frac{l_n}{2A_n^+} \boldsymbol{\rho}_n^+, & \mathbf{r} \text{ in } T_n^+ \\ \frac{l_n}{2A_n^-} \boldsymbol{\rho}_n^-, & \mathbf{r} \text{ in } T_n^- \\ 0, & \text{otherwise} \end{cases} \quad (7.1.6)$$

where  $l_n$  is the length of the  $n$ th edge,  $A_n^\pm$  is the area of the triangle  $T_n^\pm$ , and  $\boldsymbol{\rho}_n^\pm$  is the position vector of the triangle defined with respect to its free vertex. The plus or minus defines the direction of the surface current with respect to the  $n$ th edge. The functions  $\mathbf{f}_n(\mathbf{r})$  are used to represent the surface currents [144].

We now have the necessary components to solve for the boundary element matrix  $\mathbf{M}$  and RHS vector  $\mathbf{v}$ ,

$$\mathbf{M}_{mn} = \langle \mathbf{f}_m | \boldsymbol{\Gamma}^{EE} | \mathbf{f}_n \rangle \quad (7.1.7)$$

$$\mathbf{v}_m = - \langle \mathbf{f}_m | \mathbf{E}^i \rangle. \quad (7.1.8)$$

This is the most computationally expensive part of the calculations as for every element we have a four dimensional integral, surface integrals over two triangles, that must be solved numerically. The more edges we have, the more of these integrals must be performed. We then must solve the linear system  $\mathbf{M}\mathbf{k} = \mathbf{v}$  where  $\mathbf{k}$  is a vector of the surface-current expansion coefficients  $k_n$ . By phrasing this as a matrix inversion problem Scuff-EM is able to make use of highly optimised routines. By using the surface current density  $\mathbf{K}(\mathbf{r}) = \sum k_n \mathbf{f}_n(\mathbf{r})$ , we can find

the scattered electric and magnetic fields,

$$\mathbf{E}_S(\mathbf{r}) = \sum_n k_n \int \Gamma^{EE}(\mathbf{r}, \mathbf{r}') \mathbf{f}_n(\mathbf{r}') d\mathbf{r}' \quad (7.1.9)$$

$$\mathbf{H}_S(\mathbf{r}) = \sum_n k_n \int \Gamma^{ME}(\mathbf{r}, \mathbf{r}') \mathbf{f}_n(\mathbf{r}') d\mathbf{r}'. \quad (7.1.10)$$

This provides a robust and simple way to find the electric and magnetic fields scattered from a dielectric object and is computationally cheap to evaluate the field after solving the matrix inversion problem [145]. Fig. 7.2 shows the electric fields scattered from a sphere illuminated by a plane wave for various size parameters  $R/\lambda$  as calculated by Scuff-EM compared with the analytical results. For simplicity, we keep a constant particle size and alter the size parameter by changing the wavelength of the incident light.

### 7.1.2 Scuff-EM Implementation of a Gaussian Beam

Because particles are often levitated in Gaussian TEM<sub>00</sub> laser beam, we want to ensure that the implementation of the Gaussian beam in Scuff-EM is accurate. We also discovered an apparent discrepancy with our results compared to those presented in [146] and so we sought to ensure that the Scuff-EM implementation was accurate. Working in the paraxial approximation, we can define an  $x$  polarised beam propagating in the  $z$  axis as,

$$\mathbf{E}(r, z) = E_0 \hat{\mathbf{x}} \frac{w_0}{w(z)} \exp\left(\frac{-r^2}{w(z)^2}\right) \exp\left[-i\left(kz + k\frac{r^2}{2R(z)} - \phi(z)\right)\right] \quad (7.1.11)$$

where  $r$  is the radial distance from the propagation axis,  $z$  is the direction along the propagation axis from the focal point of the beam, and  $w_0$  is the beam waist, that is the radius of the beam at the focal point [147]. We have also defined the following functions,

$$w(z) = w_0 \sqrt{1 + \left(\frac{\lambda z}{\phi w_0^2}\right)^2} \quad (7.1.12)$$

is the beam radius at the point  $z$ , defined as the point at which the field amplitude falls to  $E_0/e$ ,

$$R(z) = z \left[1 + \left(\frac{\pi w_0^2}{z\lambda}\right)^2\right] \quad (7.1.13)$$

is the radius of curvature of the wave front at the point  $z$ ,

$$\phi(z) = \arctan\left(\frac{z\lambda}{\pi w_0^2}\right) \quad (7.1.14)$$

is the Gouy phase shift resulting from the act of focusing the beam [148]. This description is only valid in the paraxial regime where the divergence angle  $\theta_d = \lambda/(\pi w_0)$  is small enough that we can use the small angle approximation of trigonometry. However, if we want to use a more highly focused beam we must go beyond the paraxial approximation.

The Gaussian beam implementation built into Scuff-EM is based on [149] which defines Gaussian beams beyond the paraxial approximation based on a complex source point model. In this model electric dipoles are oriented along the  $x$ -axis, polarisation axis, and magnetic dipoles are oriented along the  $y$ -axis. In the complex source point model, we place these dipoles at the point  $z_0$ , the electric fields from these sources can be written as,

$$\begin{aligned} f(kR) &= j_0(kR) + j_2(kR) \\ g(kR) &= j_0(kR) + j_2(kR)/2 \end{aligned} \quad (7.1.15)$$

where  $j_n(x)$  is the spherical Bessel function of order  $n$ ,  $k$  is the wave number, and  $R = \sqrt{x^2 + y^2 + (z - iz_0)^2}$  is the radius of curvature of the beam. This gives the electric field as,

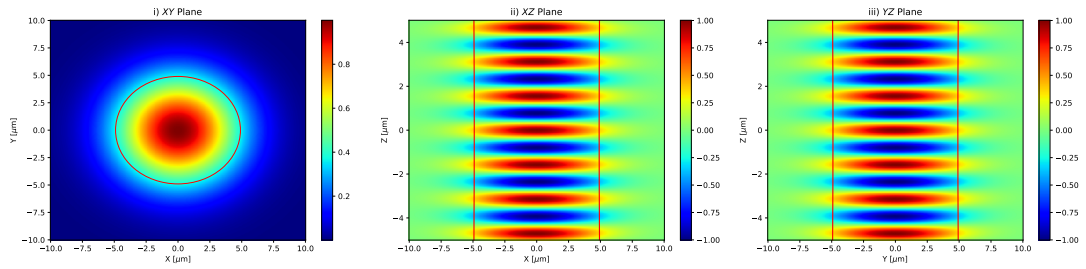
$$\begin{aligned} \mathbf{E} = & \left\{ g(kR) + [f(kR) - g(kR)] \frac{x^2}{R^2} + \frac{i}{2} f(kR) k(z - iz_0) \right\} \hat{\mathbf{x}} \\ & + [f(kR) - g(kR)] \frac{xy}{R^2} \hat{\mathbf{y}} \\ & + \left\{ [f(kR) - g(kR)] \frac{xz}{R^2} - \frac{i}{2} f(kR) kx \right\} \hat{\mathbf{z}} \end{aligned} \quad (7.1.16)$$

We can test the Scuff-EM implementation of the Gaussian beam by plotting the field generated in the absence of a scatterer. This is shown in Fig. 7.3

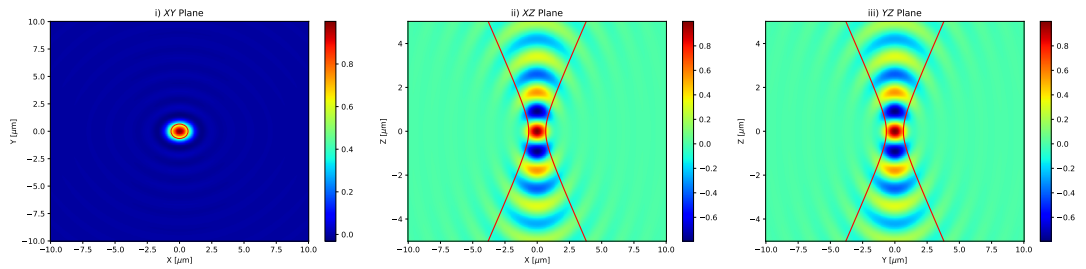
### 7.1.3 Alternative Method for Defining a Gaussian Beam

In order to test our numerical approach, we want to be able to compare to analytical results, such as the ones presented in [146]. The Gaussian beam defined





(a) Beam focused by a 0.1 NA lens leading to a beam waist of  $4.9\mu\text{m}$  and a divergence angle of 0.1 radians.



(b) Beam focused by a 0.75 NA lens leading to a beam waist of  $0.66\mu\text{m}$  and a divergence angle of 0.75 radians.

Figure 7.3: The real part of the electric field as output by Scuff-EM in the absence of a scatterer for two Gaussian beams with different beam waists. The red lines show the beam radius as given by Eq. (7.1.12)

in [146] is based off integrals over a mono-chromatic plane wave  $\mathbf{E}_{\text{in}}$ . This is the Angular Spectrum Method [29]. In this approximation, the field close to the focus takes the form,

$$\mathbf{E}(\mathbf{r}) = \frac{k_0 f}{2\pi i} \int_{\mathcal{D}^\pm} \mathbf{E}_\infty^\pm(f, \theta_k, \phi_k) \exp[ikr \cos \theta_k \cos \theta + ikr \sin \theta_k \sin \theta \cos(\phi_k - \phi)] d\Omega_k \quad (7.1.17)$$

where  $f$  is the focal length,  $k_0 = 2\pi/\lambda$ ,  $\text{NA} = \sin \theta_{\text{NA}}$ , and

$$\begin{aligned} \mathbf{E}_\infty^\pm(f, \theta_k, \phi_k) &= \sqrt{|\cos \theta_k|} [\mathbf{E}_{\text{in}}(f, \theta_k, \phi_k) \cdot \mathbf{e}_\phi(\theta_k, \phi_k)] \mathbf{e}_\phi(\theta_k, \phi_k) \\ &\pm \sqrt{|\cos \theta_k|} [\mathbf{E}_{\text{in}}(f, \theta_k, \phi_k) \cdot \mathbf{e}_\rho(\theta_k, \phi_k)] \mathbf{e}_\phi(\theta_k, \phi_k) \end{aligned} \quad (7.1.18)$$

and our integration is over the limits  $\mathcal{D}_+ = \{0 \leq \theta_k \leq \theta_{\text{NA}}, 0 \leq \phi_k \leq 2\pi\}$ , and  $\mathcal{D}_- = \{\pi - \theta_{\text{NA}} \leq \theta_k \leq \pi, 0 \leq \phi_k \leq 2\pi\}$ .

We can achieve the same field in Scuff-EM via the method of numerical spherical integration called the Lebedev rule which we had used in Sec. 5.4.3. From this we can write the field as a weighted sum of plane waves that can be passed to Scuff-EM to define the Gaussian beam. For the rest of this work, we use this field in Scuff-EM.

## 7.2 Information Radiation

A particle trapped in an optical trap will scatter the trapping light in all directions. This scattered light can be collected and used to track the position of the particle as described in Section 2.3. However, in order to know the position of the particle with maximum precision, we must know where the light that carries the information about the particle's location is scattered to. It is important to note that the scattered information is not the same as the scattered power. For example, the power scattered by a dipole backwards and forwards is the same, but the forward scattered light carries no information about the particle's position. For this, we use Information Radiation Patterns (IRPs) to show where the information on the particle motion is scattered to.

For trapped spheres there exists analytical solutions to find the IRP for each degree of freedom of the particle which are discussed below. Initially there only existed a solution for particles in the Rayleigh limit [41], but later a method for

solving the information scatter for arbitrary sized spheres was demonstrated [146]. The Rayleigh regime method used an interference between the scattered light and an ideal reference field to determine the direction that the information is scattered to as the particle moves in the direction  $\mu$ .

### 7.2.1 Analytical Information Radiation Pattern in the Rayleigh Limit

For particles in the Rayleigh regime, we can use the model presented in [41] to find the information patterns. We begin by modelling the incident electric field as a plane-wave. If we assume that it is  $x$  polarised and travels in the  $z$  direction, it takes the form,

$$\mathbf{E}_i(\mathbf{r}_0) = E_0 \mathbf{n}_x \exp(iAkz_0) \quad (7.2.1)$$

where  $\mathbf{r}_0 = (x_0, y_0, z_0)$  is the position of the particle and  $A$  is a geometric factor resulting from the Gouy phase-shift. In a mildly focused beam, such as the one we are considering here, it can be shown that  $A = 1 - (kz_R)^{-1}$  where  $z_R$  is the Rayleigh range [150]. The particle then radiates the scattered field

$$\mathbf{E}_s(\mathbf{r}) = \mathbf{E}_d(\mathbf{r}) \exp[-ik(\mathbf{r}_0 \cdot \mathbf{n}_r - Az_0)] \quad (7.2.2)$$

where  $\mathbf{n}_r$  is the unit vector oriented in the radial direction.  $\mathbf{E}_d(\mathbf{r})$  is the field emitted by an  $x$  oriented dipole at the origin and emits the differential power

$$dp_{\text{dip}}(\theta, \phi) = \frac{3P_{\text{dip}}}{8\pi} [1 - \sin^2(\theta) \cos^2(\phi)] d\Omega \quad (7.2.3)$$

where  $P_{\text{dip}}$  is the total radiated power. For a Rayleigh sphere, this can be thought of as the power that would be scattered into the solid angle  $d\Omega$  from the particle should it be at rest in the origin.

Because the information of the particle's position is contained only in the phase of Eq. (7.2.2), we can make use of a homodyne measurement by interfering the scattered light with an ideal reference field,

$$\mathbf{E}_{\text{ref}}(\mathbf{r}) = -i\gamma \mathbf{E}_d(\mathbf{r}) \quad (7.2.4)$$

where  $\gamma \gg 1$  such that the ideal reference field is the field scattered from the particle at rest at the origin with a much greater intensity and a  $\pi/2$  phase shift.

By interfering the scattered and reference fields, we can read out a power on a detector covering the solid angle  $d\Omega$ , located in the far field at the position  $(\theta, \phi)$  as,

$$dp_{\text{det}}(\theta, \phi) = [\gamma^2 + 2\gamma k(\mathbf{r}_0 \cdot \mathbf{n}_r - Az_0)]dp_{\text{dip}}. \quad (7.2.5)$$

We consider the particle moving in only one direction  $\mu \in (x, y, z)$  such that its position in the other two axes is 0. This then allows us to simplify Eq. (7.2.5) to,

$$dp_{\text{det}}^{(x)}(\theta, \phi) = [\gamma^2 + 2\gamma k \sin(\theta) \cos(\phi)x_0]dp_{\text{dip}} \quad (7.2.6a)$$

$$dp_{\text{det}}^{(y)}(\theta, \phi) = [\gamma^2 + 2\gamma k \sin(\theta) \sin(\phi)y_0]dp_{\text{dip}} \quad (7.2.6b)$$

$$dp_{\text{det}}^{(z)}(\theta, \phi) = [\gamma^2 + 2\gamma k(\cos(\theta)z_0 - Az_0)]dp_{\text{dip}} \quad (7.2.6c)$$

which is linearly dependent on the position in the  $\mu$  axis. Note that we only need to consider the effects of the Gouy phase shift of motion in the  $z$  axis. The first term in these equations are the same and independent of the particle position. It dominates the measurement fluctuations as shot noise. Therefore, we can write the power spectral density of these fluctuations as

$$ds_{\text{pp}}^{\text{det}}(\theta, \phi) = \frac{\hbar kc}{2\pi}\gamma^2 dp_{\text{dip}}. \quad (7.2.7)$$

We use this to find the power spectral density of the measurement imprecision at the detector for each direction of particle motion as,

$$s_{\text{imp}}^{(x)}(\theta, \phi) = \frac{ds_{\text{pp}}^{\text{det}}(\theta, \phi)}{(2\gamma k \sin(\theta) \cos(\phi)dp_{\text{dip}})^2} \quad (7.2.8a)$$

$$s_{\text{imp}}^{(y)}(\theta, \phi) = \frac{ds_{\text{pp}}^{\text{det}}(\theta, \phi)}{(2\gamma k \sin(\theta) \sin(\phi)dp_{\text{dip}})^2} \quad (7.2.8b)$$

$$s_{\text{imp}}^{(z)}(\theta, \phi) = \frac{ds_{\text{pp}}^{\text{det}}(\theta, \phi)}{(2\gamma k(\cos(\theta) - Az_0)dp_{\text{dip}})^2}. \quad (7.2.8c)$$

Finally, we find the information as a function of direction to be,

$$\mathcal{I}_\mu(\theta, \phi) = \frac{S_{\text{imp}}^{(\mu)}}{s_{\text{imp}}^{(\mu)}(\theta, \phi)} \quad (7.2.9)$$

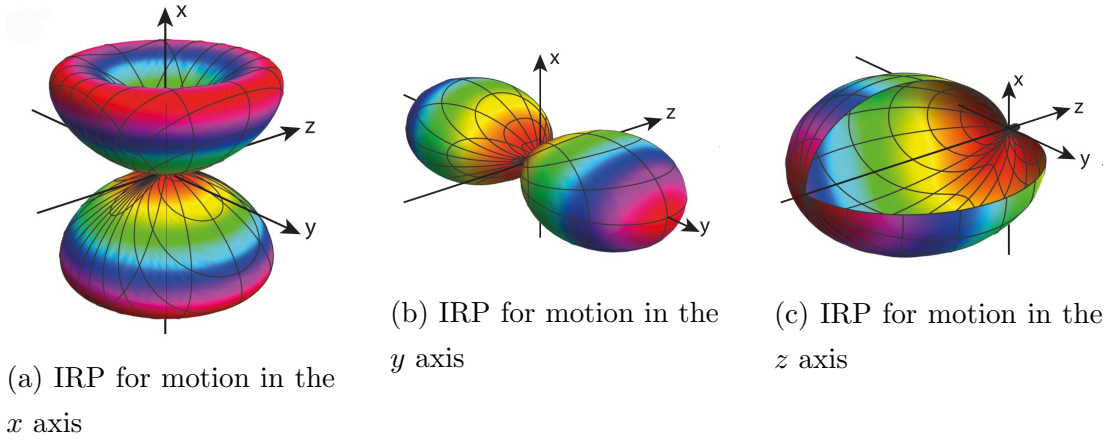


Figure 7.4: The information patterns for particle motion in each axis. Reproduced from [41].

where  $S_{\text{imp}}^{(\mu)}$  is the total imprecision and is given by  $S_{\text{imp}}^{(\mu)} = [\int s_{\text{imp}}^{(\mu)}(\theta, \phi)]^{-1}$ . This leads to the set of equations,

$$S_{\text{imp}}^{(x)} = 5 \frac{\hbar c}{8\pi k} \frac{1}{P_{\text{dip}}} \quad (7.2.10a)$$

$$S_{\text{imp}}^{(y)} = \frac{5}{2} \frac{\hbar c}{8\pi k} \frac{1}{P_{\text{dip}}} \quad (7.2.10b)$$

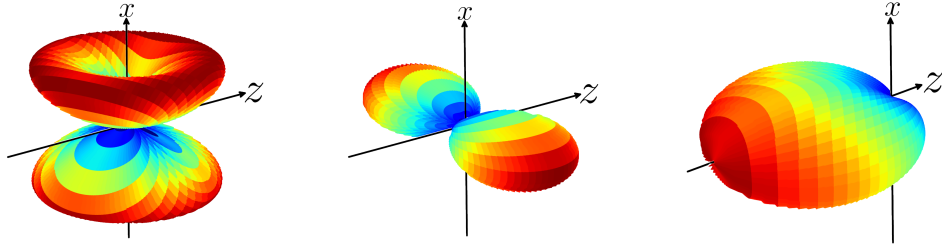
$$S_{\text{imp}}^{(z)} = \frac{1}{(5/2) + A^2} \frac{\hbar c}{8\pi k} \frac{1}{P_{\text{dip}}}. \quad (7.2.10c)$$

The imprecision in the  $z$  axis is a result of the Gouy phase shift that occurs due to the focusing of the light. For motion in the  $x$  and  $y$  axes it results from the polarisation of the incident light.

## 7.2.2 Numerical Solution for the IRP for Rayleigh Spheres

We can use the output of the scattered fields from Scuff-EM (or any other numerical solver) to produce the IRPs for each motional axis. To begin, we model a spherical particle using the gmsh software [151] with relative permittivity  $\epsilon = 2.07$ , and a size parameter of  $R/\lambda = 0.01$ , which is comfortably in the Rayleigh regime and illuminate it with an  $x$ -polarised plane wave travelling in the positive  $z$  direction with a wavelength of  $\lambda = 1550\text{nm}$ .

We find the reference field by placing the scatterer at the origin and recording the scattered field. This field is then multiplied by  $-i\gamma$  where  $\gamma = 1000$  to find the reference field given in Eq. (7.2.4). Taking this field, we can also find the value of  $dp_{\text{dip}}$  across each detector. For simplicity, we rewrite the denominators in Eq. (7.2.8) as  $d\beta_\mu^2$ . We also note that due to the linearity of Eqs. (7.2.6), we can rewrite them as a straight line  $dp_{\text{det}}^{(\mu)} = c + d\beta_\mu\mu$ . By positioning the particle at various displacements in the axis  $\mu$  and measuring the scattered field, we can plot the differential power at each detector as a function of particle position. Then, using parameter estimation techniques, in this case we use a best fit straight line, we find the value of  $d\beta_\mu$  and insert this into the relevant Eq. (7.2.8) to find the imprecision that will lead to the corresponding information radiation pattern as shown in Fig. 7.5.



(a) IRP for the  $x$  position (b) IRP for the  $y$  position (c) IRP for the  $z$  position

Figure 7.5: Information radiation patterns for the  $\mu$  location of a particle illuminated by a plane wave.

### 7.2.3 Analytical Information Patterns for Large Spheres

For particles with arbitrary size and refractive index, we have two main approaches to find the information pattern for the particle's motion. First we can use a method informed by quantum mechanics from [146]. This uses the coupling between inelastically scattered photons to phonons of particle motion through Stokes and anti-Stokes scattering. The second method is equivalent to the first but measures the amount of information entering an area from the Fisher information operator.

### 7.2.3.1 Quantum Approach

The Hamiltonian describing the interaction between the particle's motion and the electromagnetic field is given by,

$$\hat{H} = \frac{\hat{\mathbf{p}}^2}{2m} + V(\hat{\mathbf{r}}) + \hat{H}_{\text{em}} - \hat{\mathcal{F}} \cdot \hat{\mathbf{r}} \quad (7.2.11)$$

where the first term is the standard motional Hamiltonian, the second is optical trapping potential, the third describes the free dynamics of the field in the presence of a dielectric particle, and the last term describes the interaction between the particle motion and the electromagnetic field. It is this last term that we are interested in here. The radiation pressure operator  $\hat{\mathcal{F}}$  has an expectation value given by,

$$\langle \hat{\mathcal{F}} \rangle = \nabla V(\mathbf{r})|_{\mathbf{r}=0}. \quad (7.2.12)$$

Also assuming that the particle is trapped in a standard three-dimensional harmonic potential, we obtain,

$$V(\hat{\mathbf{r}}) = \frac{m}{2} \sum_{\mu} \Omega_{\mu}^2 \hat{r}_{\mu}^2 \quad (7.2.13)$$

for each axis  $\mu \in (x, y, z)$ . By making use of Eq. (7.2.11) that the Heisenberg equation of motion for the  $\mu$  component for the particle's motion is given by,

$$\frac{d^2 \hat{r}_{\mu}}{dt^2} + \Omega_{\mu}^2 \hat{r}_{\mu} = \frac{\hat{\mathcal{F}}_{\mu}}{m}. \quad (7.2.14)$$

By deriving the equivalent classical equation of motion and promoting the dynamical variables to quantum operators, and comparing with the previous equation, we are able to find an expression for the vector components of the radiation pressure operator in terms of the electric and magnetic field operators  $\hat{\mathbf{E}}(\mathbf{r})$  and  $\hat{\mathbf{B}}(\mathbf{r})$ ,

$$\hat{\mathcal{F}}_{\mu} = -\frac{\epsilon_0}{2} \lim_{r \rightarrow \infty} r^2 \int (\mathbf{e}_r \cdot \mathbf{e}_{\mu}) [\hat{\mathbf{E}}^2(\mathbf{r}) + c^2 \hat{\mathbf{B}}^2(\mathbf{r})] d\Omega \quad (7.2.15)$$

where  $d\Omega$  is the solid angle element,  $\mathbf{e}_r$  is the radial unit vector, and  $\mathbf{e}_{\mu}$  is the unit vector in the  $\mu$  direction. In terms of the normalised scattering eigenmodes

for a fixed sphere at the origin  $\mathbf{F}_\kappa(\mathbf{r})$ , the field operators are,

$$\hat{\mathbf{E}}(\mathbf{r}) = i \sum_{\kappa} \sqrt{\frac{\hbar\omega_{\kappa}}{2\epsilon_0}} [\mathbf{F}_\kappa(\mathbf{r})\hat{a}_{\kappa} - \text{H.c.}] \quad (7.2.16)$$

$$\hat{\mathbf{B}}(\mathbf{r}) = \sum_{\kappa} \sqrt{\frac{\hbar}{2\epsilon_0\omega_{\kappa}}} [\nabla \times \mathbf{F}_\kappa(\mathbf{r})\hat{a}_{\kappa} + \text{H.c.}] \quad (7.2.17)$$

where the index  $\kappa$  is a multi-index containing the polarisation index and the wave vector, and the term H.c. indicates the hermitian conjugate.

We can now write the Hamiltonian Eq. (7.2.11) as,

$$\hat{H} = \hbar \sum_{\mu} \Omega_{\mu} \hat{b}_{\mu}^{\dagger} \hat{b}_{\mu} + \hbar \sum_{\kappa} \omega_{\kappa} \hat{a}_{\kappa}^{\dagger} \hat{a}_{\kappa} + \hbar \sum_{\kappa\kappa'\mu} g_{\kappa\kappa'\mu} \hat{a}_{\kappa}^{\dagger} \hat{a}_{\kappa} (\hat{b}_{\mu}^{\dagger} + \hat{b}_{\mu}) \quad (7.2.18)$$

where  $\hat{a}_{\kappa}^{\dagger}$  and  $\hat{a}_{\kappa}$  are the photonic creation and annihilation operators, and  $\hat{b}_{\mu}^{\dagger}$  and  $\hat{b}_{\mu}$  are the bosonic creation and annihilation operators. The third term in Eq. (7.2.18) describes the Stokes and anti-Stokes processes of the light scattering to produce or absorb a phonon in the  $\mu$  direction.

The interaction between the photons and phonons are described by the coupling rates  $g_{\kappa\kappa'\mu}$  which are given by,

$$g_{\kappa\kappa'\mu} = r_{0\mu} \frac{c\sqrt{k k'}}{2} \lim_{r \rightarrow \infty} r^2 \int (\hat{\mathbf{e}}_r \cdot \hat{\mathbf{e}}_{\mu}) \left[ \mathbf{F}_{\kappa}^*(\mathbf{r}) \cdot \mathbf{F}_{\kappa'}(\mathbf{r}) + \frac{1}{k k'} \nabla \times \mathbf{F}_{\kappa}^*(\mathbf{r}) \cdot \nabla \times \mathbf{F}_{\kappa'}(\mathbf{r}) \right] d\Omega \quad (7.2.19)$$

where  $\mathbf{F}_{\kappa}(\mathbf{r})$  are the normalised scattering eigenmodes in the presence of an un-moving dielectric sphere. We assume that the particle is in the presence of a classical field given by,

$$\mathbf{E}_{\text{cl}}(\mathbf{r}, t) = i \sum_{\kappa} \sqrt{\frac{\hbar\omega_{\kappa}}{2\epsilon_0}} [\mathbf{F}_{\kappa}(\mathbf{r})\alpha_{\kappa} e^{-i\omega_{\kappa}t} - \text{c.c.}] \quad (7.2.20)$$

where  $\alpha_{\kappa}$  is the coherent complex amplitude of the mode  $\kappa$ . This allows us to write the linearised coupling rate,

$$G_{\kappa\mu} = \sum_{\kappa'} \alpha_{\kappa'} g_{\kappa\kappa'\mu}. \quad (7.2.21)$$



Because we are only concerned with where the information goes, and not if it comes from a Stokes or anti-Stokes photon, we can write the information about the particle's motion in the  $\mu$  axis as

$$\mathcal{I}_\mu(\theta, \phi) = \frac{\sum_g \int_0^\infty k^2 |G_{\kappa\mu}|^2 \delta(\omega_\kappa - \omega_0) dk}{\sum_g |G_{\kappa\mu}|^2 \delta(\omega_\kappa - \omega_0)}. \quad (7.2.22)$$

The methods described here are useful analytical methods to produce the IRPs for spheres. However, this method is difficult to implement numerically and has no obvious extension to particles with arbitrary geometry. By using arguments from Fisher information, we can use numerical techniques to find the IRPs for particles with any shape.

### 7.2.3.2 Fisher Information Approach

In the method derived by Hüpfl et al. [152] the equivalence between the Poynting vector and the Fisher information vector is utilised to derive the information passing through a given area. In the far field regime, the time averaged Poynting vector is given by,

$$\mathbf{S}^P = \text{Re}[\mathbf{E}_\omega^* \times \mathbf{H}_\omega]/2 \quad (7.2.23)$$

where  $\mathbf{E}_\omega$  and  $\mathbf{H}_\omega$  are the complex amplitudes of the electric and magnetic fields respectively. From this, we define the amount of optical power entering a photo detector located at  $(\theta, \phi)$  to be,

$$P(\theta, \phi) = \int \mathbf{S}^P \cdot d\mathbf{A}_i \quad (7.2.24)$$

where  $\mathbf{A}_i$  is the outward pointing area vector for the detector  $i$  located at  $(\theta, \phi)$ .

We can define the Fisher information flux in analogy to the Poynting vector as,

$$\mathbf{S}^{\text{FI}} = \frac{2}{\hbar\omega} \text{Re}[\partial_\mu \mathbf{E}_\omega^* \times \partial_\mu \mathbf{H}_\omega]. \quad (7.2.25)$$

Here we differentiate the fields with respect to the quantity  $\mu$ . A full derivation is provided in [152]. In this case, the fields are the scattered fields from the particle as it moves through the  $\mu$  axis. We then find the rate of information transfer across a detector to be,

$$\mathcal{I}_\mu(\theta, \phi) = \int \mathbf{S}^{\text{FI}} \cdot d\mathbf{A}_i. \quad (7.2.26)$$

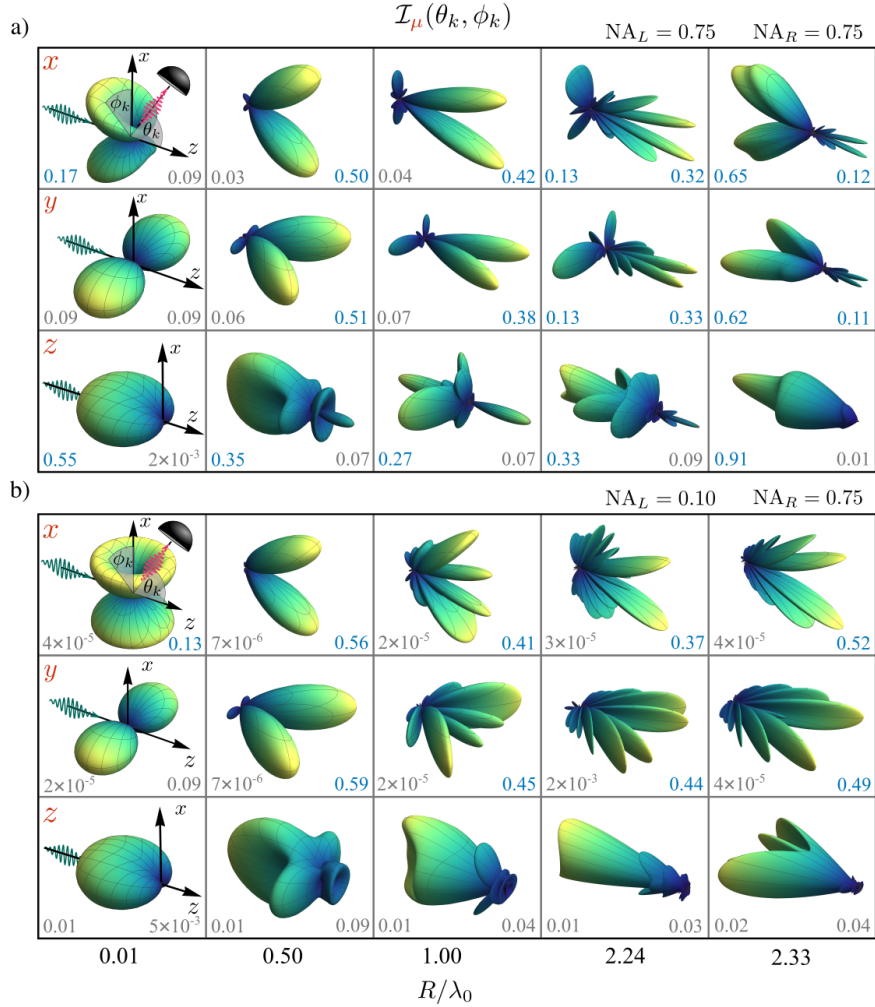


Figure 7.6: The information radiation patterns for spheres of different sizes illuminated by an  $x$  polarised Gaussian beam propagating in the positive  $z$  direction as shown in [146]. In a) the beam is focused to a waist of  $w_0 = 0.66\mu\text{m}$  by a  $\text{NA}=0.75$  lens, and in b) it is focused to a waist of  $4.9\mu\text{m}$  by a  $\text{NA}=0.1$  lens. Each panel shows the detection efficiency for the left and right lens, when in blue the detection efficiency is sufficient to allow ground state cooling.

It is clear that it is much easier to apply a numerical approach to this method than the method given in Sec. 7.2.3.1. We must simply find the scattered electric and magnetic fields as our particle moves through some axis  $\mu$ . Because this method does not assume spheres, we are also able to extend this to particles with arbitrary geometries. It is also possible to see how other degrees of freedom, such as rotational motion, can affect the IRP simply by changing this property. For example, we can rotate asymmetrical particles and generate an IRP for the particle's rotation.

## 7.2.4 Numerical Information Patterns for Large Spheres

We use the output from Scuff-EM of the scattered electric and magnetic fields to find the information radiation pattern based on Sec. 7.2.3.2. We begin, as before, by meshing the particle of interest and illuminating it by the relevant EM field. We then measure the scattered field on the surface of an imaginary sphere with a radius  $r = 1\text{m}$  such that we are in the far field regime. We do this for the particle being located at the locations  $\pm\lambda/100$  such that the distance between the points is sufficiently small such that the change in the scattered fields is linear and we can use a first-order centred difference approximation of the derivative. At each location  $(\theta, \phi)$ , we measure the complex scattered electric and magnetic fields for the particle as  $\mathbf{E}_\mu^\pm(\theta, \phi)$  and  $\mathbf{H}_\mu^\pm(\theta, \phi)$ , where the  $\pm$  denotes if the particle is located on the positive or negative side of the origin, and  $\mu$  determines the axis the particle is displaced in. For ease of notation, we split the vectors into  $\mathbf{E} = [E_x, E_y, E_z]$ . Thus, the components for the relevant differentials is given by,

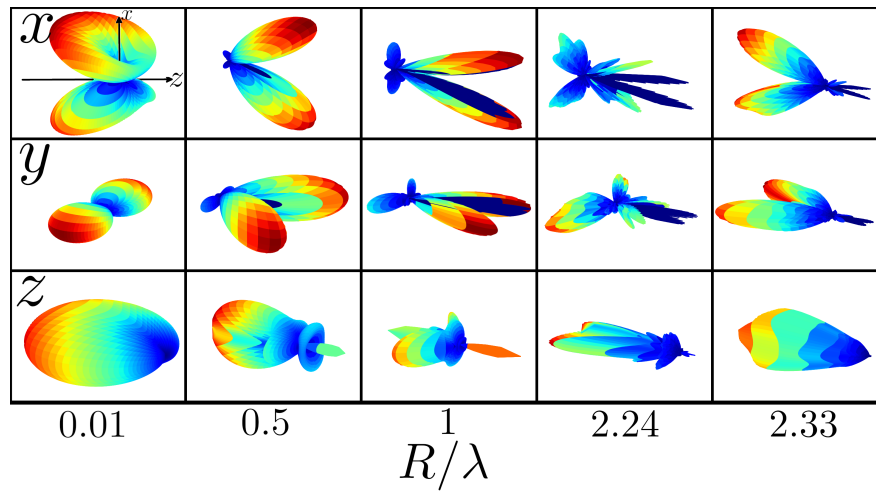
$$\partial_\mu E_{j,\mu}^* \approx \frac{E_{j,\mu}^{*+} - E_{j,\mu}^{*-}}{\lambda/100 - (-\lambda/100)} \quad (7.2.27\text{a})$$

$$\partial_\mu H_{j,\mu} \approx \frac{H_{j,\mu}^+ - H_{j,\mu}^-}{\lambda/100 - (-\lambda/100)} \quad (7.2.27\text{b})$$

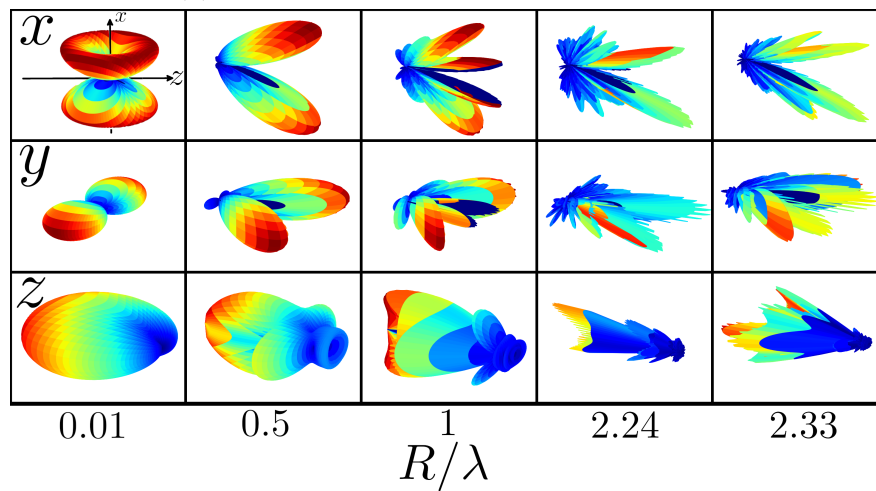
where  $j = x, y, z$ . Then, by inserting EQs. (7.2.27) into Eq. (7.2.25), we find the information radiation patterns as

$$\mathcal{I}_\mu(\theta, \phi) = \mathbf{S}^{\text{FI}}(\theta, \phi) \cdot \mathbf{A}_i \quad (7.2.28)$$

where the area vector of the detector pointing away from the origin.



(a) IRPs created with a lens of NA = 0.75.



(b) IRPs created with a lens of NA = 0.1.

Figure 7.7: Information patterns for varying radii of spherical particles in Gaussian beams formed by lenses of different numerical apertures. These plots are generated by applying the method in Sec. 7.2.3.2 in Scuff-EM.

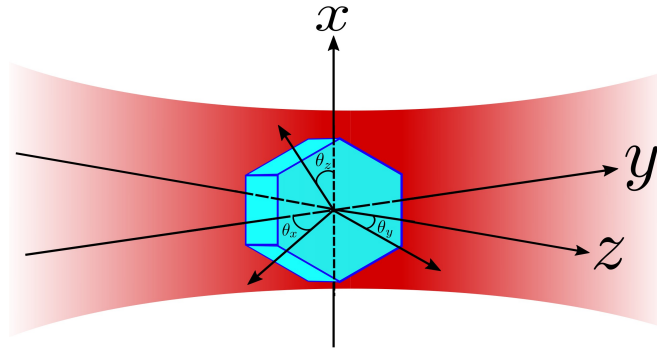


Figure 7.8: A sketch of a hexagonal plate trapped in a standing wave showing all six degrees of freedom.

Care must be taken when deciding the numerical accuracy when producing the IRPs. We must ensure that the mesh of the object is sufficiently dense such that the scattered fields are accurate, but there remains a practical limit to the mesh density we can use set by computational resources. Increasing the number of points in the mesh increases the accuracy of the replicated IRP. However, care must be taken as the complexity of the Scuff-EM calculations increases with the number of edges by a factor of  $N^4$  [145].

Comparing the results from Fig. 7.7 and Fig. 7.6, we can confirm a qualitative agreement between the numerical and analytical methods, apart from in the  $R/\lambda = 2.24$  spheres moving in the  $z$  axis which has a  $90^\circ$  rotation around the  $z$  axis. This gives us a high degree of confidence in our numerical model allowing us to apply it to other shapes.

### 7.2.5 Information Radiation Patterns from Hexagonal Plates

We follow the same method utilised in Section 7.2.3.2 to find the information patterns for our hexagonal plates shown in Fig. 7.8. This method follows the same procedure as in Section 7.2.4, but we also must consider the rotational degrees of freedom. In this case, we have the three motional degrees of freedom  $(x, y, z)$ , and the rotational degrees of freedom  $(\theta_x, \theta_y, \theta_z)$  where the axis in the

Particle Type	Diameter	Thickness
B1	300nm	$2.5\mu\text{m}$
B2	200nm	$3\mu\text{m}$
B3	200nm	$5\mu\text{m}$

Table 7.1: Dimensions for the hexagonal plate particles.

subscript defines the axis that the hexagon is rotated around (see Fig. 2.12 for an image of these degrees of freedom). Recalling Eq. (7.2.25), we find the Fisher information flux through an area  $A_i$  by measuring the change in the electric and magnetic fields passing through the area as we change the property of the particle  $\mu$ . Until now, we have only considered  $\mu$  to be the axis of the particle's motion. However now, we extend that to also include the particle's orientation,  $\mu = (x, y, z, \theta_x, \theta_y, \theta_z)$ . In the same way that we use Eq. (7.2.27) to find the change in the fields as we move the particle from  $\mu = \lambda/100$  to  $\mu = -\lambda/100$ , we can make a small change in the rotation of the particle and replace the denominator with this angular change, in this case we have rotated from  $-1^\circ$  to  $+1^\circ$ .

In Fig. 7.9, we see the IRPs for each degree of freedom  $\mu$  for hexagonal disk particles with dimensions given in Table 7.1 trapped in a standing wave trap. These plots are symmetrical in the  $z$  direction due to the counter propagating beams in the  $z$  axis. We also notice that the IRPs for the motional degrees of freedom show preference to the direction of the particle's motion. This matches the results we would expect to see from the results of the sphere IRPs. For the rotational degrees of freedom, we see that the IRPs favour the direction that light is reflected at each rotation in the  $\theta_x$  and  $\theta_t$  degrees of freedom. The  $\theta_z$  however, scatters information primarily in the  $x$  and  $y$  axes as this is where the change in the particles shape occurs.

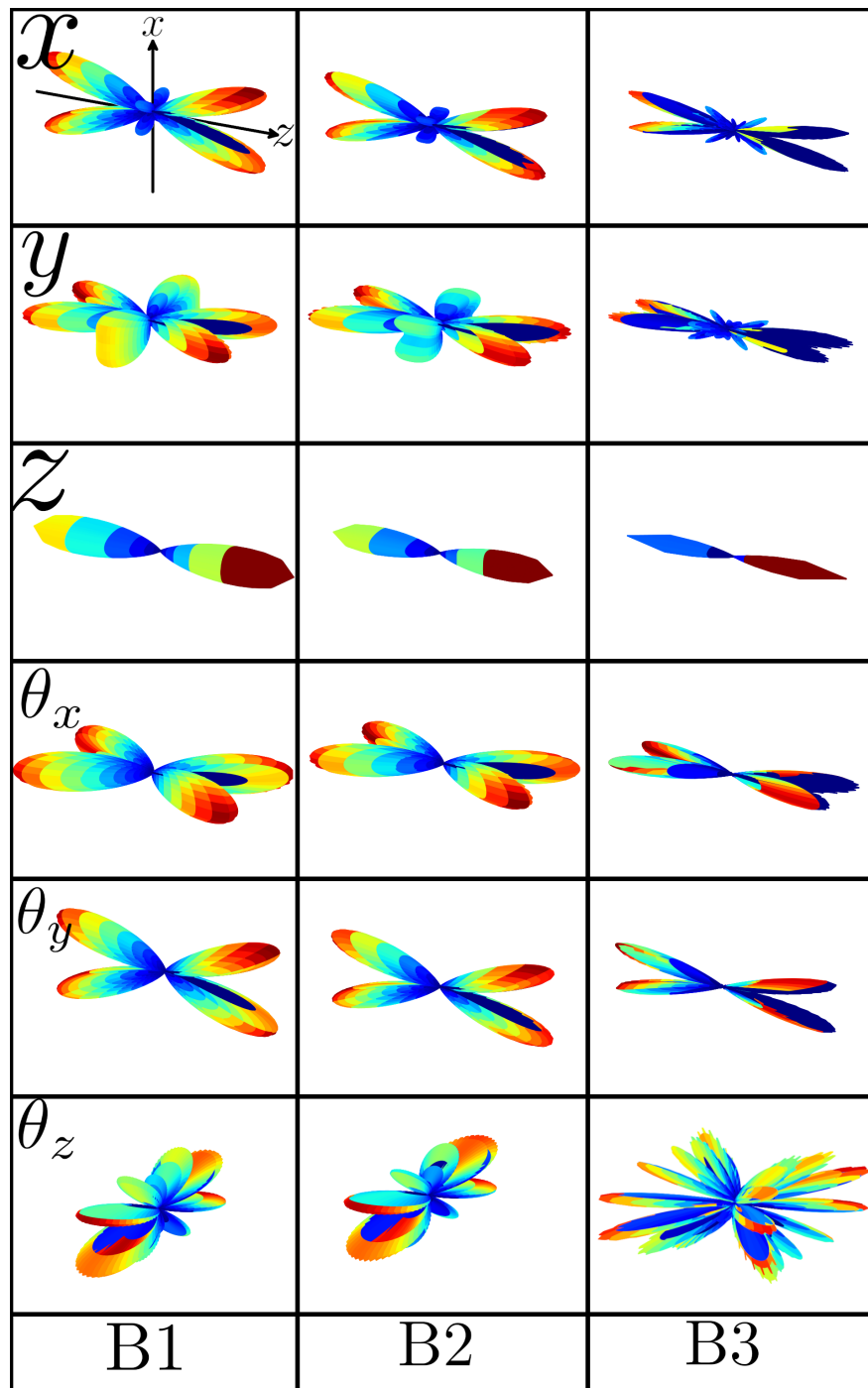


Figure 7.9: IRPs for each degree of freedom  $\mu$  of a hexagonal disk trapped in a standing wave trap made up of two counter propagating beams with a beam waist of  $w_0 = 12\mu\text{m}$ . Each particle has a vertex-to-vertex diameter of  $2.5\mu\text{m}$  to  $5\mu\text{m}$  and a thickness of either 300 or 200nm. These are based on the B1 and B2 batches from [60].

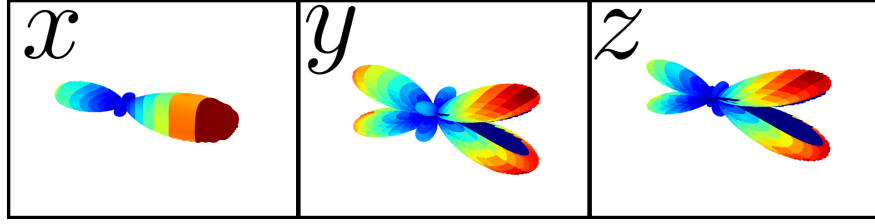


Figure 7.10: Scattering amplitude components calculated from Scuff-EM for a B1 hexagonal disk.

### 7.3 Numerical Solutions for the Talbot Coefficients

We now direct our focus to numerical solutions for the Talbot coefficients. In previous sections of this chapter, we have derived a numerical method for calculating the information contained in scattered light. We have then validated this by applying the method to geometries with known results. Now that we have confidence in this approach, we can use the same techniques to derive the scattering amplitudes needed to find the Talbot coefficients. The scattered field output by Scuff-EM is proportional to the scattering amplitude. By setting the magnitude of the incident field  $E_0 = 1$  we will recover the scattering amplitude in each of the Cartesian components. As a result, we can use the output scattered field to calculate the value of the scattering amplitudes  $f_\mu(k, \mathbf{k}\mathbf{n})$ .

Scuff-EM outputs the Cartesian components of the scattered field, as shown in Fig. 7.10 for a silicon B1 hexagon in a  $12\mu\text{m}$  beam with wavelength  $\lambda = 1550\text{nm}$ . However, the analytical scattering amplitudes use the angle from the scattering direction to define the polarisation of light scattered in each direction as was shown in Fig. 5.9 in section 5.4.2. We can perform a coordinate transform to find the  $\theta$  and  $\phi$  components of the scattering amplitude,

$$f_\phi = (-\sin \phi)f_x + (\cos \phi)f_y \quad (7.3.1a)$$

$$f_\theta = (\cos \theta \cos \phi)f_x + (\cos \theta \sin \phi)f_y + (-\sin \theta)f_z. \quad (7.3.1b)$$

These are then used in place of  $f_\mu(\mathbf{k}, \mathbf{k}')$  which enter the Talbot coefficients



via the scattering terms,

$$a^\mu(s) = \frac{8\pi}{\hbar\omega} \frac{E_G}{a_G} \int \text{Re} [f_\mu^*(k, k\mathbf{n}) f_\mu(-k, k\mathbf{n})] [\cos(kn_z s) - \cos(ks)] d\Omega \quad (7.3.2a)$$

$$b^\mu(s) = \frac{8\pi}{\hbar\omega} \frac{E_G}{a_G} \int \text{Im} [f_\mu^*(k, k\mathbf{n}) f_\mu(-k, k\mathbf{n})] \sin(kn_z s) d\Omega \quad (7.3.2b)$$

$$F^\mu(s) = \frac{8\pi}{\hbar\omega} \frac{E_G}{a_G} \int |f(k, k\mathbf{n})|^2 [\cos((1 - n_z)ks) - 1] d\Omega \quad (7.3.2c)$$

The next steps would be to compute these scattering terms for new shapes of particles and replace them in the Talbot coefficients Eq. (5.4.46). The optimum shape should be chosen such that the values of Eq. (7.3.2) are minimised to reduce the amount of decoherence, whilst also ensuring that the phase shift parameter  $\phi_0$  (Eq. (5.4.33)) can be kept as large as possible as to maximise the interference effect. This optimisation is an interesting problem for future work.

# Chapter 8

## Conclusion

We aimed to explore the extent to which feasible experiments could possibly constrain the parameters of collapse models such as CSL. These models aim to explain the apparent quantum-to-classical transition but have parameters that must be experimentally determined. The approach presented here was to consider a matter-wave interferometer using large masses and spatial separations to probe large scale superpositions. Due to the sparse nature of the data in such an experiment, we apply Bayesian inference to extract as much value from each data point as possible. This produces a real-valued probability distribution over the whole parameter space of the collapse model in contrast to previous works that only considered a binary exclusion to regions of the parameter space. By analysing the full final probability density using Bayesian information gain, we are able to quantify the worth of a given experiment, and thus find optimum experimental parameters.

In order to maximise the information, we find that we must use particles with radii beyond the point-like approximation. Therefore, we employ Talbot coefficients derived using Mie theory from the literature. However, we found that these literature results are incorrect and we present a corrected description. Furthermore we show that spherical particles are not the most optimum shape for constraining CSL parameters. Using recently published concepts about information carried by a scattered field, we present a method for numerically computing the Talbot coefficients for particles with arbitrary geometries. This is verified

against analytical results and applied to thin, hexagonal disk like structures.

We have predicted that in a MAQRO-like experiment, we could be able to push the upper bound of  $\lambda_c$  down to  $10^{-19}\text{Hz}$  at  $r_c = 10^{-7}\text{m}$  using spherical particles with mass of  $7 \times 10^8\text{u}$ . This is an improvement of almost 6 orders of magnitude compared to previous experiments. Further work includes applying the simulations of the interferometer to the hexagonal disks with numerically derived Talbot coefficients and observing how much these geometries can further constrain collapse models.

# Bibliography

- [1] Max Planck. *The Theory of Heat Radiation*. P. BLAKISTON'S SON & CO, Philadelphia, 1st edition, 2012.
- [2] Mark Kasevich and Steven Chu. Atomic interferometry using stimulated Raman transitions. *Physical Review Letters*, 67(2):181–184, 1991.
- [3] William Shockley. *Electrons and Holes in Semiconductors*. D. Van Nostrand Company, 7th edition, 1959.
- [4] D F Walls and Gerard J. Milburn. *Quantum Optics*. Springer-Verlag, Berlin, 2nd edition, 2008.
- [5] Yaakov Y. Fein, Philipp Geyer, Patrick Zwick, Filip Kiałka, Sebastian Pedalino, Marcel Mayor, Stefan Gerlich, and Markus Arndt. Quantum superposition of molecules beyond 25 kDa. *Nature Physics*, 15(12):1242–1245, 2019.
- [6] Neils Bohr. The Quantum Postulate and the Recent Development of Atomic Theory. *Nature*, 121:580–590, 1928.
- [7] Hugh Everett. "Relative state" formulation of quantum mechanics. *Reviews of Modern Physics*, 29(3):454–462, 1957.
- [8] Angelo Bassi, Kinjalk Lochan, Seema Satin, Tejinder P Singh, and Hendrik Ulbricht. Models of wave-function collapse, underlying theories, and experimental tests. *Reviews of Modern Physics*, 85(2):471–527, 2013.

- [9] Matteo Carlesso, Sandro Donadi, Luca Ferialdi, Mauro Paternostro, Hendrik Ulbricht, and Angelo Bassi. Present status and future challenges of non-interferometric tests of collapse models, 2022.
- [10] Björn Brezger, Lucia Hackermüller, Stefan Uttenthaler, Julia Petschinka, Markus Arndt, and Anton Zeilinger. Matter-Wave Interferometer for Large Molecules. *Physical Review Letters*, 88(10):4, 2002.
- [11] James Bateman, Stefan Nimmrichter, Klaus Hornberger, and Hendrik Ulbricht. Near-field interferometry of a free-falling nanoparticle from a point-like source. *Nature Communications*, 5:1–5, 2014.
- [12] D S Sivia and J Skilling. *Data Analysis A Bayesian Tutorial*. Oxford University Press, 1st edition, 2006.
- [13] C.E. Shannon. A mathematical theory of communication. *The Bell system technical journal*, 27(3):519–520, 1948.
- [14] E. F. Nichols and G. F. Hull. The Pressure Due to Radiation. *Proceedings of the American Academy of Arts and Sciences*, 38(20):559, 1903.
- [15] E. F. Nichols and G. F. Hull. A preliminary communication on the pressure of heat and light radiation. *Physical Review (Series I)*, 13(5):307–320, 1901.
- [16] A. Ashkin. Acceleration and Trapping of Particles by Radiation Pressure. *Physical Review Letters*, 24(4):156–159, 1970.
- [17] Arthur Ashkin, Karin Schutze, J. M. Dziedzic, Ursula Euteneuer, and Manfred Schliwa. Force generation of organelle transport measured in vivo by an infrared laser trap. *Nature*, 348(November):346–348, 1990.
- [18] Lucien P Ghislain and Watt W Webb. Scanning-force microscope based on an optical trap. *Optics Letters*, 18(19):1678, oct 1993.
- [19] Uroš Delić, Manuel Reisenbauer, Kahan Dare, David Grass, Vladan Vuletić, Nikolai Kiesel, and Markus Aspelmeyer. Cooling of a levitated nanoparticle to the motional quantum ground state. *Science*, 367(6480):892–895, 2020.

- [20] Johannes Piotrowski, Dominik Windey, Jayadev Vijayan, Carlos Gonzalez-Ballester, Andrés de los Ríos Sommer, Nadine Meyer, Romain Quidant, Oriol Romero-Isart, René Reimann, and Lukas Novotny. Simultaneous ground-state cooling of two mechanical modes of a levitated nanoparticle. *Nature Physics*, 19(7):1009–1013, 2023.
- [21] Sougato Bose, Anupam Mazumdar, Gavin W. Morley, Hendrik Ulbricht, Marko Toroš, Mauro Paternostro, Andrew A. Geraci, Peter F. Barker, M. S. Kim, and Gerard Milburn. Spin Entanglement Witness for Quantum Gravity. *Physical Review Letters*, 119(24):1–6, 2017.
- [22] B. P. Abbott et al. Observation of Gravitational Waves from a Binary Black Hole Merger. *Physical Review Letters*, 116(6):061102, feb 2016.
- [23] George Winstone, Mishkat Bhattacharya, Andrew A. Geraci, Tongcang Li, Peter J. Pauzauskie, and Nick Vamivakas. Levitated optomechanics: A tutorial and perspective. 2023.
- [24] A. Ashkin, J. M. Dziedzic, J. E. Bjorkholm, and Steven Chu. Observation of a single-beam gradient force optical trap for dielectric particles. *Optics Letters*, 11(5):196–198, 1986.
- [25] Y Harada and Toshimitsu Asakura. ScienceDirect - Optics Communications : Radiation forces on a dielectric sphere in the Rayleigh scattering regime. *Optics communications*, 124(March):529–541, 1996.
- [26] Craig F Borhen and Donald R Huffman. *Absorption and Scattering of Light by Small Particles*. John Wiley & Sons, Inc., 1st edition, 1983.
- [27] Shoji Asano. Light scattering properties of spheroidal particles. *Applied Optics*, 18(5):712, 1979.
- [28] K. F. Ren, G. Gréhan, and G. Gouesbet. Scattering of a Gaussian beam by an infinite cylinder in the framework of generalized Lorenz–Mie theory: formulation and numerical results. *Journal of the Optical Society of America A*, 14(11):3014, 1997.

- [29] Lukas Novotny and Bert Hecht. *Principles of Nano-Optics*. Cambridge University Press, New York, 1st edition, 2006.
- [30] Arthur Ashkin. *Optical Trapping and Manipulation of Neutral Particles Using Lasers*. World Scientific, 2006.
- [31] Jan Gieseler, Juan Ruben Gomez-Solano, Alessandro Magazzù, Isaac Pérez Castillo, Laura Pérez García, Marta Gironella-Torrent, Xavier Viader-Godoy, Felix Ritort, Giuseppe Pesce, Alejandro V. Arzola, Karen Volke-Sepúlveda, and Giovanni Volpe. Optical tweezers — from calibration to applications: a tutorial. *Advances in Optics and Photonics*, 13(1):74, 2021.
- [32] A. Ashkin. Forces of a single-beam gradient laser trap on a dielectric sphere in the ray optics regime. *Biophysical Journal*, 61(2):569–582, 1992.
- [33] Andrew Zangwill. *Modern Electrodynamics*. Cambridge University Press, New York, 1st edition, 2012.
- [34] Kirstine Berg-Sørensen and Henrik Flyvbjerg. Power spectrum analysis for optical tweezers. *Review of Scientific Instruments*, 75(3):594–612, 2004.
- [35] M. Burns, J. M. Fournier, and J. A. Golovchenko. Optical matter: Binding and crystallization in intense optical fields. *XVII International Conference on Quantum Electronics. Digest of*, (August):64, 1990.
- [36] L. Z. Cai, X. L. Yang, and Y. R. Wang. All fourteen Bravais lattices can be formed by interference of four noncoplanar beams. *Optics Letters*, 27(11):900, 2002.
- [37] Myungjoon Kim, Nayoung Kim, and Jonghwa Shin. Realization of all two-dimensional Bravais lattices with metasurface-based interference lithography. *Nanophotonics*, pages 1–8, jan 2024.
- [38] Tongcang Li, Simon Kheifets, and Mark G. Raizen. Millikelvin cooling of an optically trapped microsphere in vacuum. *Nature Physics*, 7(7):527–530, 2011.

- [39] Jan Gieseler, Bradley Deutsch, Romain Quidant, and Lukas Novotny. Subkelvin parametric feedback cooling of a laser-trapped nanoparticle. *Physical Review Letters*, 109(10):3–8, 2012.
- [40] M. Poggio, C. L. Degen, H. J. Mamin, and D. Rugar. Feedback cooling of a cantilever’s fundamental mode below 5 mK. *Physical Review Letters*, 99(1):2–5, 2007.
- [41] Felix Tebbenjohanns, Martin Frimmer, and Lukas Novotny. Optimal Position Detection of a Dipolar Scatterer in a Focused Field. *Physical Review A*, 100(4), 2019.
- [42] Daniel Goldwater, Benjamin A. Stickler, Lukas Martinetz, Tracy E. Northup, Klaus Hornberger, and James Millen. Levitated electromechanics: All-electrical cooling of charged nano- and micro-particles. *Quantum Science and Technology*, 4(2), 2019.
- [43] M. Iwasaki, T. Yotsuya, T. Naruki, Y. Matsuda, M. Yoneda, and K. Aikawa. Electric feedback cooling of single charged nanoparticles in an optical trap. *Physical Review A*, 99(5):51401, 2019.
- [44] Stephen J. Blundell and Katherine M. Blundell. *Concepts in Thermal Physics*. Oxford University Press, Oxford, 1st edition, 2006.
- [45] A. Velyhan, P. Žilavý, J. Pavlů, J. Šafínková, and Z. Němeček. Ion beam effects on dust grains. *Vacuum*, 76(4):447–455, 2004.
- [46] Sergey I. Kopnin, Tatiana I. Morozova, and Sergey I. Popel. Electron Beam Action and High Charging of Dust Particles. *IEEE Transactions on Plasma Science*, 46(4):701–703, 2018.
- [47] M. Pauthenier and M. Moreau-Hanot. La charge des particules sphériques dans un champ ionisé. *Journal de Physique et le Radium*, 3(12):590–613, 1932.
- [48] Kazimierz Adamiak. Rate of charging of spherical particles by monopolar ions in electric fields. *IEEE Transactions on Industry Applications*, 38(4):1001–1008, 2002.



- [49] Martin Frimmer, Karol Luszcz, Sandra Ferreira, Vijay Jain, Erik Hebestreit, and Lukas Novotny. Controlling the net charge on a nanoparticle optically levitated in vacuum. *Physical Review A*, 95(6), 2017.
- [50] Bradley R. Slezak, Charles W. Lewandowski, Jen Feng Hsu, and Brian D’Urso. Cooling the motion of a silica microsphere in a magneto-gravitational trap in ultra-high vacuum. *New Journal of Physics*, 20(6), 2018.
- [51] Peter Asenbaum, Stefan Kuhn, Stefan Nimmrichter, Ugur Sezer, and Markus Arndt. Cavity cooling of free silicon nanoparticles in high vacuum. *Nature Communications*, 4, 2013.
- [52] Mitsuyoshi Kamba, Ryoga Shimizu, and Kiyotaka Aikawa. Optical cold damping of neutral nanoparticles near the ground state in an optical lattice. *Optics Express*, 30(15):26716, 2022.
- [53] N. Kerker, R. Röpke, L. M. Steinert, A. Pooch, and A. Stibor. Quantum decoherence by Coulomb interaction. *New Journal of Physics*, 22(6), 2020.
- [54] Felix Tebbenjohanns, M. Luisa Mattana, Massimiliano Rossi, Martin Frimmer, and Lukas Novotny. Quantum control of a nanoparticle optically levitated in cryogenic free space. *Nature*, 595(7867):378–382, 2021.
- [55] Benjamin A. Stickler, Birthe Papendell, Stefan Kuhn, Björn Schrämski, James Millen, Markus Arndt, and Klaus Hornberger. Probing macroscopic quantum superpositions with nanorotors. *New Journal of Physics*, 20(12), 2018.
- [56] Zhujing Xu and Tongcang Li. Detecting Casimir torque with an optically levitated nanorod. *Physical Review A*, 96(3):1–12, 2017.
- [57] Keith D. Bonin, Bakhit Kourmanov, and Thad G. Walker. Light torque nanocontrol, nanomotors and nanorockers. *Optics Express*, 10(19):984, 2002.

- [58] Stefan Kuhn, Alon Kosloff, Benjamin A. Stickler, Fernando Patolsky, Klaus Hornberger, Markus Arndt, and James Millen. Full rotational control of levitated silicon nanorods. *Optica*, 4(3):356, 2017.
- [59] Stefan Kuhn, Peter Asenbaum, Alon Kosloff, Michele Sclafani, Benjamin A. Stickler, Stefan Nimmrichter, Klaus Hornberger, Ori Cheshnovsky, Fernando Patolsky, and Markus Arndt. Cavity-Assisted Manipulation of Freely Rotating Silicon Nanorods in High Vacuum. *Nano Letters*, 15(8):5604–5608, 2015.
- [60] George Winstone, Zhiyuan Wang, Shelby Klomp, Greg R Felsted, Andrew Laeuger, Chaman Gupta, Daniel Grass, Nancy Aggarwal, Jacob Sprague, Peter J Pauzauskie, Shane L Larson, Vicky Kalogera, and Andrew A Geraci. Optical Trapping of High-Aspect-Ratio NaYF Hexagonal Prisms for kHz-MHz Gravitational Wave Detectors. *Physical Review Letters*, 129(5), 2022.
- [61] Mark Fox. The Harmonic Oscillator. In *Quantum Optics*, chapter 3.3, pages 41–43. Oxford University Press, New York, 1st edition, 2006.
- [62] J.J. Sakurai and Jim Napolitano. *Modern Quantum*. 2011.
- [63] Michael Moore. Lecture 34 : The Density Operator, 2009.
- [64] Franz Schwabl. *Statistical Mechanics*. Berlin, 2000.
- [65] E. Wigner. On the quantum correction for thermodynamic equilibrium. *Physical Review*, 40(5):749–759, 1932.
- [66] Wolfgang P. Schleich. *Quantum Optics in Phase Space*. Wiley-VCH, Berlin, 1st edition, 2001.
- [67] William B. Case. Wigner functions and Weyl transforms for pedestrians. *American Journal of Physics*, 76(10):937–946, 2008.
- [68] Hermann Weyl. *The Theory of Groups and Quantum Mechanics*. Dover, New York, 1931.
- [69] Maximilian Schlosshauer. Quantum Decoherence. pages 1–73, nov 2019.

- [70] K. Hornberger. Introduction to decoherence theory. In *Lecture Notes in Physics*, volume 768, pages 221–276. 2009.
- [71] Louis N Hand and Janet D Finch. *Analytical mechanics*. Cambridge University Press, New York, 1 edition, 1998.
- [72] John Von Neumann. *Mathematical Foundations of Quantum Mechanics*. Princeton University Press, translatio edition, 1996.
- [73] Angelo Bassi and Giancarlo Ghirardi. A general argument against the universal validity of the superposition principle, 2000.
- [74] Stephen L. Adler. Why decoherence has not solved the measurement problem: A response to P.W. Anderson. *Studies in History and Philosophy of Science Part B - Studies in History and Philosophy of Modern Physics*, 34(1):135–142, 2003.
- [75] Angelo Bassi and Kasra Hejazi. No-faster-than-light-signaling implies linear evolution. A re-derivation. *European Journal of Physics*, 36(5):1–17, 2015.
- [76] Roderich Tumulka. A relativistic version of the Ghirardi-Rimini-Weber model. *Journal of Statistical Physics*, 125(4):825–844, 2006.
- [77] G. C. Ghirardi, R. Grassi, and P. Pearle. Relativistic dynamical reduction models: General framework and examples. *Foundations of Physics*, 20(11):1271–1316, nov 1990.
- [78] Iwo Bialynicki-Birula and Jerzy Mycielski. Nonlinear wave mechanics. *Annals of Physics*, 100(1-2):62–93, 1976.
- [79] Steven Weinberg. Precision tests of quantum mechanics. *Physical Review Letters*, 62(5):61–68, 1989.
- [80] N. Gisin. Weinberg’s non-linear quantum mechanics and supraluminal communications. *Physics Letters A*, 143(1-2):1–2, 1990.
- [81] Philip Pearle. Reduction of the state vector by a nonlinear Schrödinger equation. *Physical Review D*, 13(4):857–868, 1976.

- [82] Angelo Bassi. Collapse models: Analysis of the free particle dynamics. *Journal of Physics A: Mathematical and General*, 38(14):3173–3192, 2005.
- [83] G. C. Ghirardi, A. Rimini, and T. Weber. Unified microscopic macroscopic. *Physical Review D*, 34(2):470–491, 1986.
- [84] L. Diósi. A universal master equation for the gravitational violation of quantum mechanics. *Physics Letters A*, 120(8):377–381, 1987.
- [85] Roger Penrose. On gravity’s role in quantum state reduction. *General Relativity and Gravitation*, 28(5):581–600, 1996.
- [86] Roger Penrose. Quantum computation, entanglement and state reduction. *Philosophical Transactions of the Royal Society of London. Series A: Mathematical, Physical and Engineering Sciences*, 356(1743):1927–1939, aug 1998.
- [87] Gian Carlo Ghirardi, Philip Pearle, and Alberto Rimini. Markov processes in Hilbert space and continuous spontaneous localization of systems of identical particles. *Physical Review A*, 42(1):78–89, 1990.
- [88] Philip Pearle and Euan Squires. Bound State Excitation, Nucleon Decay Experiments, and Models of Wave Function Collapse. *Physical Review Letters*, 73(1), 1994.
- [89] Thomas Young. I. The Bakerian Lecture. Experiments and calculations relative to physical optics. *Philosophical Transactions of the Royal Society of London*, 94:1–16, 1804.
- [90] C. J. Davisson. The Diffraction of Electrons by a Crystal of Nickel. *Bell System Technical Journal*, 7(1):90–105, 1928.
- [91] Shaun Laing and James Bateman. Bayesian inference for near-field interferometric tests of collapse models. *arXiv*, arXiv:2310.05763, 2023.
- [92] Stephen L. Adler and Andrea Vinante. Bulk heating effects as tests for collapse models. *Physical Review A*, 97(5):1–6, 2018.

- [93] Marco Bilardello, Sandro Donadi, Andrea Vinante, and Angelo Bassi. Bounds on collapse models from cold-atom experiments. *Physica A: Statistical Mechanics and its Applications*, 462:764–782, nov 2016.
- [94] Tim Kovachy, Jason M. Hogan, Alex Sugarbaker, Susannah M. Dickerson, Christine A. Donnelly, Chris Overstreet, and Mark A. Kasevich. Matter wave lensing to picokelvin temperatures. *Physical Review Letters*, 114(14):1–6, 2015.
- [95] Sandro Donadi, Kristian Piscicchia, Raffaele Del Grande, Catalina Curceanu, Matthias Laubenstein, and Angelo Bassi. Novel CSL bounds from the noise-induced radiation emission from atoms. *The European Physical Journal C*, 81(8):773, aug 2021.
- [96] Stephen L Adler, Angelo Bassi, Matteo Carlesso, and Andrea Vinante. Testing continuous spontaneous localization with Fermi liquids. *Physical Review D*, 99(10):103001, may 2019.
- [97] H.F. Talbot. LXXVI. Facts relating to optical science. No. IV . *The London, Edinburgh, and Dublin Philosophical Magazine and Journal of Science*, 9(56):401–407, 1836.
- [98] William B. Case, Mathias Tomandl, Sarayut Deachapunya, and Markus Arndt. Realization of optical carpets in the Talbot and Talbot-Lau configurations. *Optics Express*, 17(23):20966, 2009.
- [99] Christian Brand, Stephan Troyer, Christian Knobloch, Ori Cheshnovsky, and Markus Arndt. Single-, double-, and triple-slit diffraction of molecular matter waves. *American Journal of Physics*, 89(12):1132–1138, 2021.
- [100] Bjorn Brezger, Markus Arndt, and Anton Zeilinger. Concepts for near-field interferometers. *Journal of Optics B: Quantum Semiclassical Optics*, 5(S82), 2003.
- [101] Stefan Nimmrichter and Klaus Hornberger. Theory of near-field matter wave interference beyond the eikonal approximation. *Physics Review A*, 78, 2008.

- [102] H. B. G. Casimir and D. Polder. The Influence of Retardation on the London-van der Waals Forces. *Physical Review*, 73(4):360–372, feb 1948.
- [103] Stefan Gerlich, Lucia Hackermüller, Klaus Hornberger, Alexander Stibor, Hendrik Ulbricht, Michael Gring, Fabienne Goldfarb, Tim Savas, Marcel Müri, Marcel Mayor, and Markus Arndt. A Kapitza-Dirac-Talbot-Lau interferometer for highly polarizable molecules. *Nature Physics*, 3(10):711–715, 2007.
- [104] Klaus Hornberger, Stefan Gerlich, Hendrik Ulbricht, Lucia Hackermüller, Stefan Nimmrichter, Ilya V. Goldt, Olga Boltalina, and Markus Arndt. Theory and experimental verification of Kapitza-Dirac-Talbot-Lau interferometry. *New Journal of Physics*, 11, 2009.
- [105] Alessio Belenchia, Giulio Gasbarri, Rainer Kaltenbaek, Hendrik Ulbricht, and Mauro Paternostro. Talbot-Lau effect beyond the point-particle approximation. *Physical Review A*, 100(3), 2019.
- [106] Rainer Kaltenbaek, Markus Aspelmeyer, Peter F Barker, Angelo Bassi, James Bateman, Kai Bongs, Sougato Bose, Claus Braxmaier, Āaslav Brukner, Bruno Christophe, Michael Chwalla, Pierre Franois Cohadon, Adrian Michael Cruise, Catalina Curceanu, Kishan Dholakia, Lajos Diosi, Klaus Doringshoff, Wolfgang Ertmer, Jan Gieseler, Norman Gurlebeck, Gerald Hechenblaikner, Antoine Heidmann, Sven Herrmann, Sabine Hossenfelder, Ulrich Johann, Nikolai Kiesel, Myungshik Kim, Claus Lammerzahl, Astrid Lambrecht, Michael Mazilu, Gerard J Milburn, Holger Muller, Lukas Novotny, Mauro Paternostro, Achim Peters, Igor Pikovski, Andre Pilan Zanoni, Ernst M Rasel, Serge Reynaud, Charles Jess Riedel, Manuel Rodrigues, Loic Rondin, Albert Roura, Wolfgang P Schleich, Jorg Schmiedmayer, Thilo Schuldt, Keith C Schwab, Martin Tajmar, Guglielmo M Tino, Hendrik Ulbricht, Rupert Ursin, and Vlatko Vedral. Macroscopic quantum resonators (MAQRO): 2015 update, 2016.

- [107] M. D. Summers, D. R. Burnham, and D. McGloin. Trapping solid aerosols with optical tweezers: A comparison between gas and liquid phase optical traps. *Optics Express*, 16(11):7739, 2008.
- [108] Maryam Nikkhou, Yanhui Hu, James A. Sabin, and James Millen. Direct and clean loading of nanoparticles into optical traps at millibar pressures. *Photonics*, 8(11), 2021.
- [109] Evan Weisman, Chethn Krishna Galla, Cris Montoya, Eduardo Alejandro, Jason Lim, Melanie Beck, George P. Winstone, Alexey Grinin, William Eom, and Andrew A. Geraci. An apparatus for in-vacuum loading of nanoparticles into an optical trap. *Review of Scientific Instruments*, 93(11):1–9, 2022.
- [110] Gambhir Ranjit, David P. Atherton, Jordan H. Stutz, Mark Cunningham, and Andrew A. Geraci. Attonewton force detection using microspheres in a dual-beam optical trap in high vacuum. *Physical Review A - Atomic, Molecular, and Optical Physics*, 91(5):1–5, 2015.
- [111] Gambhir Ranjit, Mark Cunningham, Kirsten Casey, and Andrew A. Geraci. Zeptonewton force sensing with nanospheres in an optical lattice. *Physical Review A*, 93(5):1–5, 2016.
- [112] Cris Montoya, Eduardo Alejandro, William Eom, Daniel Grass, Nicolas Clarisse, Apryl Witherspoon, and Andrew A. Geraci. Scanning force sensing at micrometer distances from a conductive surface with nanospheres in an optical lattice. *Applied Optics*, 61(12):3486, 2022.
- [113] David P. Atherton. *Sensitive force measurements with optically trapped micro-spheres in high vacuum*. Ph.d., University of Nevada, 2015.
- [114] ESA. Assessment of a Quantum Physics Payload Platform QPPF. Technical Report CDF-183(C), 2018.
- [115] Lorenzo Dania, Katharina Heidegger, Dmitry S. Bykov, Giovanni Cerchiari, Gabriel Araneda, and Tracy E. Northup. Position Measurement of a Levi-

- tated Nanoparticle via Interference with Its Mirror Image. *Physical Review Letters*, 129(1):13601, 2022.
- [116] Nikolai Kiesel, Florian Blaser, Uroš Delić, David Grass, Rainer Kaltenbaek, and Markus Aspelmeyer. Cavity cooling of an optically levitated submicron particle. *Proceedings of the National Academy of Sciences of the United States of America*, 110(35):14180–14185, 2013.
- [117] Eric W Weisstein. Convolution Theorem, 2024.
- [118] Uwe Kreibig and Michael Vollmer. *Optical Properties of Metal Clusters*. Springer, 1995.
- [119] Stefan Nimmrichter, Klemens Hammerer, Peter Asenbaum, Helmut Ritsch, and Markus Arndt. Master equation for the motion of a polarizable particle in a multimode cavity. *New Journal of Physics*, 12, 2010.
- [120] Milton Abramowitz and Stegun Irene. *Handbook of Mathematical Functions*. National Bureau of Standards, 10th edition, 1972.
- [121] R. G. Barrera, G. A. Estevez, and J. Giraldo. Vector spherical harmonics and their application to magnetostatics. *European Journal of Physics*, 6(4):287–294, 1985.
- [122] Casper H. L. Beentjes. Quadrature on a Spherical Surface. *International Conference on Mathematics and Computational Methods Applied to Nuclear Science and Engineering*, pages 1–15, 2015.
- [123] F. London. Zur Theorie und Systematik der Molekularkrafte. *Zeitschrift fur Physik*, 63(3-4):245–279, mar 1930.
- [124] W.M. Haynes. *CRC Handbook of Chemistry and Physics*. 95th edition, 2014.
- [125] Stefan Nimmrichter, Philipp Haslinger, Klaus Hornberger, and Markus Arndt. Concept of an ionizing time-domain matter-wave interferometer. *New Journal of Physics*, 13, 2011.



- [126] Giulio Gasbarri, Alessio Belenchia, Mauro Paternostro, and Hendrik Ulbricht. Prospects for near-field interferometric tests of collapse models. *Physical Review A*, 103(2):1–10, 2021.
- [127] David Lunn, Christopher Jackson, Nicky Best, Andrew Thomas, and David Spiegelhalter. *Prior Distributions*. CRC Press/Chapman and Hall, 1st edition, 2012.
- [128] Ruoyong Yang and James O Berger. *A Catalog of Noninformative Priors*, 1998.
- [129] Harold Jeffreys. An Invariant Form for the Prior Probability in Estimation Problems. *Proceedings of the Royal Society of London. Series A, Mathematical and Physical Sciences*, 186(1007):453–461, 1946.
- [130] Alexander Ly, Maarten Marsman, Josine Verhagen, Raoul P.P.P. Grasman, and Eric Jan Wagenmakers. A Tutorial on Fisher information. *Journal of Mathematical Psychology*, 80:40–55, 2017.
- [131] Jose M. Bernardo. Reference Posterior Distributions for Bayesian Inference. *Journal of the Royal Statistical Society: Series B (Methodological)*, 41(2):113–128, 1979.
- [132] Ben Lambert. *A Student’s Guide to Bayesian Statistics*. SAGE Publications Ltd, 1 edition, 2018.
- [133] Arnold Zellner. Models, Prior Information, and Bayesian Analysis. *Journal of Econometrics*, 75, 1996.
- [134] Stephen L. Adler. Lower and upper bounds on CSL parameters from latent image formation and IGM heating. *Journal of Physics A: Mathematical and Theoretical*, 40(12):2935–2957, 2007.
- [135] Stefan Nimmrichter and Klaus Hornberger. Macroscopicity of mechanical quantum superposition states. *Physical Review Letters*, 110(16):1–11, 2013.

- [136] Björn Schriniski, Stefan Nimmrichter, Benjamin A. Stickler, and Klaus Hornberger. Macroscopicity of quantum mechanical superposition tests via hypothesis falsification. *Physical Review A*, 100(3):1–20, 2019.
- [137] Xun Huan and Youssef M Marzouk. Simulation-based optimal Bayesian experimental design for nonlinear systems. *Journal of Computational Physics*, 232(1):288–317, 2013.
- [138] Kenneth J. Ryan. Estimating Expected Information Gains for Experimental Designs with Application to the Random Fatigue-Limit Model. *Journal of Computational and Graphical Statistics*, 12(3):585–603, 2003.
- [139] Nancy Aggarwal, George P. Winstone, Mae Teo, Masha Baryakhtar, Shane L. Larson, Vicky Kalogera, and Andrew A. Geraci. Searching for New Physics with a Levitated-Sensor-Based Gravitational-Wave Detector. *Physical Review Letters*, 128(11):111101, 2022.
- [140] M. T.Homer Reid. Scuff-EM, 2018.
- [141] M. T.Homer Reid and Steven G. Johnson. Efficient Computation of Power, Force, and Torque in BEM Scattering Calculations. *IEEE Transactions on Antennas and Propagation*, 63(8):3588–3598, 2015.
- [142] Cristophe Guezaine and Jean-François Remacle. Gmsh, 2022.
- [143] Charles Dapogny, Cécile Dobrzynski, Pascal Frey, and Algiane Froehly. Mmg Platform, 2023.
- [144] D. R. Wilton, S. S.M. Rao, and A. W. Glisson. Electromagnetic Scattering By Surfaces of Arbitrary Shape. *National Bureau of Standards, Special Publication*, (3), 1980.
- [145] Homer Reid. Surface Integral Equations and Boundary Element Method, 2012.
- [146] Patrick Maurer, Carlos Gonzalez-Ballester, and Oriol Romero-Isart. Quantum theory of light interaction with a Lorenz-Mie particle: Optical de-

- tection and three-dimensional ground-state cooling. *Physical Review A*, 108(3):033714, sep 2023.
- [147] Orazio Svelto. Gaussian Beams. In *Principles of Lasers*, chapter 4.7, pages 148–155. Springer US, New York, 4 edition, 1998.
- [148] A. Rubinowicz. On the anomalous propagation of phase in the focus. *Physical Review*, 54(11):931–936, 1938.
- [149] C. J.R. Sheppard and S. Saghafi. Gaussian beams beyond the paraxial approximation. *Guangdianzi Jiguang/Journal of Optoelectronics Laser*, 9(6):42–44, 1998.
- [150] Chris Dawson and James Bateman. Spectral analysis and parameter estimation in levitated optomechanics. *Journal of the Optical Society of America B*, 36(6):1565, 2019.
- [151] Christophe Geuzaine and Jean François Remacle. Gmsh: A 3-D finite element mesh generator with built-in pre- and post-processing facilities. *International Journal for Numerical Methods in Engineering*, 79(11):1309–1331, 2009.
- [152] Jakob Hüpfel, Felix Russo, Lukas M. Rachbauer, Dorian Bouchet, Junjie Lu, Ulrich Kuhl, and Stefan Rotter. Continuity Equation for the Flow of Fisher Information in Wave Scattering. *2023 Conference on Lasers and Electro-Optics, CLEO 2023*, aug 2023.